ABSTRACT

Title of dissertation: Fully Anisotropic Solution of the Three Dimensional Boltzmann Transport Equation

Francis G. VanGessel, Masters of Science, 2016

Thesis directed by: Professor Peter W. Chung
Department of Mechanical Engineering

The development of accurate modeling techniques for nanoscale thermal transport is an active area of research. Modern day nanoscale devices have length scales of tens of nanometers and are prone to overheating, which reduces device performance and lifetime. Therefore, accurate temperature profiles are needed to predict the reliability of nanoscale devices. The majority of models that appear in the literature obtain temperature profiles through the solution of the Boltzmann transport equation (BTE). These models often make simplifying assumptions about the nature of the quantized energy carriers (phonons). Additionally, most previous work has focused on simulation of planar two dimensional structures. This thesis presents a method which captures the full anisotropy of the Brillouin zone within a three dimensional solution to the BTE. The anisotropy of the Brillouin zone is captured by solving the BTE for all vibrational modes allowed by the Born Von-Karman boundary conditions.

Table of Contents

List of Tables

List of Figures

Chapter 1: Introduction

1.1 Perspective and Motivation

Moore's Law states that the number of transistors on an integrated circuit doubles roughly every two years. This qualitative law has been the driving force behind the rapid increase in processor speeds over the past few decades. One result of the increase in transistor density is an increase in the power generated on an integrated circuit. Although in general the power generated per transistor shrinks as the transistor characteristic dimensions are reduced, this effect is counterbalanced by the increase of the overall number of transistors on an integrated circuit, leading to an overall power generation increase. Furthermore, in order to double the number of transistors on an integrated circuit, the size of a transistor must be reduced. The most recent generation of transistors have gate lengths of 14 nanometers [4] with the next generation reaching even smaller lengths. This size reduction results in hotspot creation within the transistor where heat is trapped and cannot be efficiently removed [5–9]. These self heating effects are exacerbated in devices with non-planar three dimensional geometries. The combined effects of increasing power density coupled with shrinking feature size leads to inefficient heat removal, resulting in large increases in temperature which negatively effects device performance. Among

these negative effects are reductions in saturation currents and maximum allowable frequencies which reduce the transistors operating performance [10]. Furthermore, the strain caused by overheating reduces the transistor lifetime [11]. Therefore, accurate thermal modeling is critical for determining device reliability in existing devices as well as designing transistors which minimize hotspot temperatures.

Continuum laws, such as Fourier's Law of heat conduction, rely on the assumption that a material may be assumed homogeneous on the length scale of interest. In addition, these laws assume that local equilibrium is assumed to prevail throughout the material. When devices, such as transistors, have characteristic dimensions within the nanometer regime, sub-continuum effects begin to dominate and the assumptions underlying continuum laws are no longer valid. Therefore modeling techniques that are capable of capturing subcontinuum effects are required for accurate prediction of temperature profiles within such nanoscale devices. One such modeling technique is the solution of the Boltzmann transport equation which may be numerically solved to determine a wide range of thermodynamic properties, including temperature profiles, in devices with dimensions ranging from a few nanometers up through the macroscale. The Boltzmann transport equation is an appealing technique as it is capable of capturing ballistic transport effects that emerge on the atomistic scale, while also accurately modeling regions where diffusive transport dominates. Thus the Boltzmann transport equation is a widely used method for simulation of nanoscale devices and thin crystalline films.

Despite gaining widespread use for nanoscale thermal modeling, methods for the numerical solution of the Boltzmann transport equation detailed in the liter-

ature often have a variety of simplifying assumptions that limit the accuracy of the solutions obtained. Chief amongst these are the gray and semi-gray approximation which assume that the energy carriers, henceforth referred to as phonons, within a crystalline material may be approximated by a few averaged phonon properties [12–18]. More recently, work done in the area of nanoscale thermal modeling has replaced the gray approximation with a Boltzmann transport equation formulation that accounts for variation in the phonon properties, however this variation is considered along only a single high symmetry direction in the Brillouin Zone (region of reciprocal space containing all unique vibrational modes that exist within a material) [19–25]. Therefore, energy transport is assumed to be isotropic, an assumption that has been shown to be inaccurate in the literature [26]. Other assumptions made in the literature assume that temperature varies in only one or two dimensions, leading to Boltzmann transport solution methods that are unable to model new device geometries that are intrinsically three dimensional. Examples of such devices are new transistor designs such as the Fin field effect transistor (FinFET) first developed at Berkeley [27] and gaining adoption in present day commercial integrated circuits [4]. Additionally, few published methods for solving the Boltzmann transport equation rigorously account for the effect of material geometry on the allowed vibrational modes. Those that do, do not consider temperature variation in three dimensions [26, 28]. While the simplifications and assumptions listed here do not apply to all of the Boltzmann transport solution methods appearing in the literature, no method has appeared in the literature which has completely eliminated all of the simplifications documented above.

In this thesis an algorithm for solving the Boltzmann transport equation is presented. This approach is then implemented into a numerical Boltzmann transport equation code capable of three dimensional device simulation. The algorithm presented in this thesis avoids simplifying assumptions, which appear in approaches detailed in the literature, in order to fully capture the wide array of phonon physics. Full Brillouin zone anisotropy is accounted for by determining phonon properties throughout the Brillouin zone, not just along one high symmetry directions. To this end, phonon properties are determined via a molecular dynamics approach for obtaining lattice vibrational properties which are then used as inputs to the Boltzmann transport code. Secondly, the Boltzmann transport equation is discretized in a manner allowing for three dimensional temperature gradients. This is important as recent nanoscale devices are no longer planar, i.e. approximately two dimensional, and therefore require three dimensional modeling. Finally the algorithm solves the Boltzmann transport equation for all available vibrational modes within a material by considering the device geometry. Therefore, the approach detailed in this work is capable of capturing effects such as the reduction in thermal conductivity which is known to occur in devices with very thin dimensions [26].

By eliminating the various simplifications and assumptions that appear in much of the modeling methods utilizing the Boltzmann transport equation, a Boltzmann transport code is formulated that is capable of accurately modeling heat flow in nanoscale crystalline devices. The scope and structure of this thesis is now presented.

1.2 Scope of Thesis

The remainder of this work is organized as follows. First, current computational modeling techniques for nanoscale thermal transport are reviewed in Ch. 2. These techniques can be roughly categorized as first principles methods, molecular dynamics methods, and Boltzmann transport simulations. The strengths, weaknesses, and regime of applicability for each technique is covered. Boltzmann transport equation algorithms that appear in literature are discussed in more detail in order to distinguish how the method presented in this thesis differs from existing methodologies.

Following the literature review, the fundamentals of lattice dynamics and phonon physics theory are presented in Ch. 3. Important concepts related to vibrational modes in crystalline materials as well as nanoscale energy transport are discussed. Examples of several key concepts are presented via simple one-dimensional examples, which avoids obfuscating the underlying physics. The concepts covered in the theoretical section, though not complete, form the basis for understanding the algorithm presented in later sections.

Chapter 4 details the Boltzmann transport equation algorithm as it has been implemented into a FORTRAN90 code. First the molecular dynamics simulations used for generating phonon inputs are discussed as well as the basis for the form of the phonon relaxation times. Subsequently, the numerical discretization of the Boltzmann transport equation is presented. The control volume discretization scheme is briefly discussed as well as the upwinding approximation for discretizing

the spatial operator. The computational implementation of various boundary conditions are detailed and supported through physical arguments. Finally, specifics to the computational implementation, such as parallelization techniques and the iterative solver, are discussed.

A variety of simulation results are presented in Ch. 5. First a simulation of semi-ballistic transport is performed via the plane parallel problem borrowed from the field of radiation transport physics. The simulation results are then compared to known semi-analytical solutions in order to verify the BTE code. Once the mathematical accuracy of the algorithm has been verified, the improvement over existing computational techniques is demonstrated. This is shown through simple transport problem highlighting the result of accounting for Brillouin zone anisotropy. The final set of simulations is a parameter study of a nanoscale transistor device known as a FinFET, a schematic of a FinFET is presented in Fig. 1.1. This device is gaining adoption in top of the line integrated circuits, and due to the nanometer dimensions and non-planar geometry requires modeling which accounts for three dimensional temperature gradients as well as anisotropy in the heat flow.

The final section reiterates the main points of the thesis. The improvements demonstrated by the algorithm are restated. In addition a path forward is detailed for improving the method through inclusion of material interfaces, time stepping, and OpenMPI parallelization.

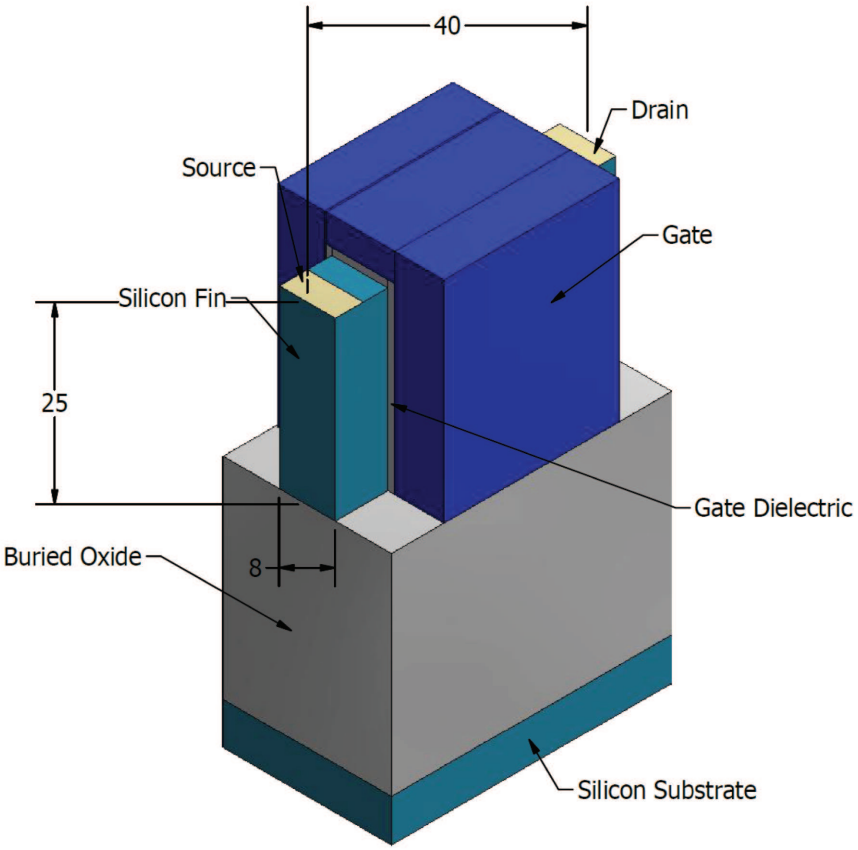

Figure 1.1: Schematic of a typical FinFET device. The dimensions are in units of nanometers and are obtained from [29].

Chapter 2: Literature Review

Modeling of subcontinuum effects is important for predicting thermal behavior of nanoscale devices, the length and time scales of interest render experimental techniques difficult or infeasible for many cases. Rapid increase in computing power over the past few decades has allowed for increasingly complex computational models of nanoscale heat transport. Computational models are not hindered by the practical restrictions of experimental techniques attempting to probe nanometer length scales or picosecond time scales and thus present an attractive alternative to experiment. In addition computational techniques are inexpensive as computing time is cheaper and often faster than experimental alternatives, albeit with reduced accuracy.

There exist a wide range of computational methods for modeling thermal behavior at the nanoscale. Within the next section these various computational methods will be detailed; with special attention paid to methods similar to the one utilized in this work so that differences may be clearly stated. Each method has inherent strengths and weaknesses as well as different length scales at which the method is applicable. The three main computational methods that will be discussed are: first-principles calculations, Molecular Dynamics simulations, the Boltzmann transport equation.

2.1 First Principles Calculations

First principles or *Ab-Initio* methods seek to directly apply physical equations and concepts to systems of interest. One manner in which *Ab-Initio* methods are used in the context of determining vibrational and heat transport properties at the nanoscale, is through determination of the exact response of electrons in the crystal to displacements of atomic nuclei. The electronic response yields parameter free force constants, which in turn allows for the determination of vibrational and transport properties [30]. Alternatively if the system is sufficiently one dimensional and without impurities, Landauer Formalism may be used to calculate heat flow.

The most prevalent computational methods for determining electronic response for use in the first principles framework is Density Functional Theory (DFT), and the closely related Density Functional Perturbation Theory (DFPT) [31–35]. DFT allows for calculation of the ground state electronic structure for a many body system, which allows for direct calculation of phonon properties such as phonon frequencies, heat capacity, and harmonic force constants [33]. DFPT extends this approach to calculate higher order perturbations to the system in order to extract anharmonic force constants as well as phonon lifetimes [36]. Phonon properties obtained from DFT and DFPT are most often used as inputs for the determination of thermal conductivity within the first principles framework [37]. Furthermore, these properties may be used as inputs to the Boltzmann transport equation for accurate device modeling. DFT/DFPT calculations may be performed using open source computer codes such as Quantum Espresso [38], however calculation is restricted to

structures with a small number of atoms and becomes prohibitively computationally expensive for large systems.

Another first principles technique that is prevalent for the prediction of nanoscale thermal transport is the Landauer formula. The Landauer formula allows for the prediction of the heat current in nanojunctions. This has application to one-dimensional systems such as nanowires and nanotubes [39]. The fundamental quantity of importance in determining the thermal current is determination of the *transmission coefficient* which describes how efficiently thermal energy is transported through a junction connected to two thermal leads. The transmission coefficient is dependent on the thermal properties of the material of interest [40]. One method of calculating the transmission coefficient is through non-equilibrium Green's function. Landauer formalism, as this approach is called, is valid when there are hundreds of atoms, or fewer, between the two leads. At this length scale energy is transported via waves and the phonon particle viewpoint is not necessarily valid. However, use of the Landauer formula is restricted to small system sizes that are predominantly one-dimensional [39].

2.2 Molecular Dynamics

Molecular dynamics is another commonly used method for nanoscale heat transport. The molecular dynamics method uses an analytic equation describing the interatomic potential of a material to integrate the Newtonian equations of motion, allowing for the evolution of atomic nuclei in time and space. By treating the atomic

nuclei as hard spheres, which evolve according to Newtonian equations of motion, molecular dynamics is a classical method and therefore one must exercise caution as to the regime it is applied. In the case of lattice thermal conductivity it has been found that molecular dynamics simulations compare well with experiment down to one-tenth of the Debye temperature of a material [41]. Molecular dynamics by design models the dynamics of individual atoms and has a wide range of applications such as thermal transport, molecular assembly, chemical reactions, and material fracture [42–47].

An important consideration when performing a molecular dynamics simulation of thermal transport is in selecting the appropriate interatomic potential. Empirical potentials often include fitting parameters which are fitted through comparison of quantities such as melting temperature, lattice constant, or liquid structure to known experimental data. However, an empirical potential which accurately predicts the melting point of a crystal may not accurately predict the same crystal's phonon transport properties. Therefore, recent work has focused on fitting existing empirical potentials to certain properties that better predict transport characteristics. One example of this type of research is fitting the Stillinger-Weber potential, initially developed to describe the liquid phase of silicon, to inter-atomic force constants in silicon derived from DFT simulations [48]. The resulting phonon frequencies predicted through the modified empirical potential give much closer agreement to experiment than the original model. Thus DFT simulations may be used to modify the parameters of an interatomic potential so that molecular dynamics simulations yield more accurate predictions of thermal transport properties.

Molecular dynamics simulations are used to determine a wide variety of phonon properties for use as inputs to thermal transport simulations. Examples of these properties include: frequencies, group velocities, phonon lifetimes, density of phonon states, and specific heats. One benefit of using molecular dynamics to extract these properties is that assumptions inherent in other methods of obtaining vibrational properties (see lattice dynamics in Ch. 3) are avoided in molecular dynamics [49]. Furthermore, molecular dynamics methods are often less computationally expensive than DFT methods. Phonon properties extracted from molecular dynamics have been used for the determination of thermal conductivities through the Green-Kubo method [50], as well as for inputs to Boltzmann Transport simulations [51].

In addition to accurate determination of phonon properties, molecular dynamics has been used to study the transmission and reflection of phonon wave-packets at interfaces of dissimilar materials as well as grain boundaries [52]. Previous models for predicting how phonon are transmitted and reflected at material boundaries, such as the acoustic mismatch model and the diffuse mismatch model, failed to accurately capture transmission and reflection. The technique detailed in [52] specifies the initial position and momenta of the atoms within a material in order to form a phonon wavepacket of defined wavevector and polarization. The wavepacket is then launched toward an interface where transmission and reflection are observed. This technique allows for the determination of wavevector and polarization specific transmission and reflection coefficients. Furthermore, mode conversion due to interface scattering may also be studied using this technique.

Molecular dynamics has proven to be an extremely useful tool for the modeling of nanoscale thermal transport. It is orders of magnitude less computationally demanding than DFT calculations while still capturing effects on the length scale of individual atoms. In addition, by its very nature molecular dynamics is able to capture the full anharmonicity of the interatomic potential (unlike harmonic lattice dynamics) which allows for more accurate predictions of phonon properties. However, molecular dynamics is still restricted to system sizes with less than a billion atoms due to its computational expense. In addition the classical nature of the method means the ensemble is governed by Boltzmann statistics rather than Bose-Einstein statistics meaning accuracy is lost when quantum effects become important [53]. Therefore, alternative techniques are required for larger systems as well as simulations at low temperature. One such technique is the Boltzmann transport equation.

2.3 Boltzmann Transport Equation

The Boltzmann equation was first formulated by Ludwig Boltzmann to describe the statistical distribution of a dilute gas system. However, the theory was expanded to describe any system with an equilibrium statistical distribution, such as electrons, phonons, or photons [54]. Rudolf Peierls first derived the phonon form of the Boltzmann Transport Equation (BTE), which in its most general form is

written as [55]:

$$\frac{\partial f}{\partial t} + \boldsymbol{v}_g \cdot \nabla_{\boldsymbol{r}} f = \left(\frac{\partial f}{\partial t}\right)_{collision} \qquad (2.1)$$
$$f = f(\boldsymbol{r}, \boldsymbol{k}, p, t) \quad ,$$

where f represents the phonon distribution function, i.e. the number of phonons within the infinitesimal spatial region $(\boldsymbol{r}, \boldsymbol{r} + d\boldsymbol{r})$ with a wavevector in the infinitesimal region of momentum space $(\boldsymbol{k}, \boldsymbol{k} + d\boldsymbol{k})$ of polarization p at time t. Inspecting Eq. 2.1 reveals that the phonon ensembles time rate of change is affected through both advection as well as a collisional term accounting for carrier interactions, isotope scattering, as well as boundary scattering. It is this equation that modeling techniques using Boltzmann transport theory seek to solve through a wide range of methodologies.

2.3.1 Monte Carlo Method

Monte Carlo simulation is a particle based method with applications to several physical phenomenon, including neutron, radiative, electron, and thermal transport [23, 56–58]. As applied to nanoscale heat transport the Monte Carlo method utilizes random sampling to trace the path of particles, representing phonons, within a domain. The random sampling process determines how long the particles travel before scattering, the type of scattering the particles undergo, and the frequency of the newly created particle. By simulating a large number of particles for a sufficiently long length of time, relevant statistics may be extracted to give the phonon distribution within the domain. Despite the probabilistic nature of the Monte Carlo

method, an accurate solution to the governing equation is obtained in the limit of sampling an infinite number of particles [23]. The Monte Carlo method is amenable to solution of the BTE as it is well suited to obtaining the solution to a differential equation for a function of many variables such as the distribution function (f in Eq. 2.1) in the Boltzmann transport equation. The basic algorithm of any Monte Carlo implementation involves a drift step in which particles are advected through space, using the left hand side of Eq. 2.1, followed by a collisional where scattering occurs, modeled by the right hand side of Eq. 2.1.

One of the earliest works which used Monte Carlo techniques to solve the BTE was performed by Mazumder and Majumdar (2001). They simulated phonons by tracing representative particles in a spatial domain, explicitly accounting for phonon dispersion. The scattering events were drawn from probability distribution functions constructed from Normal and Umklapp process relaxation times. This technique was used to predict in plane thermal conductivity of thin silicon films. Conductivities predicted through this method were in excellent agreement with experimental values [24].

A major drawback of the Monte Carlo method is its unfavorable scaling characteristics with regards to reducing the statistical uncertainty of the numerical solution. This means that in order to obtain a solution with half the variance in the temperature and heat flux fields, four times the particles must be simulated [59]. Recent work in the area of Monte Carlo simulation method for solving the phonon BTE have utilized a variance reduction technique referred to as the deviational formulation [59]. This technique only simulates the particles which deviate from the

known analytical form of the equilibrium distribution. As a result very "small" signals may be resolved with over four orders of magnitude computational speed up versus traditional methods. Monte Carlo methods utilizing this variance reduction approach have been used for the simulation of three dimensional nanoscale devices under the isotropic assumption [59].

2.3.2 Equation of Phonon Radiative Transfer

The equation of phonon radiative transfer (EPRT) was first developed by Majumdar [60]. This method exploits the similarity between photons and phonons to express the phonon BTE in terms of a phonon intensity, $I_\omega(\hat{\boldsymbol{s}}, \boldsymbol{r}, t)$ where I_ω represents the phonon energy flux in the direction $\hat{\boldsymbol{s}}$ within the frequency interval $(\omega,\ \omega + d\omega)$. The appeal of the EPRT representation rests in the wide range of numerical methods that already exist in the radiation transport literature which may be easily adopted for solving the EPRT. Numerical solution techniques for the EPRT include the control angle discrete ordinates method (CADOM) [25] and the finite difference method [61].

The EPRT has been used for simulations involving transport in thin film as well as device modeling. It is capable of capturing transport on several different length scales ranging from a few nanometers where transport is completely ballistic, to micrometers where transport is diffusive in nature. In addition the EPRT is a starting point for the derivation of continuum heat transport equations including Fourier equation and the hyperbolic heat equation. One severe drawback of the

EPRT is that by its formulation it is an isotropic method and therefore does not account for anisotropy of phonon properties within the Brillouin zone. Therefore, the EPRT is only strictly valid for simulations where isotropic transport is a valid assumption.

2.3.3 Lattice Boltzmann Method

The lattice Boltzmann method is a deterministic particle based method first formulated for fluid mechanics simulations. It has since been developed into a form for solving the BTE, called the Lattice Boltzmann Kinetic Equation (LBKE) [62]. The lattice Boltzmann method discretizes the spatial domain into discrete nodes and then solves the BTE by approximating the derivatives through finite differencing. One of the drawbacks of the lattice Boltzmann method is the finite travel directions that result from discretizing the spatial domain. This can lead to non-physical behaviors where phonons propagate faster than their group velocity in some directions. Additionally, in ballistic transport regimes the lack of available transport directions can manifest itself in "ray effects" where energy is never allowed to reach certain regions of the domain [63].

The lattice Boltzmann method has been used to determine both cross plane, as well as in plane thermal conductivity of a silicon thin film, [26] and [28]. Due to the difficulty in probing thermal conductivity experimentally on this scale, no experimental results exist for comparison. However, results from the lattice Boltzmann method used in [26,28] may be compared to thermal conductivity values obtained un-

der a wide range of simplifying assumptions such as the gray approximation and the isotropic assumption. It was discovered that the isotropic assumption can produce thermal conductivity values with up to 25 percent error, highlighting the importance of accounting for Brillouin Zone anisotropy [26]. However, despite accounting for anisotropy the results in this study were obtained only for one-dimensional heat transport.

A variety of solution techniques to the Boltzmann transport equation have been presented in this section. These modeling techniques have grown more sophisticated over the years in an effort to capture the wide array of phonon physics that are present within crystalline materials. In addition three dimensional simulations have begun to appear in order to model devices with more complex geometries [25,59,64]. However despite the sophistication of the modeling methods detailed in this section, the literature does not contain a modeling method which captures the anisotropy of the Brillouin Zone within the framework of solving the Boltzmann transport equation in a three dimensional nanoscale device. In this thesis such a technique will be presented. The next section covers the fundamental physics of phonon transport in crystalline materials, this physics is then implemented into a Boltzmann transport solver.

Chapter 3: Theory

3.1 Direct Space Lattice

The defining feature of a crystalline material is the periodic array of atoms of which it is composed. The spatial locations of these atoms are completely defined by a crystal lattice along with an associated basis. The crystal lattice is a regular array of points in one, two, or three dimensional space. The basis refers to a group of atoms attached to each lattice point, where the group may consist of one atom, a few atoms, or even entire molecules. Encapsulating the atoms which form a single basis is a unit cell. The crystalline material is constructed through a tiling of these unit cell with each unit cells containing the exact same basis of atoms. Fig. 3.1 contains a diagram of a two dimensional crystal. There are many types of crystal lattice systems [30], however this work deals primarily with materials that exhibit cubic crystal lattices. There are three types of cubic crystal lattices: simple cubic (SC), body-centered cubic (BCC), and face-centered cubic (FCC), a diagram of all three lattice types is given in Fig. 3.2. Common semiconductor materials such as silicon and germanium exhibit an FCC structure.

A crystal lattice may be completely defined through primitive lattice vectors $(\boldsymbol{a}_1, \boldsymbol{a}_2, \boldsymbol{a}_3)$, where the location of any point in the lattice is given by a lattice vector

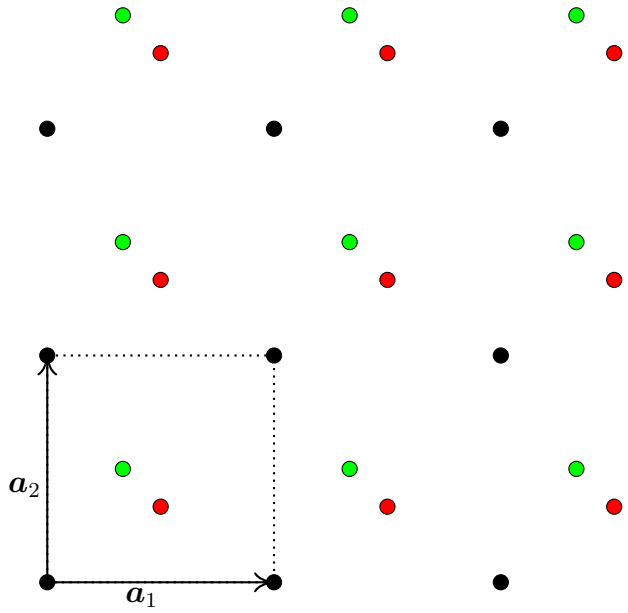

Figure 3.1: A two dimensional crystalline material with a three atom basis. $\boldsymbol{a}_1$ and $\boldsymbol{a}_2$ are the direct lattice vectors. The dotted region denotes a single unit cell, each unit cell is associated with a lattice point and contains a three atom basis (denoted black, red, and green)

$\boldsymbol{T}$,

$$\boldsymbol{T} = n_1\boldsymbol{a}_1 + n_2\boldsymbol{a}_2 + n_3\boldsymbol{a}_3 \qquad n_1, n_1, n_1 \in \boldsymbol{Z} \ . \tag{3.1}$$

The crystal lattice is invariant under any translation by a lattice vector, meaning that all points in a lattice are equivalent. The primitive lattice vectors for the three types of cubic lattices are as follows:

SC	BCC	FCC
$\boldsymbol{a}_1 = a\hat{\boldsymbol{x}}$	$\boldsymbol{a}_1 = \frac{a}{2}(-\hat{\boldsymbol{x}} + \hat{\boldsymbol{y}} + \hat{\boldsymbol{z}})$	$\boldsymbol{a}_1 = \frac{a}{2}(\hat{\boldsymbol{y}} + \hat{\boldsymbol{z}})$
$\boldsymbol{a}_2 = a\hat{\boldsymbol{y}}$	$\boldsymbol{a}_2 = \frac{a}{2}(\hat{\boldsymbol{x}} - \hat{\boldsymbol{y}} + \hat{\boldsymbol{z}})$	$\boldsymbol{a}_2 = \frac{a}{2}(\hat{\boldsymbol{x}} + \hat{\boldsymbol{z}})$
$\boldsymbol{a}_3 = a\hat{\boldsymbol{z}}$	$\boldsymbol{a}_3 = \frac{a}{2}(\hat{\boldsymbol{x}} + \hat{\boldsymbol{y}} - \hat{\boldsymbol{z}})$	$\boldsymbol{a}_3 = \frac{a}{2}(\hat{\boldsymbol{x}} + \hat{\boldsymbol{y}})$

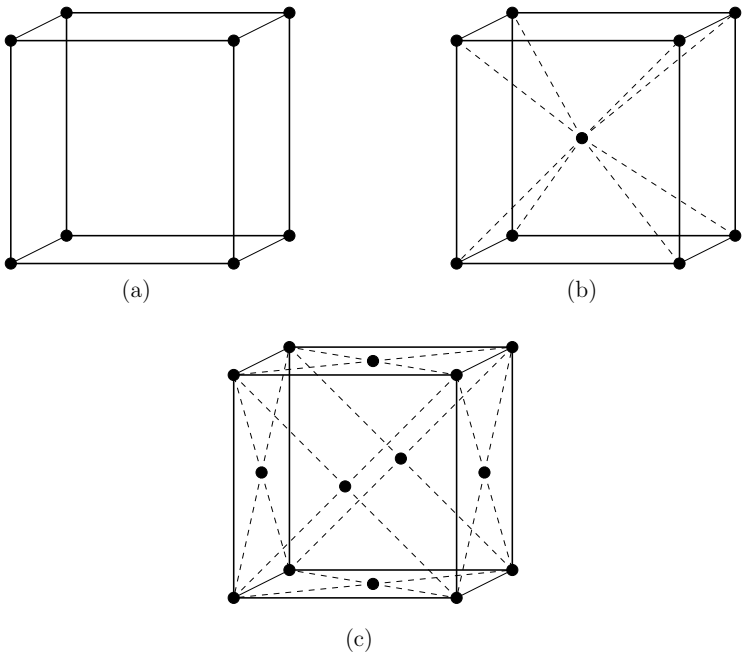

Figure 3.2: Cubic lattice structures: (a) simple cubic lattice where atoms lie at the vertices only, (b) body-centered cubic (BCC) where atoms lie at the vertices as well as the cell centroid, (c) face-centered cubic (FCC) where atoms lie at the vertices as well as the face centers.

The direct lattice in conjunction with the basis completely describe the equilibrium positions of all atoms within a material. However, in reality atoms do not lie stationary at their equilibrium positions, but rather oscillate about their equilibrium positions with some finite displacement. The mathematical apparatus for describing these lattice vibrations is called lattice dynamics and will be the focus of the Sec. 3.3.

3.2 Reciprocal Space Lattice and Brillouin Zone

In addition to a direct space lattice, the concept of a reciprocal space lattice proves extremely useful towards understanding the physics underlying phonon transport. The reciprocal lattice is completely defined by the reciprocal lattice vectors $(\boldsymbol{b}_1, \boldsymbol{b}_2, \boldsymbol{b}_3)$, where all points in the reciprocal space lattice may be written in the form,

$$\boldsymbol{G} = k_1\boldsymbol{b}_1 + k_2\boldsymbol{b}_2 + k_3\boldsymbol{b}_3 \qquad k_1, k_2, k_3 \in \boldsymbol{Z} \ . \tag{3.2}$$

The reciprocal space lattice vectors are related to the real space lattice vectors through:

$$\boldsymbol{b}_i = 2\pi \frac{\boldsymbol{a}_j \cdot \boldsymbol{a}_k}{|\boldsymbol{a}_i \cdot (\boldsymbol{a}_j \times \boldsymbol{a}_k)|} \ . \tag{3.3}$$

The reciprocal lattice vectors for each cubic type are:

SC	BCC	FCC
$\boldsymbol{b}_1 = \frac{2\pi}{a}\hat{\boldsymbol{x}}$	$\boldsymbol{b}_1 = \frac{2\pi}{a}(\hat{\boldsymbol{y}} + \hat{\boldsymbol{z}})$	$\boldsymbol{b}_1 = \frac{2\pi}{a}(-\hat{\boldsymbol{x}} + \hat{\boldsymbol{y}} + \hat{\boldsymbol{z}})$
$\boldsymbol{b}_2 = \frac{2\pi}{a}\hat{\boldsymbol{y}}$	$\boldsymbol{b}_2 = \frac{2\pi}{a}(\hat{\boldsymbol{x}} + \hat{\boldsymbol{z}})$	$\boldsymbol{b}_2 = \frac{2\pi}{a}(\hat{\boldsymbol{x}} - \hat{\boldsymbol{y}} + \hat{\boldsymbol{z}})$
$\boldsymbol{b}_3 = \frac{2\pi}{a}\hat{\boldsymbol{z}}$	$\boldsymbol{b}_3 = \frac{2\pi}{a}(\hat{\boldsymbol{x}} + \hat{\boldsymbol{y}})$	$\boldsymbol{b}_3 = \frac{2\pi}{a}(\hat{\boldsymbol{x}} + \hat{\boldsymbol{y}} - \hat{\boldsymbol{z}})$

Reciprocal space may be conceptualized as the space of vibrational modes in a material. A point in reciprocal space is mapped by a wavevector $\boldsymbol{k}$, analogously to a point in real space being mapped by a position vector $\boldsymbol{r}$. The wavevector $\boldsymbol{k}$ corresponds to a certain vibrational mode, i.e. simple harmonic motion of all the atoms in a material at some characteristic frequency ω. It can be shown that all physically distinct vibrational modes correspond to a wavevector within the first *Brillouin zone*. The first Brillouin zone for a given crystal structure is constructed by connecting the origin in reciprocal space to all lattice points in reciprocal space by a line and then bisecting these lines with perpendicular planes. In doing so, the zone created about the origin is called the first Brillouin Zone, see Fig. 3.3 for the first Brillouin zone of the FCC crystal lattice.

3.3 Lattice Dynamics

Lattice dynamics describes the dynamical motion of the atoms within a crystalline material. To determine the dynamics of all atoms within a crystal, the potential energy function of the entire crystal is differentiated to give the forces on

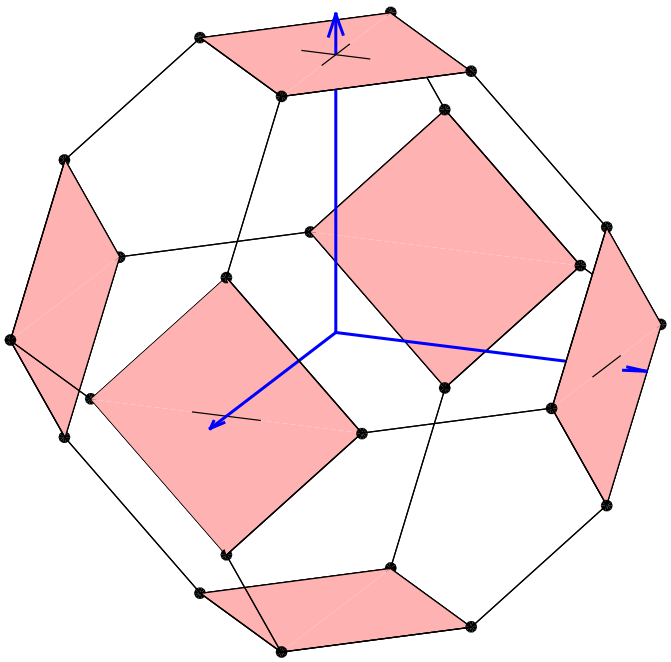

Figure 3.3: First Brillouin zone of a Face Centered Cubic crystal lattice

each atom, leading to equations of motion. Solving these equations of motion leads to the atomic displacements being governed by waves of vibrational motion, where each wave is characterized by wavevector, $\boldsymbol{k}$, and branch, λ.

Consider the potential energy $\mathcal{V}$ of a crystal. $\mathcal{V}$ is assumed to be a function of the instantaneous positions of each atom within the crystal and is minimized when all atoms occupy their equilibrium positions. Expanding $\mathcal{V}$ in a Taylor series about the equilibrium positions of the atoms leads to,

$$\mathcal{V} = \mathcal{V}_0 + \sum_{\substack{i \\ p}} \sum_{\alpha} \left. \frac{\partial \mathcal{V}}{\partial r_\alpha(ip)} \right|_0 u_\alpha(ip,t) + \frac{1}{2} \sum_{\substack{i \; i' \\ p \; p'}} \sum_{\alpha\beta} \left. \frac{\partial^2 \mathcal{V}}{\partial r_\alpha(ip) \partial r_\beta(i'p')} \right|_0 u_\alpha(ip,t) u_\beta(i'p',t) + \cdots \quad . \tag{3.4}$$

In the above equation $r_\alpha(ip)$ is the α Cartesian component of the position vector of the p-th atom in the basis attached to the lattice point labeled by i, while $u_\alpha(ip,t)$ is the time dependent displacement of the Cartesian component α of atom (ip) from equilibrium. The first term of Eq. 3.4, $\mathcal{V}_0$, refers to the potential energy of the crystal when all atoms are in their equilibrium position and is a constant representing the energy of the lattice once all vibrations have been frozen out. This term does not affect the dynamical motion of the lattice as it adds nothing to the force experienced by each atom. The second term corresponds to the force felt by the atoms at equilibrium, and is trivially zero since the Taylor expansion is taken about each atom's equilibrium positions. Thus the third, or harmonic, term in the expansion is the first to contribute a force on the atoms. Furthermore, if the atomic displacements are small then higher order terms in the potential expansion may be neglected in what is referred to as the *harmonic approximation*.

The forces on each atom are found by taking the negative gradient of the harmonic portion of the potential energy, leading to the following equation of motion for an atom:

$$\begin{aligned} m_p \ddot{u}_\alpha(ip,t) = & -\sum_{\substack{i' \\ p'}} \sum_{\beta} \Phi_{\alpha,\beta}(ip;i'p')\ u_\beta(i'p',t) \\ \Phi_{\alpha,\beta}(ip;i'p') = & \left.\frac{\partial^2 \mathcal{V}}{\partial r_\alpha(ip)\partial r_\beta(i'p')}\right|_0 \end{aligned} \tag{3.5}$$

where the force constant matrix $\Phi(ip;i'p')$, characterizing the forces between atoms (ip) and $(i'p')$, has been introduced. This is a differential equation which is com-

monly solved through an ansatz, such as the one introduced in [30],

$$u_\alpha(ip,t) = \sum_{\boldsymbol{k}} U_\alpha(\boldsymbol{k}p) e^{i(\boldsymbol{k}\cdot\boldsymbol{R}_i - \omega t)} \ , \tag{3.6}$$

here $\boldsymbol{R}_i$ is the spatial location of the lattice point i. Note that the form of the displacement vector is a linear combination of plane waves. In addition the plane wave polarization vector $\boldsymbol{U}$ is in general complex and thus by convention the real space displacement corresponds to the real part only.

Inserting Eq. 3.6 into Eq. 3.5 and performing algebraic manipulation yields the eigenvalue equation:

$$\sum_{\substack{i' \\ p'}} \sum_{\beta} \left[\Phi_{\alpha,\beta}(ip;i'p') e^{i\boldsymbol{k}(\boldsymbol{R}_{i'} - \boldsymbol{R}_i)} - \omega^2 \delta_{p,p'} \delta_{\alpha,\beta} \right] U_\beta(\boldsymbol{k},p') = 0 \ . \tag{3.7}$$

Therefore the determination of the frequency and mode shape of the vibration associated with wavevector $\boldsymbol{k}$ is determined by solving the eigensystem of the *dynamical matrix* defined as,

$$D_{p,p'}(\boldsymbol{k}) = \sum_{i'} \Phi(1p;i'p') e^{i\boldsymbol{k}\cdot\boldsymbol{R}_{i'}} \ . \tag{3.8}$$

It is important to understand that due to the invariance of $\mathcal{V}$ under uniform translation by any lattice vector T, only the relative difference ($|\boldsymbol{R}_i - \boldsymbol{R}_{i'}|$) of two points in the lattice affect the dynamical matrix. Therefore the lattice point denoted by i may be arbitrarily set to $i = 1$ where $\boldsymbol{R}_{i=1} = \boldsymbol{0}$, this has been done in Eq. 3.8. Note that the dynamical matrix is a continuous tensor function of the wavevector $\boldsymbol{k}$ and accounts for all interactions of atom $(1p)$ with the rest of the crystal. The

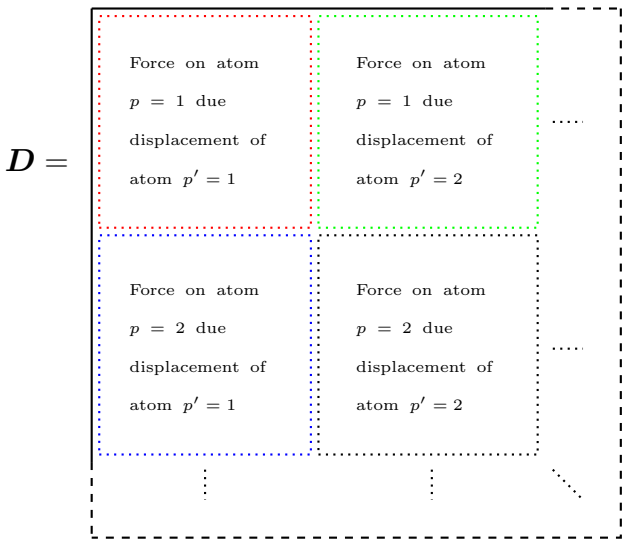

Figure 3.4: Visual depiction of what the blocks of the dynamical matrix represent in terms of forces and displacements.

dynamical matrix can be interpreted as being composed of blocks which represent the force felt by the $p-$th atom in the unit cell due to displacements by the p'-th atom in the unit cell, where each block is modulated by some phase factor. A single block of the dynamical matrix is a: 3×3 matrix for a three dimensional crystal, 2×2 matrix for a two dimensional crystal, scalar for a one dimensional crystal (see Fig. 3.4 for a visual representation).

3.3.1 1-D Example

To demonstrate how the dynamical matrix is constructed and used to obtain the vibrational properties of the lattice, consider the simple case of a one dimensional lattice with a two atom basis, the system is depicted in Fig. 3.5.

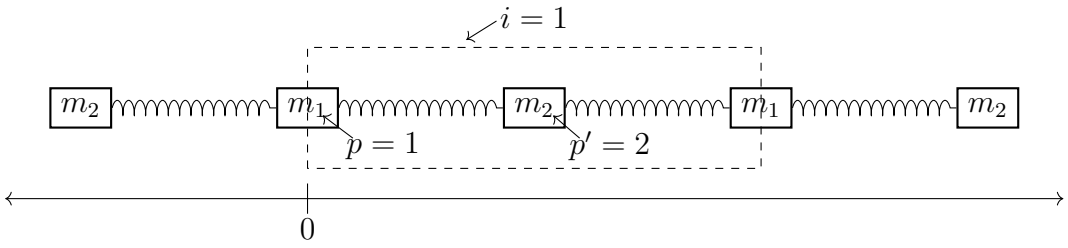

Figure 3.5: A one dimensional lattice with a two atom basis is depicted. The unit cell, labeled by $i = 1$ is denoted by dashed lines. Within this unit cell, the basis atoms have been labeled. For convenience the lattice vector of cell $i = 1$ is centered on the origin.

In the one dimensional case the dynamical matrix defined in Eq. 3.8 reduces to the simplified form:

$$\begin{aligned} D_{pp'}(k) &= \sum_{i'} \Phi(1p; i'p') e^{ikR_{i'}} \quad , \\ \Phi(1p; i'p') &= \left. \frac{\partial^2 V}{\partial r(1p) \partial r(i'p')} \right|_0 \quad , \end{aligned} \tag{3.9}$$

note that in one dimension the Cartesian component subscripts may be dropped. To proceed an interatomic potential is required to describe the interaction between atoms, for ease of presentation assume that each atom interacts only with it's nearest neighbors via a linear spring-like force, where the potential energy of each spring is given by:

$$\phi(r) = \frac{A}{2} (r - x_0)^2 \quad , \tag{3.10}$$

here A is the strength of the interatomic bond and x_0 is the equilibrium separation. Note that with this potential form the harmonic approximation is exact.

Once an analytical form for the interatomic potential has been chosen the potential energy of the entire crystal may be written in the harmonic approximation

leading to the expression,

$$\begin{aligned} V &= \frac{1}{2}\sum_{\substack{i,i'\\p,p'}} \phi\left(|r(i,p)-r(i',p')|\right) \qquad , \\ &= \frac{A}{4}\sum_{\substack{i,i'\\p,p'}} (|r(i,p)-r(i',p')|-x_0)^2 \qquad . \end{aligned} \tag{3.11}$$

From this expression the force constants are extracted by differentiating twice. Taking the first derivative with respect to an arbitrary atoms (js) yields:

$$\begin{aligned} \frac{\partial V}{\partial r(js)} = & \\ & \frac{A}{4}\sum_{\substack{i,i'\\p,p'}} \left\{ 2(|r(ip)-r(i'p')|-x_0)\left(\frac{r(ip)-r(i'p')}{|r(ip)-r(i'p')|}\left[\delta_{ij}\delta_{ps}-\delta_{i'j}\delta_{p's}\right]\right)\right\} \\ & = A\sum_{\substack{i'\\p'}} \left(|r(js)-r(i'p')|-x_0\right)\frac{r(js)-r(i'p')}{|r(js)-r(i'p')|} \qquad . \end{aligned} \tag{3.12}$$

Differentiating a second time with respect to an arbitrary atoms $(j's')$ gives the expression:

$$\begin{aligned} & \frac{\partial^2 V}{\partial r(js)\partial r(j's')} = \\ & A\sum_{\substack{i'\\p'}} \left(\frac{r(js)-r(i'p')}{|r(js)-r(i'p')|}\left[\delta_{jj'}\delta_{ss'}-\delta_{i'j'}\delta_{s'p'}\right]\right)\frac{r(js)-r(i'p')}{|r(js)-r(i'p')|} + \\ & \left(|r(js)-r(i'p')|-x_0\right)\times \\ & \left(\frac{\delta_{jj'}\delta_{ss'}-\delta_{i'j'}\delta_{s'p'}}{|r(js)-r(i'p')|} - \frac{\left(r(j,s)-r(i'p')\right)^2}{|r(js)-r(i'p')|^3}\left[\delta_{jj'}\delta_{ss'}-\delta_{i'j'}\delta_{s'p'}\right]\right) \end{aligned} \tag{3.13}$$

Evaluating eq. 3.13 at equilibrium, and taking i to be the unit cell attached to the lattice vector which coincides with the origin, i.e. $i = 1$ and $R_{i=1} = 0$, reduces the force constant expression to:

$$\Phi(1p; i'p') = \left.\frac{\partial^2 V}{\partial r(1p)\partial r(i'p')}\right|_0 = A \sum_{\substack{j \\ s}} [\delta_{1i'}\delta_{pp'} - \delta_{i'j}\delta_{p's}] \qquad . \tag{3.14}$$

Once the force constants have been extracted from the chosen interatomic potential the dynamical matrix is formed. Inserting Eq. 3.14 into Eq. 3.9 gives the expression,

$$\begin{aligned} D_{pp'}(k) =& \sum_{i'} \Phi(1, p; i', p') e^{ikR_{i'}} \\ =& A \sum_{i'} \left(\sum_{\substack{j \\ s}} \delta_{1i'}\delta_{pp'} - \delta_{i'j}\delta_{p's} \right) e^{ikR_{i'}} \\ =& A \sum_{\substack{j \\ s}} \delta_{pp'} e^{ikR_1} - A \sum_{i'} e^{ikR_{i'}} \qquad ; \qquad R_1 = 0 \\ =& \underbrace{A \sum_{\substack{j \\ s}} \delta_{pp'}}_{\text{Term 1}} - \underbrace{A \sum_{i'} e^{ikR_{i'}}}_{\text{Term 2}} \qquad . \end{aligned} \tag{3.15}$$

Note in the the final expression the summation indices, j, s, i', range only over atoms that interact with the atom under consideration, i.e. the nearest neighbor.

It is instructive to assemble the dynamical matrix term by term to gain intuition with how atoms interact with one another. When considering the dynamical matrix one may think of term $D_{pp'}$ as a measure of the force felt by atom p due to displacement of atom p' with a phase modulation (the cells in the lattice and atoms

in the basis are labeled in Fig. 3.5). Assembling the dynamical matrix gives the following terms:

$$
\begin{aligned}
D_{11} &= \overbrace{\underbrace{A}_{\substack{j=1\\ s=2}} + \underbrace{A}_{\substack{j=0\\ s=2}}}^{\text{Term 1}} - \overbrace{0}^{\text{Term 2}} \\
D_{22} &= \overbrace{\underbrace{A}_{\substack{j=1\\ s=1}} + \underbrace{A}_{\substack{j=2\\ s=1}}}^{\text{Term 1}} - \overbrace{0}^{\text{Term 2}} \\
D_{12} &= \overbrace{0}^{\text{Term 1}} - \overbrace{\underbrace{Ae^{ik0}}_{\substack{\text{interaction}\\ \text{of atom 1}\\ \text{w/ atom 2}\\ \text{in cell 1}}} - \underbrace{Ae^{-ik}}_{\substack{\text{interaction}\\ \text{of atom 1}\\ \text{w/ atom 2}\\ \text{in cell 0}}}}^{\text{Term 2}} \\
D_{21} &= \overbrace{0}^{\text{Term 1}} - \overbrace{\underbrace{Ae^{ik0}}_{\substack{\text{interaction}\\ \text{of atom 2}\\ \text{w/ atom 1}\\ \text{in cell 1}}} - \underbrace{Ae^{-ik}}_{\substack{\text{interaction}\\ \text{of atom 2}\\ \text{w/ atom 1}\\ \text{in cell 2}}}}^{\text{Term 2}} \quad .
\end{aligned}
\tag{3.16}
$$

Thus the fully assembled dynamical matrix has the form:

$$
D(k) = \begin{bmatrix} 2A & -A\left(1+e^{-ik}\right) \\ -A\left(1+e^{ik}\right) & 2A \end{bmatrix} \quad . \tag{3.17}
$$

3.3.2 Vibrational Properties

The dynamical matrix contains information about several fundamental vibrational properties of the lattice including: mode shapes, vibrational frequencies, and group velocities. The wavevector $\boldsymbol{k}$ may be thought of as enumerating the vibrational modes of the material, for each $\boldsymbol{k}$ there are n unique vibrational modes corresponding to the n eigenvector/eigenvalue pairs of the dynamical matrix, where:

$$
n = number\ of\ dimensions \times number\ of\ atoms\ in\ basis \quad .
$$

The n values of the vibrational properties at each wavevector are referred to as *branches*, where each branch may be labeled as λ. Therefore a vibrational mode is uniquely defined by a wavevector and branch, i.e. $(\boldsymbol{k}, \lambda)$

Obtaining the mode shapes and frequencies of each vibrational mode reduces to solving the generalized eigensystem:

$$\boldsymbol{DU} - \omega^2 \boldsymbol{MU} = 0, \tag{3.18}$$

where $\boldsymbol{M}$ is the diagonal mass matrix. Solving for the frequencies in the one dimensional example presented in Sec. 3.3.1 yields:

$$\begin{aligned} \omega_{ac}(k) =& \sqrt{A/(m_1 m_2)} \sqrt{m_1 + m_2 - \sqrt{m_1^2 + m_2^2 + 2m_1 m_2 \cos(k)}} \\ \omega_{op}(k) =& \sqrt{A/(m_1 m_2)} \sqrt{m_1 + m_2 + \sqrt{m_1^2 + m_2^2 + 2m_1 m_2 \cos(k)}} \end{aligned} \quad , \tag{3.19}$$

for a plot of these values, see Fig. 3.6. The two distinct frequencies per wavevector, a result of the two atom basis, are said to belong to either the *acoustic* or *optical* branches. The naming convention stems from the fact that sound waves in a material correspond to the acoustic branch, while the high energy optical branch may be excited by photons in certain ionic crystals [65]. The dispersion curves, i.e. the wavevector-frequency relations, for the linear chain display qualitative behavior which extend to more general three dimensional lattices. One such behavior is that at the center of the Brillouin zone there will always be certain branches that tend to

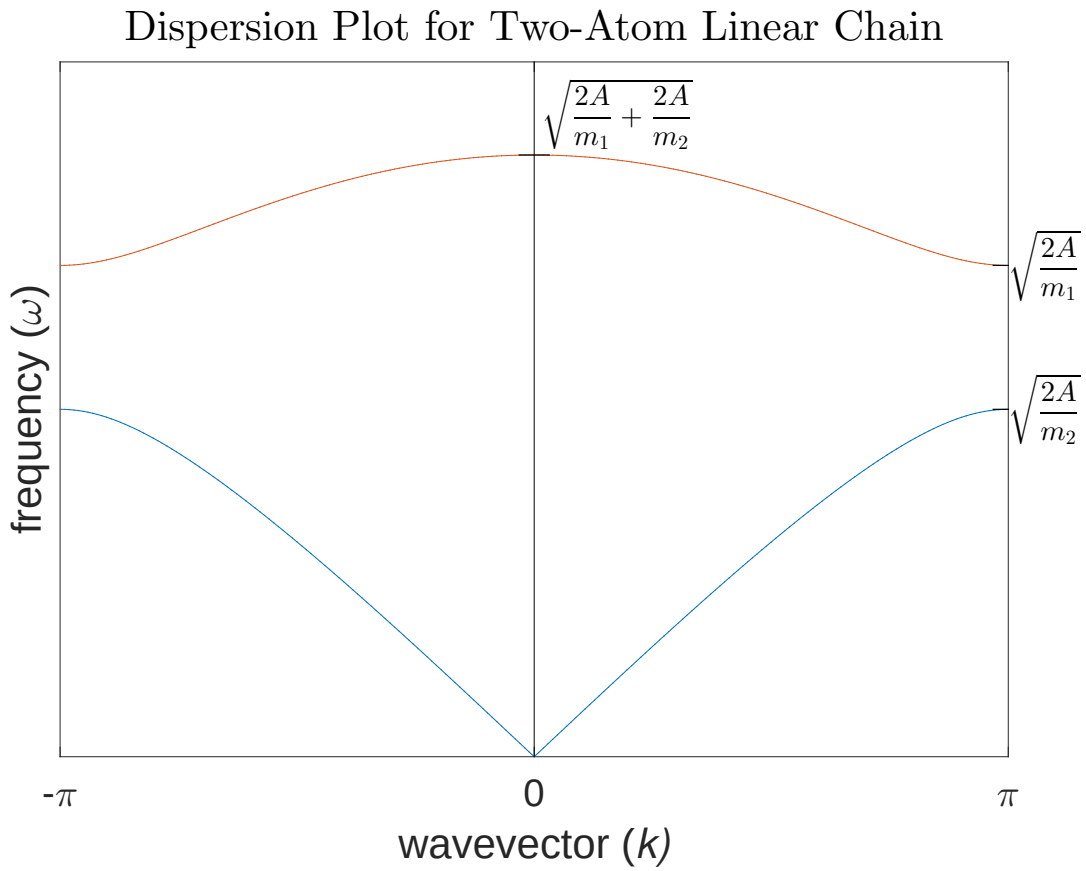

Figure 3.6: Frequencies of the acoustic (yellow line) and optical (blue line) modes.

0, i.e. the acoustic modes, while the other branches will tend towards a maximum frequency, i.e. the optical modes. Conversely, all branches level out at the Brillouin zone edge and their slopes approach 0.

In addition to vibrational frequency, group velocity v_g is an inherent property of a vibrational mode. The group velocity characterizes the speed at which energy within a vibrational mode travels, and defined as:

$$\boldsymbol{v}_g = \nabla_{\boldsymbol{k}}\, \omega \tag{3.20}$$

Applying this to our one dimensional example yields the following group velocity equations for the linear chain:

$$v_{g,ac}(k) = -\frac{\sqrt{A\ m_1\ m_2}\sin(k)}{2\sqrt{m_1^2+m_2^2+2m_1m_2\cos(k)}\sqrt{m_1+m_2-\sqrt{m_1^2+m_2^2+2m_1m_2\cos(k)}}}$$

$$v_{g,op}(k) = -\frac{\sqrt{A\ m_1\ m_2}\sin(k)}{2\sqrt{m_1^2+m_2^2+2m_1m_2\cos(k)}\sqrt{m_1+m_2+\sqrt{m_1^2+m_2^2+2m_1m_2\cos(k)}}}\ , \tag{3.21}$$

for a plot of these values, see Fig. 3.7. The group velocities of the linear chain also display behavior that is common to general three dimensional lattices. Namely the velocity of the acoustic modes is maximum at the Brillouin zone center, while the optical mode's group velocity becomes zero. In addition the group velocity of both modes decrease towards the Brillouin zone edge, although in real crystals the group velocity does not always vanish at the Brillouin zone boundary as it does here.

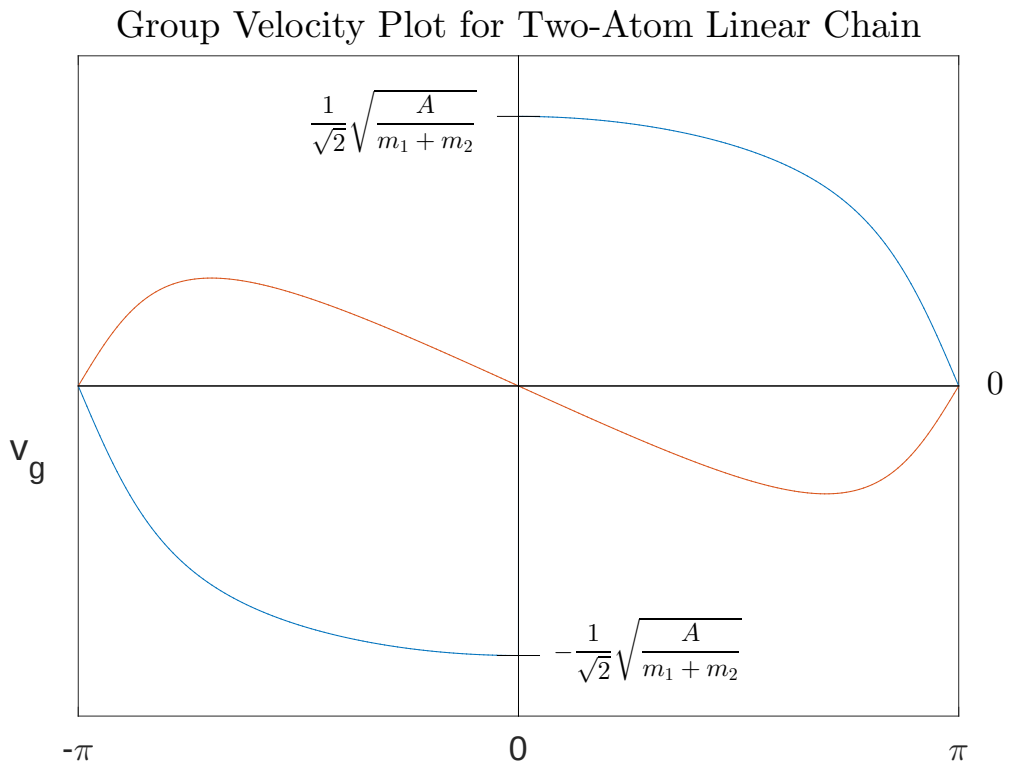

Figure 3.7: Group velocity of the acoustic (yellow line) and optical (blue line) branches.

3.4 Quantum Nature of Phonons

Individual vibrational modes, characterized by a wavevector $\boldsymbol{k}$ and branch index λ, represent a collective motion of lattice ions where the vibrational modes are decoupled from one another within the harmonic approximations. Therefore, each mode may be described quantum mechanically by the harmonic oscillator Hamiltonian:

$$H_{\boldsymbol{k},\lambda} = \hbar\omega_{\boldsymbol{k},\lambda}\left(\hat{N}_{\boldsymbol{k},\lambda} + \frac{1}{2}\right) \quad , \tag{3.22}$$

where $\hat{N}_{\boldsymbol{k},\lambda}$ is the number operator that gives the quanta of energy, or number of *phonons*, in the mode $(\boldsymbol{k}, \lambda)$, for a derivation of this expression see [65]. A well known property of a harmonic oscillator is that the the energy levels are quantized [66] and may be written in the form:

$$E_{\boldsymbol{k},\lambda} = \left(N_{\boldsymbol{k},\lambda} + \frac{1}{2} \right) \hbar \omega_{\boldsymbol{k},\lambda} \ , \tag{3.23}$$

where $N_{\boldsymbol{k},\lambda}$ represents the number of phonons of the quantum state $(\boldsymbol{k}, \lambda)$.

Interpreting phonons as a quantum of energy for de-localized lattice vibration is referred to as the wave description of phonons, this is because a phonon wavefunction is of the form of a plane wave. However, there exists an alternative interpretation known as the particle description of phonons [67]. The particle description seeks to localize phonons both in real space, as well as in wavevector space. In order to localize a phonon for a given quantum state $(\boldsymbol{k}, \lambda)$, a phonon wave-packet is formed through a superposition of phonon wavefunctions. Each wavefunction forming the superposition has a wavevector contained in a small region of reciprocal space, $\Delta\boldsymbol{k}$, centered on the wavevector of interest $\boldsymbol{k}$ [68]. The resulting wavepacket is localized in both real and reciprocal space with a small uncertainty in both, see Fig. 3.8. It is important to note that an implicit assumption of the particle viewpoint is that enough waves exist in a lattice to form a wavepacket. It will be shown in Sec. 3.5 that this amounts to the crystal having a sufficient number of unit cells. In this work all crystals studied will be sufficiently large enough to be modeled in the particle description.

The phonon wavepacket centered at $(\boldsymbol{k}, \lambda)$ possesses the same properties as the quantum state, namely the same frequency and group velocity. Therefore, the energy of a phonon wavepacket is given by Eq. 3.23. Furthermore, the energy propagates at the group velocity $\boldsymbol{v}_g(\boldsymbol{k}, \lambda)$.

The occupation of a given mode is the quanta of energy within that mode, with respect to the particle description the occupation number is the number of wavepackets corresponding to a given mode that exist within a region of space. The differential equation governing the occupation of various phonon states was first detailed by Robert E. Peierls [55]. The time evolution of the occupation for a given phonon state is governed by the differential equation:

$$\frac{\partial N_{\boldsymbol{k},\lambda}}{\partial t} + \boldsymbol{v}_g(\boldsymbol{k}, \lambda) \cdot \frac{\partial N_{\boldsymbol{k},\lambda}}{\partial \boldsymbol{r}} = \left(\frac{\partial N_{\boldsymbol{k},\lambda}}{\partial t} \right)_{collision} \quad . \tag{3.24}$$

This expression is the phonon Boltzmann Transport Equation (BTE). It describes the time rate of change of a phonon state through advection as well as collisional terms. The collisional terms are a result of isotope scattering, boundary scattering, as well as phonon-phonon interactions. Physical justification for Eq. 3.24 is given in [67] and [55].

Once phonon properties such as vibrational frequency and group velocity have been determined, the phonon Boltzmann transport equation gives a complete description of the spatial distribution of all allowed phonon modes within the material. Therefore, the problem of phonon transport is reduced to the solution of a differential equation, or rather a set of coupled differential equations, one for each phonon

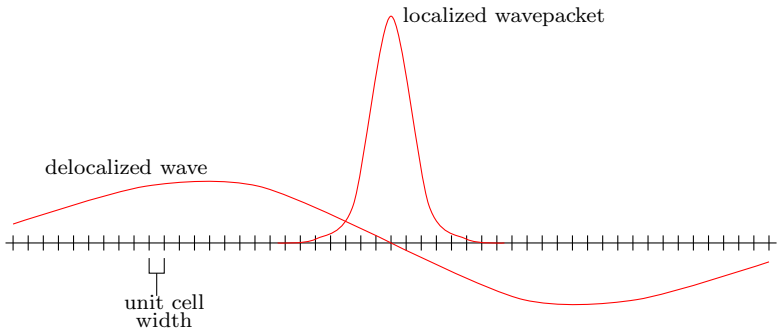

Figure 3.8: Phonon representation in the wave representation (delocalized wave), and the particle representation (localized wave packet)

mode. Once the spatial distribution of phonons is known, the temperature and energy fields within the domain are easily obtained. In the final section of this chapter the determination of the allowed phonon modes within a material are discussed.

3.5 Determination of Allowed Wavevectors

The numerical procedure detailed in Ch. 4, relies on the knowledge of phonon properties for all vibrational states available to the crystalline material being modeled in order to solve the Boltzmann transport equation for these states. In this section the process for determining the allowed vibrational states, denoted by $(\boldsymbol{k}, \lambda)$, is discussed. Furthermore, it is shown that not only are allowed wavevectors discrete in reciprocal space, but there are also a finite number of wavevectors corresponding to physically unique vibrational modes. Therefore, the continuous representation of wavevectors that is used in the vast majority of Boltzmann solvers is a simplifying assumption. For crystals of dimensions on the nanoscale it has been shown that the reduction in allowed vibrational modes do affect thermal properties [26, 28, 69] and therefore considering wavevectors as discrete is a fundamentally more accurate

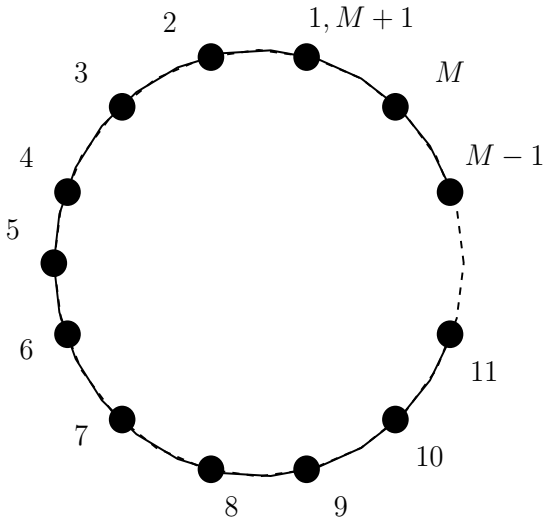

Figure 3.9: Periodic boundary conditions for a one dimensional chain with a period of M unit cells

treatment that better captures phonon physics. In the remainder of this section physical arguments are laid out, which restrict the allowed wavevectors within the first Brillouin Zone. Additionally, a more subtle point regarding the wavevectors is proven, notably that for a crystal of finite size, only a finite number of physically allowed wavevectors exist within the first Brillouin Zone.

The theory developed in Sec. 3.3 relied on the assumption that every atom experiences the same analytical form of the potential energy and therefore is in the *bulk* of the crystal far removed from any surfaces. However, this assumption relies on the crystal being infinite in extent which is non-physical as this work deals with crystals with length scales on the nanoscale. In order to reconcile these contradictory assumptions, Born Von-Karman boundary conditions are applied.

Born/Von-Karman, boundary conditions state that the crystal is periodic in M unit cells in one dimension or more generally periodic in (M_1, M_2, M_3) unit cells in three dimensions, see Fig. 3.9.

To see how the assumption of periodic boundary conditions restricts the allowed wavevectors within the Brillouin Zone, consider the ionic displacement resulting from a single vibrational mode given by Eq. 3.6,

$$u_\alpha(ip,t) = U_\alpha(\boldsymbol{k},p)e^{i(\boldsymbol{k}\cdot\boldsymbol{R}_i-\omega t)} \quad . \tag{3.25}$$

Note that a traveling wave in the crystal lattice is completely characterized by a wavevector and a polarization, $(\boldsymbol{k},\lambda)$, the latter has been omitted in the above equation but is implied.

Let the direct lattice of the crystalline material be defined by the lattice vectors $\{\boldsymbol{a}_1,\boldsymbol{a}_2,\boldsymbol{a}_3\}$. Assuming the crystal has M_1 unit cells in the $\boldsymbol{a}_1$ direction, M_2 unit cells in the $\boldsymbol{a}_2$ direction, and M_3 unit cells in the $\boldsymbol{a}_3$ direction, then the atoms in the basis attached to lattice site $\boldsymbol{R}_i$ are equivalent to the corresponding atoms in the basis attached to the lattice site $\boldsymbol{R}_i + M_1\boldsymbol{a}_1 + M_2\boldsymbol{a}_2 + M_3\boldsymbol{a}_3$ by periodic boundary conditions.

Defining $\boldsymbol{G} = M_1\boldsymbol{a}_1 + M_2\boldsymbol{a}_2 + M_3\boldsymbol{a}_3$, Eq. 3.25 implies:

$$u_\alpha(ip,t) = u_\alpha(jp,t) \quad , \tag{3.26}$$

where j indexes the lattice point $\boldsymbol{R}_i + \boldsymbol{G}$. Combining Eq. 3.26 and Eq. 3.25 leads to the relation:

$$\begin{aligned} e^{i\boldsymbol{k}\cdot\boldsymbol{R}_i} &= e^{i\boldsymbol{k}\cdot(\boldsymbol{R}_i+\boldsymbol{G})} \\ e^{i\boldsymbol{k}\cdot\boldsymbol{G}} &= 1 \\ \boldsymbol{k}\cdot\boldsymbol{G} &= 2\pi r \qquad ; \qquad r \in \mathbb{Z} \end{aligned} \tag{3.27}$$

Therefore all admissible wavevectors must obey this relation. The form of $\boldsymbol{k}$ that satisfy the relation were given in Eq. 3.3. Note the property of real space and reciprocal lattice vectors that $\boldsymbol{a}_i \cdot \boldsymbol{b}_j = 2\pi\delta_{ij}$. Finally, consider a general wavevector written as $\boldsymbol{k} = \frac{r_1}{M_1}\boldsymbol{b}_1 + \frac{r_2}{M_2}\boldsymbol{b}_2 + \frac{r_1}{M_1}\boldsymbol{b}_3$ in the context of Eq. 3.27,

$$\begin{aligned} \boldsymbol{G}\cdot\boldsymbol{k} &= (M_1\boldsymbol{a}_1 + M_2\boldsymbol{a}_2 + M_3\boldsymbol{a}_3)\cdot\left(\frac{r_1}{M_1}\boldsymbol{b}_1 + \frac{r_2}{M_2}\boldsymbol{b}_2 + \frac{r_3}{M_3}\boldsymbol{b}_3\right) \\ &= 2\pi r_1 + 2\pi r_2 + 2\pi r_3 \\ &= 2\pi r \end{aligned} \tag{3.28}$$

Therefore it is clear that the wavevectors $\boldsymbol{k} = \frac{r_1}{M_1}\boldsymbol{b}_1 + \frac{r_2}{M_2}\boldsymbol{b}_2 + \frac{r_1}{M_1}\boldsymbol{b}_3$ do satisfy periodic boundary conditions, and furthermore only wavevectors of this form correspond to physically realizable vibrational modes. Furthermore, because $r_i \in \mathbb{Z}$ the wavevectors that are allowed to exist in the crystal are discrete within reciprocal space. These wavevectors are often referred to colloquially as k-points.

To show that there are a finite number of these wavevectors, consider the atomic displacements that arise from the wavevectors:

$$\boldsymbol{k} = \frac{r_1}{M_1}\boldsymbol{b}_1 + \frac{r_2}{M_2}\boldsymbol{b}_2 + \frac{r_3}{M_3}\boldsymbol{b}_3$$
$$\boldsymbol{k}' = \frac{r_1 + M_1}{M_1}\boldsymbol{b}_1 + \frac{r_2 + M_2}{M_2}\boldsymbol{b}_2 + \frac{r_3 + M_3}{M_3}\boldsymbol{b}_3$$

Inserting the second of these wavevector into the exponential term of Eq. 3.25 yields:

$$\begin{aligned}
e^{i\boldsymbol{k}'\cdot\boldsymbol{R}_i} &= e^{i\left[\frac{r_1+M_1}{M_1}\boldsymbol{b}_1+\frac{r_2+M_2}{M_2}\boldsymbol{b}_2+\frac{r_3+M_3}{M_3}\boldsymbol{b}_3\right]\cdot\boldsymbol{R}_i} \\
&= e^{i\left[\frac{r_1}{M_1}\boldsymbol{b}_1+\frac{r_2}{M_2}\boldsymbol{b}_2+\frac{r_3}{M_3}\boldsymbol{b}_3\right]\cdot\boldsymbol{R}_i} e^{i[\boldsymbol{b}_1+\boldsymbol{b}_2+\boldsymbol{b}_3]\cdot\boldsymbol{R}_i} \\
&= e^{i\left[\frac{r_1}{M_1}\boldsymbol{b}_1+\frac{r_2}{M_2}\boldsymbol{b}_2+\frac{r_3}{M_3}\boldsymbol{b}_3\right]\cdot\boldsymbol{R}_i} e^{i[2\pi(r_1+r_2+r_3)]} \\
&= e^{i\left[\frac{r_1}{M_1}\boldsymbol{b}_1+\frac{r_2}{M_2}\boldsymbol{b}_2+\frac{r_3}{M_3}\boldsymbol{b}_3\right]\cdot\boldsymbol{R}_i} \\
&= e^{i\boldsymbol{k}\cdot\boldsymbol{R}_i} \quad ,
\end{aligned}$$

where we have used $\boldsymbol{R}_i = M_1\boldsymbol{a}_1 + M_2\boldsymbol{a}_2 + M_3\boldsymbol{a}_3$. Therefore the two wavevectors correspond to the exact same ionic displacement and are therefore equivalent. Thus all unique wavevectors are contained in the range $r_i \in \{1, 2, \ldots, M_i\}$ or any contiguous range of integers of length N_i. It is convention to choose this range to be (almost) symmetric about 0 so that $r_i \in \{-\frac{M_i}{2} + 1, -\frac{M_i}{2} + 2, \ldots, -1, 0, 1, \ldots, \frac{M_i}{2} - 1, \frac{M_i}{2}\}$. This convention restricts the wavevectors to lie within the first Brillouin zone. It has been shown that the allowed wavevectors within the Brillouin Zone are of the

form:

$$\boldsymbol{k} = \frac{r_1}{M_1}\boldsymbol{b}_1 + \frac{r_2}{M_2}\boldsymbol{b}_2 + \frac{r_3}{M_3}\boldsymbol{b}_3$$
$$r_i \in \left(-\frac{M_i}{2}+1, -\frac{M_i}{2}+2, \ldots, -1, 0, 1, \ldots, \frac{M_i}{2}-1, \frac{M_i}{2}\right) \quad . \tag{3.29}$$

These wavevectors may be determined solely from the crystal dimensions. For each of these allowed wavevectors and for all branches the phonon properties are determined and supplied as inputs to the solution of the BTE.

One final note of importance is that in addition to Born Von-Karman boundary conditions there do exist other conditions that may be imposed on the crystalline system, one example being fixed end boundary conditions. These various boundary conditions will alter the allowed vibrational modes within the system, however the wavevectors will always remain discrete as well as finite for any other condition imposed. Furthermore there will always be the same number of allowed wavevectors, or stated differently the number of degrees of freedom is unaffected by the choice of boundary conditions as it should be. Throughout the rest of this work periodic boundary conditions are assumed as it has been shown that Born Von-Karman boundary conditions are suitable for application to crystals considered in this work [70].

In this section the relevant physics governing phonons has been introduced. In order to model phonon transport in a finite system one only needs information regarding the system size, or specifically the number of unit cells in the system, as well as the empirical potential governing interatomic interactions. Knowledge of

the number of unit cells allows extraction of the allowed wavevectors as detailed in Sec. 3.5. Once wavevectors are known the dynamical matrix may be formed and the eigensystem solved for every allowable wavevector and branch, providing all necessary phonon inputs for the simulation, this process was detailed in 3.3. With the phonon properties in hand one may use the phonon BTE to simulate phonon transport for the system of interest. Though the form of the BTE is known, analytical solutions exist only for a small set of simple situations. In the next section, a general numerical approach for solving the phonon BTE is introduced which explicitly accounts for the allowed wavevectors within the anisotropic Brillouin Zone. The BTE is discretized and solved via a numerical algorithm yielding the the spatial energy density for all phonon modes. From the known phonon energy densities, energy and temperature profiles then determined.

Chapter 4: Boltzmann Transport Solver Algorithm

This chapter presents the details for implementing a method for the simulation of phonon transport via the Boltzmann transport equation. The method solves the BTE for all allowed wavevectors within the anisotropic Brillouin zone. Section 4.1 details how inputs to the BTE code are obtained. Inputs to the Boltzmann transport code include phonon frequency, group velocity, and relaxation time. In Sec. 4.2 the governing differential equation is discretized for numerical solution via the control volume method. Section 4.2.2 deals with the implemented boundary conditions and their physical basis. Finally, in Sec. 4.2.3 the specifics of the computational implementation are discussed, such as: parallelization, linear solver, and convergence criterion.

4.1 Boltzmann Solver Inputs

The Boltzmann transport solver detailed in this thesis has been written in such a manner that given a set of phonon properties, boundary conditions, and a spatial grid, the Boltzmann transport equation is solved iteratively for each allowed wavevector and all branches to obtain the steady state temperature and energy profiles within the domain of interest. While, this procedure allows the solver to

be applied to a wide range of geometries and crystalline material structures, it does require the user to determine the phonon properties and supply these as inputs. The manner in which these properties are determined is now detailed.

4.1.1 Frequencies and Group Velocities

In Ch. 3, the theoretical basis for obtaining phonon properties was presented. There, the functional expression for an interatomic potential was differentiated to obtain the dynamical matrix, along with the associated eigensystem which yields the desired phonon properties. This process while conceptually straightforward and thus useful for pedagogical purposes is difficult to implement in practicality. Often materials of interest will have complex crystalline structure with several atoms in the basis rendering the straightforward treatment exceedingly difficult as the interatomic potential will, in general, be of a very complex form. An example of such a material is the Hexahydro-1,3,5-trinitro-1,3,5-s-triazine crystal (RDX) pictured in Fig. 4.1. As a result it is much more practical to use a molecular dynamics simulator to obtain phonon inputs.

The General Utility Lattice Program (GULP) [71] is used to generate the phonon properties for every allowed wavevector and all branches within the first Brillouin zone. While GULP is capable of directly calculating the frequencies of all phonon branches corresponding to a given wavevector, the full dynamical matrix is obtained instead. The reason for obtaining the full dynamical matrix stems from

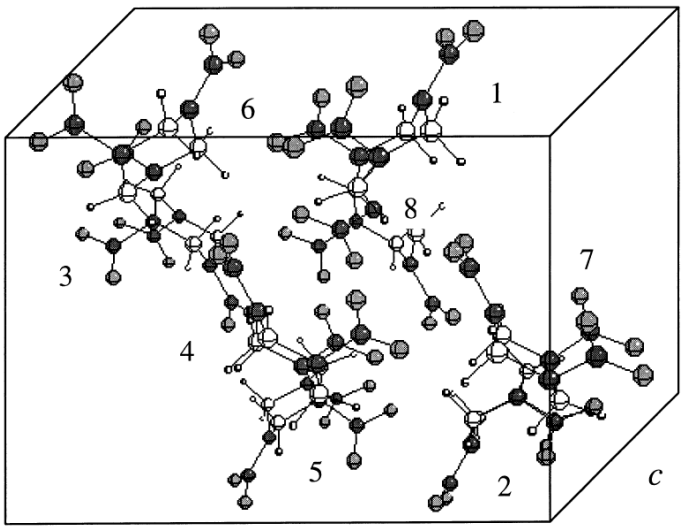

Figure 4.1: RDX unit cell (figure from [2])

the definition of the group velocity:

$$\boldsymbol{v}_g = \nabla_{\boldsymbol{k}}\omega \qquad . \tag{4.1}$$

The group velocity may be numerically evaluated from through a central differencing scheme. However, this process may result in errors in regions of the Brillouin zone where frequency values of different branches intersect. Degeneracies in the frequencies may occur at points or lines within the Brillouin zone and are an inherent feature of the point operation symmetry of the lattice [72].

In regions where degeneracy occurs, it may become difficult to discern which frequency values corresponds to which phonon state $(\boldsymbol{k}, \lambda)$. Inability to discern which branch a frequency corresponds to poses challenges to the central differencing approach for obtaining the group velocity. This obstacle may be circumvented by

instead using an alternative definition of the group velocity, which involves differentiating the entire dynamical matrix. In doing so the issue of assigning frequencies to the appropriate branches is circumvented as all the branch information is implicitly handled by numerically differentiating a single dynamical matrix as opposed to differentiating multiple frequencies. The alternative definition for group velocity is:

$$\frac{\partial \omega}{k_\alpha} = \frac{1}{2\omega} \boldsymbol{e}^\dagger \frac{\partial \boldsymbol{D}}{\partial k_\alpha} \boldsymbol{e} \qquad , \tag{4.2}$$

where k_α is the α-th component of the wavevector under consideration and $\boldsymbol{e}$ and $\boldsymbol{e}^\dagger$ are the dynamical matrix eigenvector and its associated adjoint.

The derivation for this expression is as follows. Consider the eigensystem of the dynamical matrix,

$$\boldsymbol{D}\boldsymbol{e} - \omega^2 \boldsymbol{e} = \boldsymbol{0} \qquad , \tag{4.3}$$

and its Hermitian adjoint

$$\boldsymbol{e}^\dagger \boldsymbol{D} - \boldsymbol{e}^\dagger \omega^2 = \boldsymbol{0} \qquad , \tag{4.4}$$

where the hermiticity of the dynamical matrix has been invoked. Taking the derivative of Eq. 4.3 yields the expression:

$$\frac{\partial \boldsymbol{D}}{\partial k_\alpha}\boldsymbol{e} + \boldsymbol{D}\frac{\partial \boldsymbol{e}}{\partial k_\alpha} - 2\omega \frac{\partial \omega}{\partial k_\alpha}\boldsymbol{e} - \omega^2 \frac{\partial \boldsymbol{e}}{\partial k_\alpha} = \boldsymbol{0} \qquad . \tag{4.5}$$

Rearranging this expression and left multiplying by $\boldsymbol{e}^\dagger$ yields:

$$\boldsymbol{e}^{\dagger}\frac{\partial \boldsymbol{D}}{\partial k_{\alpha}}\boldsymbol{e} - 2\omega\frac{\partial \omega}{\partial k_{\alpha}}\boldsymbol{e}^{\dagger}\boldsymbol{e} + \left(\boldsymbol{e}^{\dagger}\boldsymbol{D} - \boldsymbol{e}^{\dagger}\omega^{2}\right)\frac{\partial \boldsymbol{e}}{\partial k_{\alpha}} = \boldsymbol{0} \quad . \tag{4.6}$$

Utilizing the orthonormality of eigenvectors of the dynamical matrix as well as Eq. 4.4 reduces our expression to:

$$\boldsymbol{e}^{\dagger}\frac{\partial \boldsymbol{D}}{\partial k_{\alpha}}\boldsymbol{e} - 2\omega\frac{\partial \omega}{\partial k_{\alpha}} = \boldsymbol{0} \quad . \tag{4.7}$$

Rearrangement of this expression yields Eq. 4.2. The benefit of this method is that the group velocity and frequency for each branch of a given wavevector has no ambiguity.

Therefore, to perform a simulation, the allowed wavevectors, $\boldsymbol{k}$, are first determined from the system geometry. Next, for each wavevector the dynamical matrix is determined via GULP, and in addition six other dynamical matrices are determined at the wavevectors $\{k_x \pm dk, k_y \pm dk, k_z \pm dk\}$ and the central differencing is performed. The eigensystem, for each allowed wavevector, is then solved yielding the phonon frequencies and eigenvectors. Finally the frequencies and eigenvectors are used to evaluate Eq. 4.2, where by virtue of the method each phonon state $(\boldsymbol{k}, \lambda)$ maps to a unique frequency, eigenvector, group velocity triplet. The only remaining phonon input required is the relaxation time.

4.1.2 Relaxation Times

The right hand side collisional term of the phonon Boltzmann transport equation represents phonon-phonon, phonon-electron, phonon-impurity, and phonon-

boundary scattering. For a pristine infinite semiconducting crystal only phonon-phonon interactions occur, as these arise naturally from the anharmonicity of the interatomic potential. The complete mathematical description of three phonon interactions was first derived by Peierls [55], where the time rate of change of the occupation, N, of the phonon mode $(\boldsymbol{k}, \lambda)$ due to three phonon interactions is given by:

$$\begin{aligned}\left(\frac{\partial N(\boldsymbol{k},\lambda)}{\partial t}\right)_{collision} = \\ \frac{\hbar}{32\pi^2\rho}\int d^3\boldsymbol{k}'\Bigg[\sum_{\lambda'\lambda''}|b(\boldsymbol{k},\lambda;\boldsymbol{k}',\lambda';\boldsymbol{k}'',\lambda'')|^2\times\omega\omega'\omega''\delta(\omega+\omega'-\omega'')\times \\ (N_0+1)(N_0'+1)N_0''(g''-g-g')+ \\ \frac{1}{2}\sum_{\lambda'\lambda''}|b(\boldsymbol{k},\lambda;\boldsymbol{k}',\lambda';\boldsymbol{k}'',\lambda'')|^2\,\omega\omega'\omega''\delta(\omega-\omega'-\omega'') \\ (N_0+1)N_0'N_0''(g'+g''-g)\Bigg] \quad ,\end{aligned} \tag{4.8}$$

here $\hbar$ is Planck's constant divided by 2π, ρ is the material density, the integration ranges over the entire first Brillouin zone where the sum and integration only includes phonon modes that satisfy pseudo-momentum conservation as well as energy conservation, i.e.

$$\begin{aligned}\boldsymbol{k}\pm\boldsymbol{k}' =& \boldsymbol{k}+\boldsymbol{G} \\ \omega_\lambda(\boldsymbol{k})\pm\omega_{\lambda'}(\boldsymbol{k}') =& \omega_{\lambda''}(\boldsymbol{k}'') \quad ,\end{aligned} \tag{4.9}$$

,where $\boldsymbol{G}$ is any reciprocal lattice vector. Additionally, N_0 is the equilibrium population of a phonon mode as given by Bose-Einstein statistics, $|b(\boldsymbol{k}, \lambda; \boldsymbol{k}', \lambda'; \boldsymbol{k}'', \lambda'')|$ represents the strength of the three phonon process (i.e. the *coupling* between modes), and finally g represents how strongly the phonon mode occupation deviates from the equilibrium value $N_0(\boldsymbol{k}, \lambda)$. The physical basis of this expression, within the particle description, may be understood as follows. The integration ranges over the frequency surface within the first Brillouin zone defined through the delta functions in Eq. 4.8. Points on the constant frequency surface where the pseudo-momentum conservation rules are satisfied correspond to either a creation or an annihilation event for mode $(\boldsymbol{k}, \lambda)$. The first term in the summation of Eq. 4.8 corresponds to a creation event, while the second corresponds to an annihilation event (the factor of $1/2$ accounts for double counting physically indistinguishable processes). See Fig. 4.2 for an illustration of the two types of three phonon scattering. By integrating over the whole Brillouin zone in Eq. 4.8 and summing over all branches, the effect of all possible annihilation and creation processes, on the occupancy of mode $(\boldsymbol{k}, \lambda)$, are accounted for. Further information on phonon-phonon interactions may be found in [55].

The Boltzmann transport equation has been solved exactly by retaining this full scattering term [73–76], however this method is restricted to one-dimensional systems under the assumption of small temperature deviation. Even with these simplifications implementation of the iterative solution procedure proves to be computationally demanding as it requires a double integral over a sufficiently fine grid of

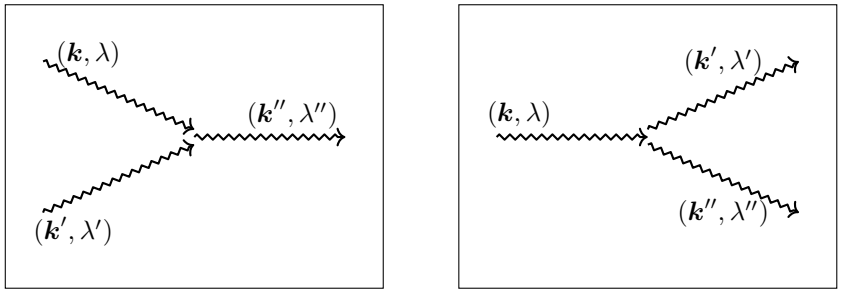

(a) (b)

Figure 4.2: Three phonon interactions within the particle viewpoints, annihilation (a) or creation (b) events

wavevectors within the first Brillouin Zone [77]. Therefore, Eq. 4.8 is often replaced with the relaxation time approximation:

$$\left(\frac{\partial N(\boldsymbol{k},\lambda)}{\partial t}\right)_{collision} = \frac{N_0(\boldsymbol{k},\lambda) - N(\boldsymbol{k},\lambda)}{\tau(\boldsymbol{k},\lambda)} \quad . \tag{4.10}$$

The relaxation time τ represents the average time a phonon travels before colliding with a boundary, impurity, or other energy carriers. These collisions serve to relax the phonon mode occupation back to equilibrium Bose-Einstein statistics, $N_0(\boldsymbol{k}, \lambda)$ A wide range of relaxation time values appear in the literature. Early expressions for τ were derived from theory using simplifications such as the assumption of low temperature [78, 79], or were fit to experimental data for bulk crystals [80]. However, advances in *ab-initio* calculations have allowed for phonon relaxation times to be fitted to results from first principles DFPT calculations [34]. These relaxation times have been found to accurately predict the thermal conductivity of common semiconductor materials silicon and germanium. Furthermore,

these relaxation times have been been previously used in computational studies of thin silicon films and therefore are applicable to length scales of interest within this work. Thus for studies of silicon the following form of the relaxation times will be used:

$$\tau_j^{(N)}(\omega, T) = \frac{1}{A_j^{(N)}\omega^2 T\left[1 - \exp(-\frac{3T}{\Theta_D})\right]} \qquad j = TA, LA \tag{4.11}$$
$$\tau_j^{(U)}(\omega, T) = \frac{1}{A_j^{(U)}\omega^4 T\left[1 - \exp(-\frac{3T}{\Theta_D})\right]}$$

$A_{TA}^{(N)}$ $(\text{meV}^2\text{K s})^{-1}$	$A_{LA}^{(N)}$ $(\text{meV}^2\text{K s})^{-1}$	$A_{TA}^{(U)}$ $(\text{meV}^2\text{K s})^{-1}$	$A_{LA}^{(U)}$ $(\text{meV}^2\text{K s})^{-1}$
253322	163921	2012	507

Table 4.1: Constants for evaluation of silicon phonon relaxation times, all values obtained from [34]

4.2 Discretization

Obtaining the the energy and temperature profiles of a nanoscale device requires the solution of the Boltzmann transport equation for every phonon state that exists within the material. The Boltzmann transport equation for a general wavevector and polarization $(\boldsymbol{k}, \lambda)$ under the relaxation time approximation is:

$$\frac{\partial N_{\boldsymbol{k},\lambda}}{\partial t} + \boldsymbol{v}_g(\boldsymbol{k},\lambda) \cdot \nabla N_{\boldsymbol{k},\lambda} = \frac{N^0_{\boldsymbol{k},\lambda} - N_{\boldsymbol{k},\lambda}}{\tau_{\boldsymbol{k},\lambda}} \quad . \tag{4.12}$$

This expression cannot, in general, be solved analytically and therefore must be discretized and solved using a numerical method. The numerical procedure used is the control volume method which has long been applied to heat transfer and fluid mechanics simulations [81]. The control volume method is straightforward to implement, and by its very nature ensures energy conservation regardless of the refinement level of the spatial grid [81]. The basic concept of the control volume method is to partition the solution domain into non-overlapping control volumes and integrate the differential equation of interest over each volume. Assuming the solution variable is constant over each volume yields a system of linear equations of size equal to the number of control volumes. This linear system is then solved to obtain the solution variables of interest.

Consider a finite domain in real space denoted by Ω. Associated with this domain is a discrete set of allowed vibrational modes which may exist within the material that constitutes Ω, a single mode is uniquely defined through a wavevector and branch index $(\boldsymbol{k},\lambda)$. The spatial domain may now be discretized into N_{CV} volume elements or control volumes, where the i^{th} generic control volume is denoted by $\Delta\Omega_i$. The domain with single control volume and the associated Brillouin zone are depicted in Fig. 4.3, although the figure shows a two dimensional rectangular domain and control volume the numerical discretization presented in this section is applicable to a general three dimensional domain with polyhedral control volumes.

Figure 4.3: Spatial domain Ω with control volume $\Delta\Omega_i$ and the associated Brillouin zone with discrete kpoints.

In this work steady state solution are desired, where the general form of the steady state Boltzmann transport equation within the relaxation time approximation for a phonon state $(\boldsymbol{k}, \lambda)$ is written as:

$$\boldsymbol{v}_g \cdot \nabla N_{\boldsymbol{k}}(\boldsymbol{r}) = \frac{1}{\tau_{\boldsymbol{k}}} \left[N^0_{\boldsymbol{k}}(\boldsymbol{r}) - N_{\boldsymbol{k}}(\boldsymbol{r}) \right] \qquad , \tag{4.13}$$

where the branch index λ is implied on every term. $\boldsymbol{v}_g$ represents the phonon group velocity, $\tau_{\boldsymbol{k}}$ is the relaxation time, $N^0_{\boldsymbol{k}}$ is the equilibrium occupation of the phonon state, and $N_{\boldsymbol{k}}$ is the unknown occupation of the phonon state. The occupation of a phonon state represent the number of energy quanta, or phonons, in that state. The equilibrium occupation is determined through Bose-Einstein statistics, which has the functional form:

$$N^0_{\boldsymbol{k}} = \left[e^{\frac{\hbar\omega_{\boldsymbol{k}}}{k_b T(\boldsymbol{r})}} - 1 \right]^{-1} \tag{4.14}$$

where k_b is the Boltzmann constant and T the temperature. Note that the equilibrium distribution is independent of wavevector and depends only on the phonon state frequency $\omega_{\boldsymbol{k}}$.

Next the Boltzmann transport equation is converted into its energy density form. The energy density of the phonon mode is given by $e_{\boldsymbol{k}} = (N_{\boldsymbol{k}} + \frac{1}{2})\hbar\omega_{\boldsymbol{k}}$, where within the particle description $N_{\boldsymbol{k}}$ describes the number of phonons in the spatial region $(\boldsymbol{r}, \boldsymbol{r}+d\boldsymbol{r})$, i.e. it is the phonon number density. The simulations in this work are for temperatures that are sufficiently large such that the zero point energy, $\frac{1}{2}\hbar\omega_{\boldsymbol{k}}$, may be neglected. Thus multiplying Eq. 4.13 by $\hbar\omega_{\boldsymbol{k}}$ yields the energy density form of the BTE:

$$\boldsymbol{v}_g \cdot \nabla e_{\boldsymbol{k}}(\boldsymbol{r}) = \frac{1}{\tau_{\boldsymbol{k}}} \left[e^0_{\boldsymbol{k}}(\boldsymbol{r}) - e_{\boldsymbol{k}}(\boldsymbol{r}) \right] \qquad . \tag{4.15}$$

Device simulations often incorporate the effect of electron-phonon interactions. When a transistor is turned on electrons are accelerated towards the drain, these high-energy electrons interact with the crystalline lattice transferring energy and creating phonons. This phonon creation, known as Joule heating, is modeled through a source term added to the RHS of Eq. 4.15:

$$\boldsymbol{v}_g \cdot \nabla e_{\boldsymbol{k}}(\boldsymbol{r}) = \frac{1}{\tau_{\boldsymbol{k}}} \left[e^0_{\boldsymbol{k}}(\boldsymbol{r}) - e_{\boldsymbol{k}}(\boldsymbol{r}) \right] + S_{\boldsymbol{k}} \qquad , \tag{4.16}$$

note that despite motivating the source term through the Joule heating analogy, it is a general term which models any process that generates phonons.

Eq. 4.16 is now integrated over a polyhedral control volume $\Delta\Omega_i$,

$$\int_{\Delta\Omega_i} \boldsymbol{v}_g \cdot \nabla e_{\boldsymbol{k}}(\boldsymbol{r}) d\boldsymbol{r} = \int_{\Delta\Omega_i} \frac{1}{\tau_{\boldsymbol{k}}} \left[e^0_{\boldsymbol{k}}(\boldsymbol{r}) - e_{\boldsymbol{k}}(\boldsymbol{r}) \right] d\boldsymbol{r} + \int_{\Delta\Omega_i} S_{\boldsymbol{k}} d\boldsymbol{r} \qquad . \tag{4.17}$$

In the control volume method it is assumed that the spatial discretization is sufficiently fine that the variation of $e_{\boldsymbol{k}}$ and $e^0_{\boldsymbol{k}}$ over a single control volume is very small. Therefore $e_{\boldsymbol{k}}$ and $e^0_{\boldsymbol{k}}$ are taken to be constant within each control volume,

$$\int_{\Delta\Omega_i} \boldsymbol{v}_g \cdot \nabla e_{\boldsymbol{k}}(\boldsymbol{r}) d\boldsymbol{r} = \frac{1}{\tau_{\boldsymbol{k}}} \left[e^0_{\boldsymbol{k},i}(\boldsymbol{r}) - e_{\boldsymbol{k},i}(\boldsymbol{r}) \right] \Delta\Omega_i + S_{\boldsymbol{k},i} \Delta\Omega_i \quad . \tag{4.18}$$

The LHS of Eq. 4.18 still requires discretization of the spatial operator.

Consider only the LHS of Eq. 4.18 and apply the Gauss divergence principle,

$$\int_{\Delta\Gamma_i} \boldsymbol{v}_g \cdot e_{\boldsymbol{k}}(\boldsymbol{r}) \hat{\boldsymbol{n}} \, dS \quad , \tag{4.19}$$

where now integration ranges over the surface of cell $\Delta\Omega_i$, denoted $\Delta\Gamma_i$, and $\hat{\boldsymbol{n}}$ is the outward facing normal. The cell boundary may be divided into facets, where over each facet $\hat{\boldsymbol{n}}$ and $e_{\boldsymbol{k}}$ is constant. Under this assumption Eq. 4.19 becomes

$$\sum_{m=1}^{\#\ of facets} A_m e_{\boldsymbol{k},m} \boldsymbol{v}_g \cdot \hat{\boldsymbol{n}}_m \quad , \tag{4.20}$$

where m is an arbitrary facet of the control volume surface, $\Delta\Gamma_i$, and A_m is the area of that facet. In order to resolve the value of $e_{\boldsymbol{k},m}$, the first order upwinding approximation is applied. The upwinding approximation states that the value of an advected quantity at a facet between two control volumes is that of the cell center of the upwind control volume, where the upwind direction is uniquely determined by $\boldsymbol{v}_g$. The upwinding approximation is represented visually for two dimensions in Fig. 4.4, and may be written mathematically for a general facet m as

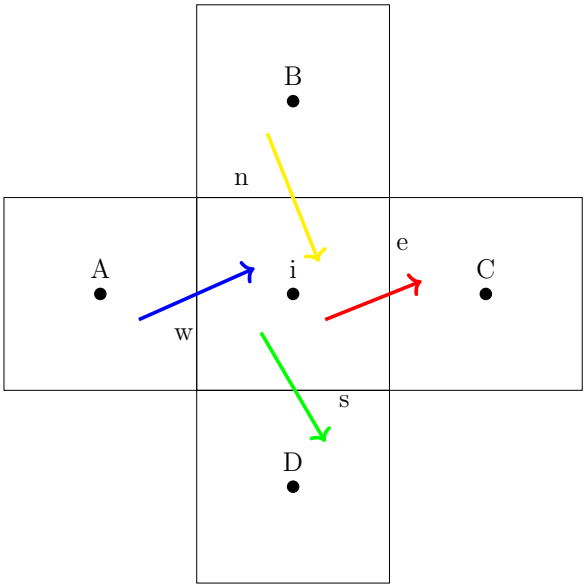

Figure 4.4: Examples of the upwind direction at all four facets of cell i for four different phonon propagation directions (red, yellow, blue, and green). At face e, the upwind direction corresponds to cell i. At face n, the upwind direction corresponds to cell B. At face w, the upwind direction corresponds to cell A. At face s, the upwind direction corresponds to cell i.

$$e_{\boldsymbol{k},m} = \frac{\max(\boldsymbol{v}_g \cdot \hat{\boldsymbol{n}}_m, 0)}{|\boldsymbol{v}_g \cdot \hat{\boldsymbol{n}}_m|} e_{\boldsymbol{k},i} + \frac{\max(-\boldsymbol{v}_g \cdot \hat{\boldsymbol{n}}_m, 0)}{|\boldsymbol{v}_g \cdot \hat{\boldsymbol{n}}_m|} e_{\boldsymbol{k},j} \quad , \tag{4.21}$$

here j refers to the control volume that shares facet m with control volume i.

Once the spatial operator has been discretized, Eqs. 4.18, 4.20, and 4.21 may be combined to yield

$$\begin{aligned} \sum_{m=1}^{\#\ offacets} A_m \left[\frac{\max(\boldsymbol{v}_g \cdot \hat{\boldsymbol{n}}_m, 0)}{|\boldsymbol{v}_g \cdot \hat{\boldsymbol{n}}_m|} e_{\boldsymbol{k},i} + \frac{\max(-\boldsymbol{v}_g \cdot \hat{\boldsymbol{n}}_m, 0)}{|\boldsymbol{v}_g \cdot \hat{\boldsymbol{n}}_m|} e_{\boldsymbol{k},j} \right] \boldsymbol{v}_g \cdot \hat{\boldsymbol{n}}_m \\ = \frac{1}{\tau_{\boldsymbol{k}}} \left[e^0_{\boldsymbol{k},i}(\boldsymbol{r}) - e_{\boldsymbol{k},i}(\boldsymbol{r}) \right] \Delta\Omega_i + S_{\boldsymbol{k},i} \Delta\Omega_i \quad . \end{aligned} \tag{4.22}$$

Eq. 4.22 represents a single linear equation within the system of equations corresponding to the phonon mode $(\boldsymbol{k}, \lambda)$. The final step in the discretization procedure

is to recast the linear system into matrix form, $K_{\boldsymbol{k}} u_{\boldsymbol{k}} = f_{\boldsymbol{k}}$. The elements of the matrix equations are:

$$(K_{\boldsymbol{k}})_{ij} = \begin{cases} \frac{1}{\tau_{\boldsymbol{k}}}\Delta\Omega_i + \sum_{m=1}^{\#\ offacets} A_m \frac{\max(\boldsymbol{v}_g \cdot \hat{\boldsymbol{n}}_m, 0)}{|\boldsymbol{v}_g \cdot \hat{\boldsymbol{n}}_m|} \boldsymbol{v}_g \cdot \hat{\boldsymbol{n}}_m & , \quad i = j \\ A_m \frac{\max(-\boldsymbol{v}_g \cdot \hat{\boldsymbol{n}}_m, 0)}{|\boldsymbol{v}_g \cdot \hat{\boldsymbol{n}}_m|} \boldsymbol{v}_g \cdot \hat{\boldsymbol{n}}_m & , \quad i \neq j \end{cases} \tag{4.23}$$

and

$$(f_{\boldsymbol{k}})_i = \frac{1}{\tau_{\boldsymbol{k}}}\Delta\Omega_i e^0_{\boldsymbol{k},i} + S_{\boldsymbol{k},i}\Delta\Omega_i \tag{4.24}$$

The linear system may be solved for the unknown cell centered phonon state energy densities, $e_{\boldsymbol{k},i}$. This process is then repeated for all allowed wavevectors and branches. Upon completion the total cell centered energy density may be computed via the summation,

$$e_i = \sum_{\boldsymbol{k}} e_{\boldsymbol{k},i} \quad . \tag{4.25}$$

Often in addition to obtaining the energy field the temperature is also sought, therefore once the energy field has been obtained the temperature field is determined through thermodynamic relations involving the specific heat.

4.2.1 Specific Heat

The volumetric specific heat is a thermodynamic quantity relating a materials energy to its temperature, and is defined as

$$C_V = \left(\frac{\partial U}{\partial T}\right)_V \quad , \tag{4.26}$$

where U is the internal energy density and the derivative is taking at constant volume. Using this definition the mode-wise volumetric specific heat may be defined as:

$$C_{V,\boldsymbol{k}} = \frac{\partial e_{\boldsymbol{k}}}{\partial T} \quad , \tag{4.27}$$

where it is assumed the material is stationary (once again the branch index is implied for all terms indexed by the wavevector $\boldsymbol{k}$). As temperature is a thermodynamic quantity defined only in equilibrium, the phonon mode energy density in Eq. 4.27 may be replaced by the equilibrium value, $e^0_{\boldsymbol{k}}$. Since the temperature dependence of the phonon mode energy at equilibrium is known to be $e^0_{\boldsymbol{k}} = \hbar\omega_{\boldsymbol{k}} \left[\exp(\frac{\hbar\omega_{\boldsymbol{k}}}{k_b T}) - 1\right]^{-1}$ the analytical form of the mode-wise specific heat,

$$C_{V,\boldsymbol{k}} = \frac{1}{V}\frac{(\hbar\omega_{\boldsymbol{k}})^2}{k_b T^2}\frac{e^{\frac{\hbar\omega_{\boldsymbol{k}}}{k_b T}}}{\left[e^{\frac{\hbar\omega_{\boldsymbol{k}}}{k_b T}} - 1\right]^2} \quad , \tag{4.28}$$

where V is the volume of the crystal. Equation 4.28 is a fully quantum mechanical expression in that it is a result of Bose-Einstein statistics and has been shown to be in excellent agreement with experimental data [82].

The total specific heat of the crystalline material is determined by summing all mode contributions,

$$C_V = \sum_{\boldsymbol{k}} C_{V,\boldsymbol{k}} \quad . \tag{4.29}$$

Equation 4.28 shows that the specific heat is a function of temperature, however for temperature ranges of interest in this work the specific heat will be assumed to take on a constant value at some reference temperature T_{ref}. The choice of T_{ref} is

not unique and for simplicity will be assumed to be that of the lowest prescribed temperature boundary condition (see Sec. 4.2.2), therefore $C_V(T) = C_V(T_{ref})$.

The assumption of constant specific heat allows for a simple relationship between energy and temperature to be established, specifically:

$$e = C_V \times (T - T_{ref}) \quad , \tag{4.30}$$

note that the energy density obtained in this manner corresponds to the difference between the system energy density at temperature T and the system energy density at temperature T_{ref}. Finally, it is important to recall that the energy-temperature relations obtained here are strictly only valid in an equilibrium system, where temperature is defined. However, it is customary in Boltzmann transport simulations to retain a pseudo-temperature, as defined by Eq. 4.30, even when the system is out of equilibrium and refer to this quantity as the temperature.

Finally, note that the force vector of the linear system given in Eq. 4.24 may be rewritten using the specific heat expression, and corresponding energy-temperature relations, defined in Eq's 4.30, 4.29, and 4.28. The updated force vector is,

$$(f_{\boldsymbol{k}})_i = \frac{1}{\tau_{\boldsymbol{k}}} \Delta\Omega_i C_{\boldsymbol{k}} (T_i - T_{ref}) + S_{\boldsymbol{k},i} \Delta\Omega_i \quad . \tag{4.31}$$

4.2.2 Boundary Conditions

Phonons, which are quantized lattice vibrations, are confined to a material and therefore scatter at material boundaries. Many works which appear in the literature

that solve the Boltzmann transport equation quantify this scattering through the inclusion of a boundary scattering relaxation time τ_b [28, 83–85]. However such a relaxation time is insufficient for the description of boundary scattering in materials with complex geometries and at material interfaces. Therefore, the work in this thesis implements a more fundamental approach whereby the surface conditions are applied as boundary conditions to the differential equation. In this manner, each facet of a control volume may be assigned different types of boundary scattering, boundary scattering can also vary for each allowed wavevector and branch. The three types of boundary conditions implemented in the Boltzmann transport equation solver are: Fourier interface condition, specular scattering, and diffuse scattering.

4.2.2.1 Fourier Interface Condition

Often a crystalline material may be grown on an amorphous substrate. One example of this is in a FinFET device where the silicon fin is deposited on silicon dioxide which is a disordered amorphous material. At such an interface, blackbody behavior may be assumed whereby phonons propagating out of the crystalline material and into the amorphous material are perfectly absorbed. Alternatively, phonon modes entering the crystalline material may be assumed to be occupied at equilibrium Bose-Einstein statistics. The mathematical expression for a Fourier interface condition is

$$e_{\boldsymbol{k},bound} = C_{V,\boldsymbol{k}} \left(T_{bound} - T_{ref} \right) \qquad ; \qquad \boldsymbol{v}_g(\boldsymbol{k}) \cdot \hat{\boldsymbol{n}} < 0 \tag{4.32}$$

where $\hat{\boldsymbol{n}}$ is the boundary outward facing normal and T_{bound} is the temperature at the control volume facet which intersects with the material interface. Note that this boundary condition allows for a non-zero net flux through the boundary.

4.2.2.2 Specular Scattering Condition

Exposed material boundaries must reflect all phonons into the bulk of the material. If at the atomic level the surface is perfectly ordered, phonons are assumed to undergo specular reflection, depicted in Fig. 4.5. Mathematically, specular reflection is expressed as:

$$\begin{aligned} e_{\boldsymbol{k}',bound} &= e_{\boldsymbol{k},i} \\ \boldsymbol{v}_g(\boldsymbol{k}') &= \left[\frac{\boldsymbol{v}_g(\boldsymbol{k})}{|\boldsymbol{v}_g(\boldsymbol{k})|} - 2\left(\frac{\boldsymbol{v}_g(\boldsymbol{k})}{|\boldsymbol{v}_g(\boldsymbol{k})|}\cdot\hat{\boldsymbol{n}}\right)\hat{\boldsymbol{n}}\right]|\boldsymbol{v}_g(\boldsymbol{k})| \quad , \end{aligned} \tag{4.33}$$

here $e_{\boldsymbol{k}',bound}$ represents the energy density at the facet of control volume i that intersects with the material boundary, where $\boldsymbol{k}$ and $\boldsymbol{k}'$ satisfy the condition in Eq. 4.33. Note that specular reflection does not resist the component of energy flux that is tangential to the material boundary.

4.2.2.3 Diffuse Scattering Condition

Fabrication techniques for nanoscale devices often create disorder within the crystalline lattice near the device surface. This surface roughness is assumed to diffusely reflect phonons [64, 86]. This diffuse reflection process is depicted visually in Fig. 4.6. The mathematical expression for diffuse reflection is

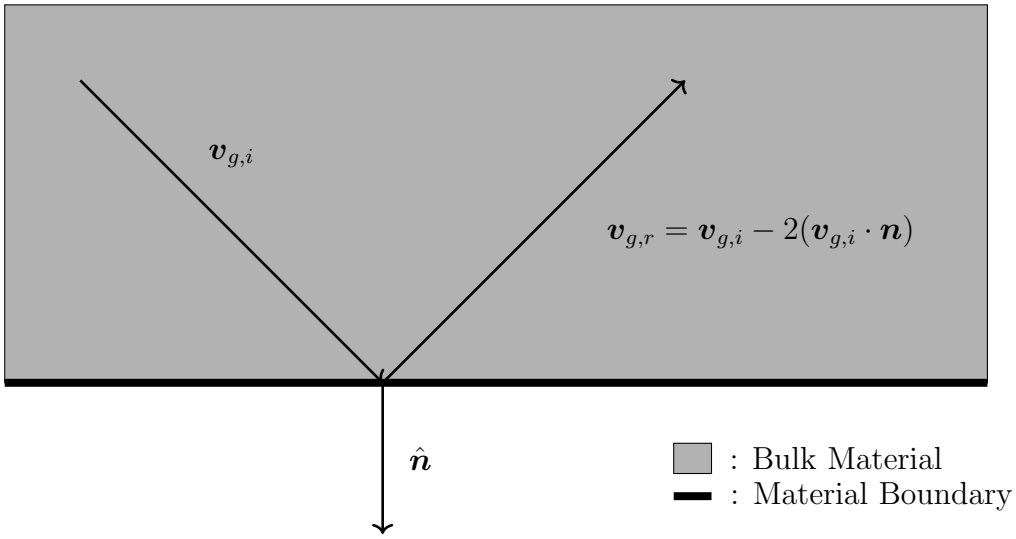

Figure 4.5: Phonon wavepacket undergoing specular reflection

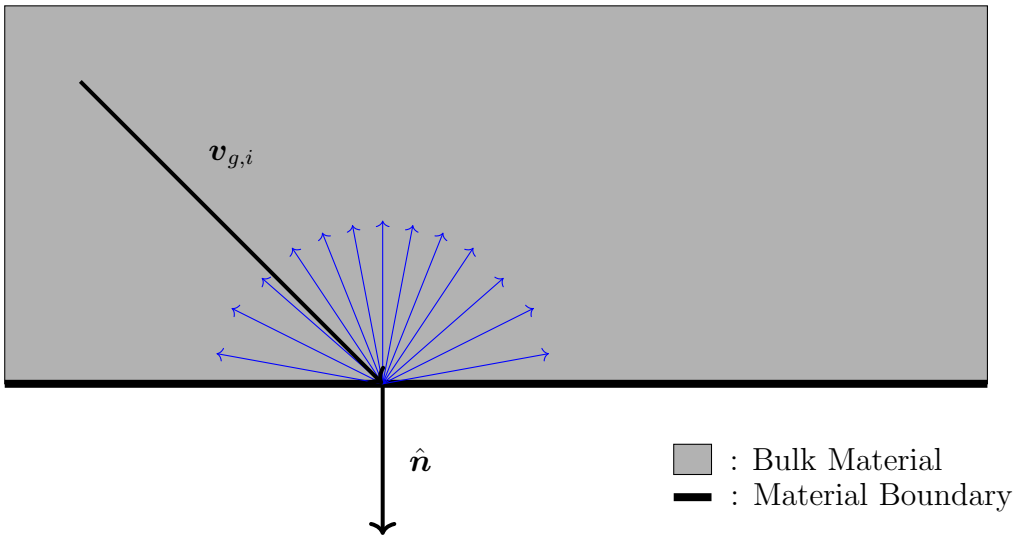

Figure 4.6: Phonon wavepacket undergoing diffuse reflection

$$
\begin{aligned}
e_{\boldsymbol{k},bound} =& \frac{1}{N} \sum_{\boldsymbol{k'}} e_{\boldsymbol{k'},i} \qquad ; \qquad \boldsymbol{v}_g(\boldsymbol{k'}) \cdot \hat{\boldsymbol{n}} > 0 \\
N =& \sum_{\boldsymbol{k'}} 1 \qquad \text{such that} \qquad \boldsymbol{v}_g(\boldsymbol{k'}) \cdot \hat{\boldsymbol{n}} < 0 \qquad ,
\end{aligned}
\tag{4.34}
$$

here $e_{\boldsymbol{k},bound}$ is the same expression as in Sec. 4.2.2.2. Diffuse scattering serves to redistribute energy incident on the boundary isotropically. Note that diffuse scattering *does* resist the component of energy flux tangential to the material boundary, thus diffuse scattering engenders thermal resistance.

All three types of boundary conditions amount to specifying the solution variable $e_{\boldsymbol{k},i}$ and are therefore essential or Dirichlet boundary conditions. Additionally, diffuse and specular boundary conditions are dependent upon the prevailing energy field and will therefore require iteration to obtain the appropriate steady state solution.

4.2.3 Computational Implementation

The final portion of this section covers the specifics of implementing the numerical algorithm detailed in this chapter into a Boltzmann transport equation code. A primary function of the code is to assemble and solve the linear system (terms given by Eqs. 4.23 and 4.24) for each allowed wavevector and branch. There exist a wide array of linear solver packages capable of solving the linear system. In choosing which linear solver package to implement three criterion were considered. First the linear solver needed to use condensed row storage (CRS) in order to avoid unnecessary floating point operations that grow costly for simulation of large systems. Additionally, the solver must be capable of inverting non-symmetric matrices, such as those that arise through application of the upwinding condition.

Finally the solver must be iterative in nature as direct methods would again prove too computationally expensive for large systems.

A generalized minimum residual (GMRES) iterative solver satisfying the three criterion was chosen as it provided a combination of speed and accuracy. Specifics of the solver implementation are as follows: the matrices are preconditioned through an incomplete LU preconditioning step, twenty Krylov subspaces were used in the inversion, and eight orders of magnitude reduction in the residual was enforced as a convergence criterion. The GMRES solver as well as the preconditioner routine are provided through the open source sparse matrix computation tool kit, SPARSKIT [87]. Implementation of this linear solver gave a 40 times speed up for a problem size of 1000 control volumes when compared to a direct solver which stores the entire linear system.

In Sec. 4.2.2 it was mentioned that due to the nature of specular and diffuse boundary conditions, the steady state solution must be computed iteratively. As a result a condition must be established to determine when the numerical solution $\{\boldsymbol{e}_i^{(k)} : i \in (1, \cdots, N_{CV})\}$ is sufficiently "close" to the exact solution $\{\boldsymbol{e}_i^{(exact)} : i \in (1, \cdots, N_{CV})\}$. Since the exact solution is in general not known, an alternative metric for determining convergence is required. This is done by taking the l^2 norm of the difference of the total system energy vector for consecutive iterations and requiring that it be sufficiently small with respect to the initial difference between iterations one and two. Mathematically this condition is stated as,

$$\|\boldsymbol{e}^{(k)} - \boldsymbol{e}^{(k-1)}\|_2 < \epsilon \, \|\boldsymbol{e}^{(2)} - \boldsymbol{e}^{(1)}\|_2 \tag{4.35}$$

where the l^2 norm has the traditional definition:

$$\|\boldsymbol{v}\|_2 = \left[\sum_i^N v_i^2\right]^{1/2} \qquad \boldsymbol{v} \in \mathbb{R}^N \qquad . \tag{4.36}$$

The value of ϵ is dependent on the desired accuracy of the final solution and is generally in the range 10^{-4} to 10^{-10}.

The algorithm detailed in this section involves solution of the Boltzmann transport equation for all allowable wavelengths and branches within the anisotropic first Brillouin Zone. While this approach is more rigorous than gray or isotropic assumptions, it becomes computationally expensive for large system sizes. In Sec. 3.5 it was shown that the finite size of a system restricts the allowed wavevectors within the Brillouin zone. In addition the number of these allowed wavevectors increases proportional to the volume of the crystal. Therefore within this algorithm, a linear system must be constructed and inverted for every allowed wavevector and all branches, which is a computationally demanding procedure. However, for a given iteration n, the assembly and solution of the linear system for a wavevector $\boldsymbol{k}$ is dependent only on prevailing values of the temperature and energy field, geometric quantities specific to the mesh, and phonon properties calculated a priori to the simulation. Thus the energy values for each wavevector may be solved for independently, allowing for parallelization of the algorithm.

The core concept of parallelization is that certain portions of a computer code may be shared between separate computing threads. These threads then perform operations simultaneously before returning control to a master thread which then

moves on to the next portion of the computer code, this process is depicted in Fig. 4.7. Parallelization is implemented within the Boltzmann transport equation

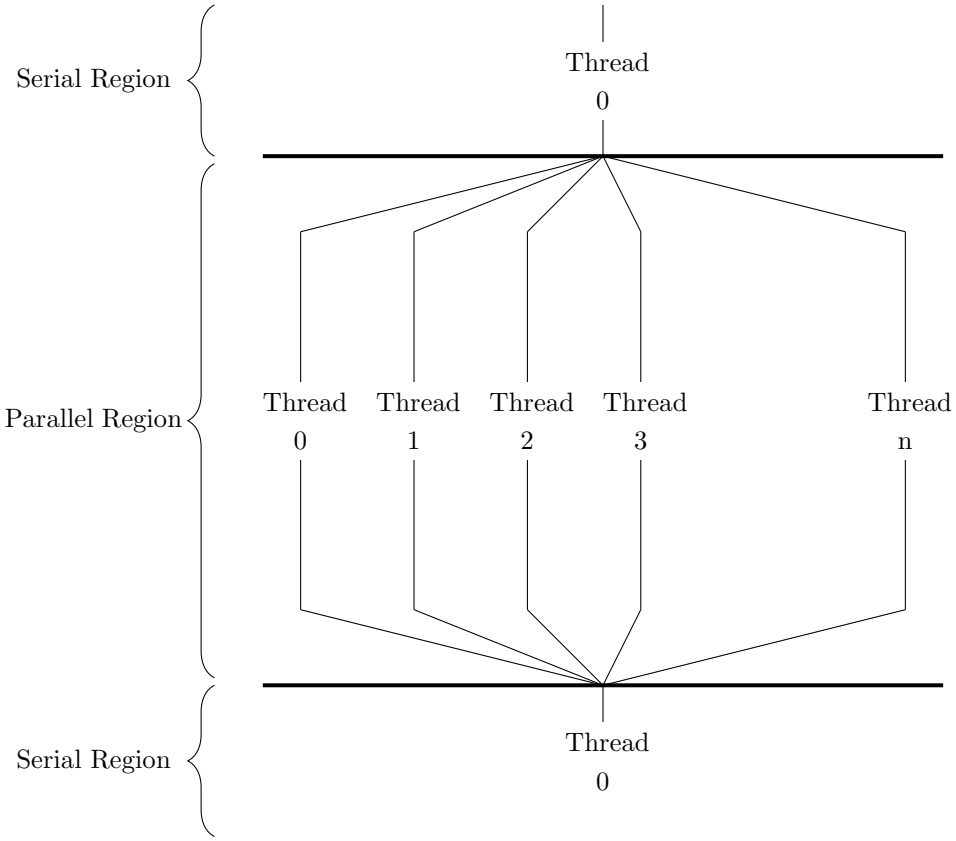

Figure 4.7: A computer code with serial and parallel regions. A master thread (Thread 0) controls program flow within a serial region. When a parallel region is encountered work is distributed to n threads. Upon completion of the parallel region control is returned to the master thread.

code via OpenMP directives. OpenMP is a computing tool comprised of compiler directives, library routines, and environment variables for use on shared-memory

machines [88]. By assembling and solving linear systems in parallel a 20 times speed up is achieved when using 40 threads with a system size of 1000 control volumes.

A flow chart detailing the numerical algorithm outlined in this chapter for solving the Boltzmann transport equation is given in Fig. 4.8. Thus determination of the temperature profile through the Boltzmann algorithm may now be summarized:

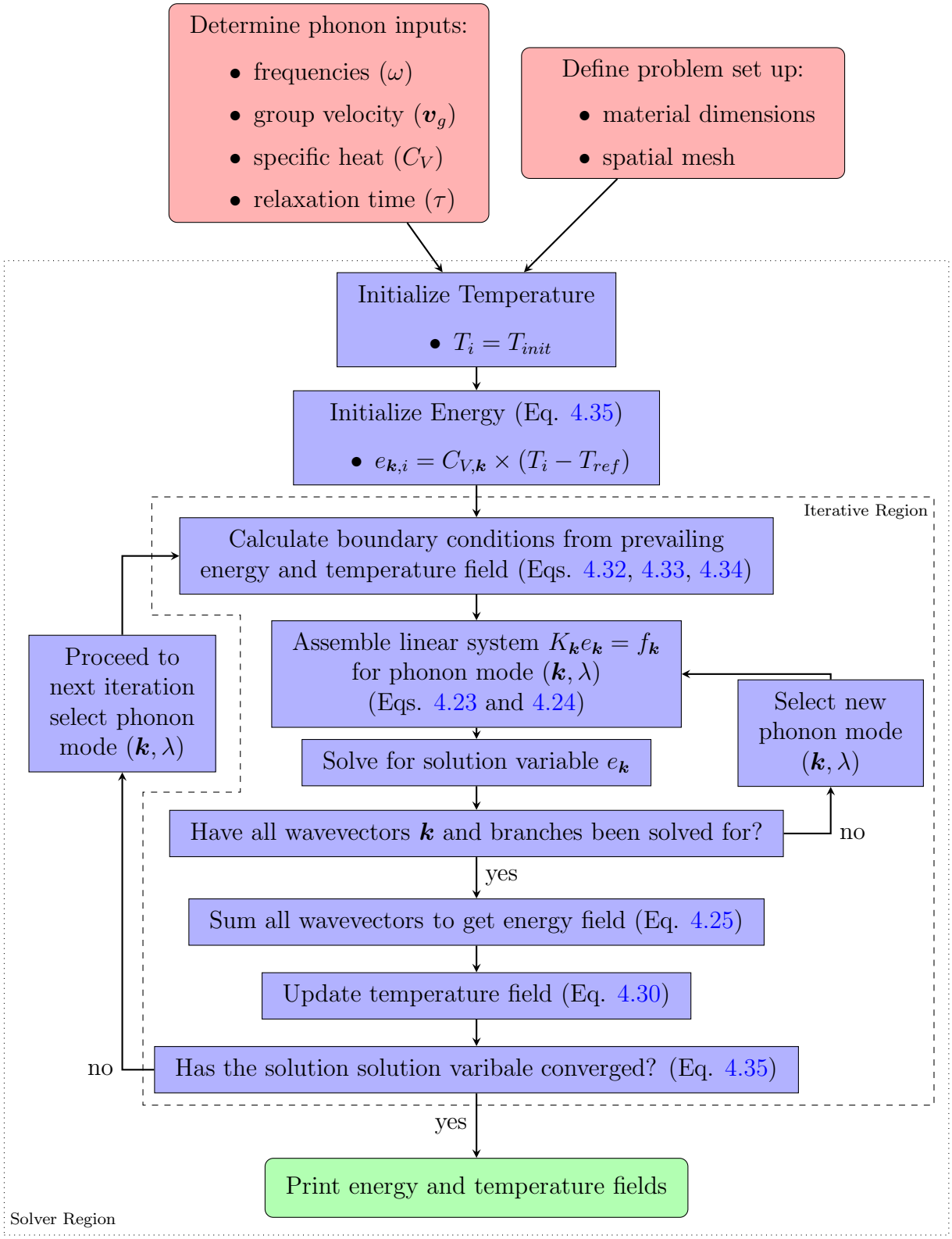

Figure 4.8: Control flow within Boltzmann transport code.

The fundamental difference between the algorithm presented in this chapter and those presented in the literature is the solution of the Boltzmann transport equation for all allowed wavevectors and branches within the anisotropic Brillouin Zone. By solving the Boltzmann transport equation for every allowed wavevectors and branches, anisotropy in the phonon transport may be captured in three dimensional nanoscale simulations.

In this section a method of solving the Boltzmann transport equations has been presented. The algorithm requires phonon properties as well as material dimensions as inputs and then solves the Boltzmann transport equation for all allowed wavevectors and all branches in a three-dimensional domain. It is this solution technique which accounts for all vibrational modes, and thus all energy carriers, that leads to a more fundamental model than what has previously been presented in the literature. This capability coupled with the multi-dimensionality of the numerical procedure generates a Boltzmann transport code capable of capturing the wide array of phonon physics that occur within a nanoscale device. In the next section the code's capabilities are demonstrated. First a simulation of semi-ballistic transport is performed and results obtained from the BTE code are compared to the semi-analytical solutions to verify the mathematical accuracy of the code. Next a study is performed to compare BTE solutions obtained under the isotropic solution to BTE solutions which account for full Brillouin zone anisotropy. Finally a FinFET device parameter study is performed to showcase the three-dimensional capability of the solver.

Chapter 5: Simulations and Results

5.1 Semi-Ballistic Transport

The Boltzmann transport equation is capable of accurate thermal modeling in regimes where phonon transport is dominated by boundary scattering, such as on the nanoscale. Accurate thermal modeling at the nanoscale requires capturing transport from the ballistic regime, where phonons propagate without scattering with other carriers, to the diffusive regime, where phonon-phonon scattering dominates, this range of transport is referred to as semi-ballistic transport. Methods such the Fourier equation of heat transfer assume that transport is completely diffusive and are therefore only valid within the diffusive regime. Thus a simulation of semi-ballistic transport may serve as a verification problem, testing the capability of the BTE code to accurately model transport spanning diffusive to ballistic regimes. Semi-analytical solutions of semi-ballistic transport are available within the radiative transport literature, one such example is the plane-parallel problem. The plane-parallel problem determines the radiation intensity field in a one dimensional domain with absorbing and emitting gray media. Solutions to such a problem have long been studied in the radiation transport literature [89–91]. The physics of radiative transport are very similar to phonon transport, where instead of quantized

lattice vibrations, quantized electromagnetic waves carry energy. In this section, the problem set up for the plane-parallel problem is detailed, the analytical expression for the exact solution is given along with the solution method, finally the results obtained from the Boltzmann transport equation solver are verified against the exact solution.

5.1.1 Verification Problem Set-Up

The physical setup of the plane-parallel problem is depicted in Fig. 5.1, note that the wall temperature slip is characteristic of semi-ballistic transport, where the temperature slip, ΔT, becomes zero in the diffuse transport limit. The governing differential equation for the radiative intensity field in such a problem may be written as [90]:

$$\begin{aligned} &\hat{\boldsymbol{s}} \cdot \nabla I = \beta \left(I_b - I \right) \quad , \quad I = I(\boldsymbol{r}, \hat{\boldsymbol{s}}) \\ &\begin{cases} I(0, \hat{\boldsymbol{s}}) = \quad I_b(T_1) \quad ; \quad \hat{\boldsymbol{s}} \cdot \hat{\boldsymbol{x}} > 0 \\ I(\tau_L, \hat{\boldsymbol{s}}) = \quad I_b(T_2) \quad ; \quad \hat{\boldsymbol{s}} \cdot \hat{\boldsymbol{x}} < 0 \end{cases} \end{aligned} \tag{5.1}$$

where $\hat{\boldsymbol{s}}$ represents the propagation direction, I the radiative intensity, and I_b the blackbody equilibrium intensity. The quantity τ_L is the optical thickness of the problem and is a measure of how strongly the radiative field interacts with the medium. The analogous quantity, to τ_L in phonon physics is the Knudsen number (Kn) which is defined as $\mathrm{Kn} = {}^{\Lambda}/_{L}$, where Λ is the mean free path (MFP) and L is the length of the domain. The MFP for a given wavevector $\boldsymbol{k}$ is $\Lambda_{\boldsymbol{k}} = |\boldsymbol{v}_g(\boldsymbol{k})|\tau_{\boldsymbol{k}}$, therefore each phonon mode will have its own Kn. For the remainder of of the

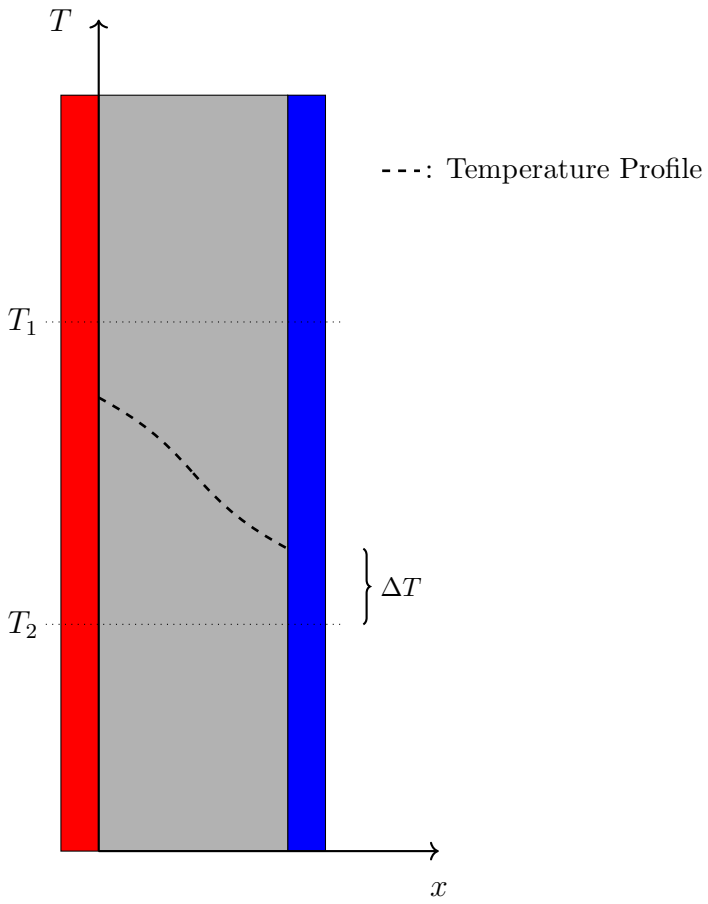

Figure 5.1: Temperature profile of a gray absorbing-emitting medium between two infinite parallel plates at temperature T_1 (red) and T_2 (blue). The temperature profile displays a temperature slip ΔT at the boundaries, a characteristic of semi-ballistic transport

section we will work with a single averaged phonon mode and thus Kn will have a single unique value. A Kn $\ll 1$ correspond to diffusive transport, while a Kn $\gg 1$ corresponds to the ballistic regime. It is important not to confuse the $\tau_{\boldsymbol{k}}$, the phonon relaxation time, with τ_L, the optical thickness for radiation transport.

The general solution for the non-dimensional temperature field in an absorbing-emitting gray medium is given by [90]:

$$\Phi_b(\tau) = \frac{1}{2}\left[E_2(\tau) + \int_0^{\tau_L} \Phi_b(\tau') E_1\left(|\tau - \tau'|\right) d\tau'\right] \tag{5.2}$$

$$\Phi_b(\tau) = \frac{T^4(\tau) - T_2^4}{T_1^4 - T_2^4} \quad ,$$

where the elliptic integral is defined as:

$$E_n(x) = \int_0^1 \mu^{n-2} e^{-x/\mu} d\mu \quad . \tag{5.3}$$

Integral Equations of this form may be solved through the *method of successive approximations*, where an initial guess of the desired function, Φ_b^k is substituted into the RHS of Eq. 5.2, the RHS of Eq. 5.2 is then computed yielding an updated, Φ_b^{k+1}, the resulting function is then used as the guess in the $k+1$ iteration. This procedure is outlined in Fig. 5.2. Using the method of successive approximations in conjunction with numerical quadrature, Φ_b was computed numerically for use in verification of the Boltzmann algorithm.

To compare to the numerical solution, the inputs to the BTE code must be altered to simulate gray photon transport. To that end a spherical Brillouin zone is created to simulate the isotropic continuum of propagation directions allowed for photons in radiative transport, see Fig. 5.3. As the the system being modeled is gray, i.e. frequency independent, all phonon properties are assumed constant

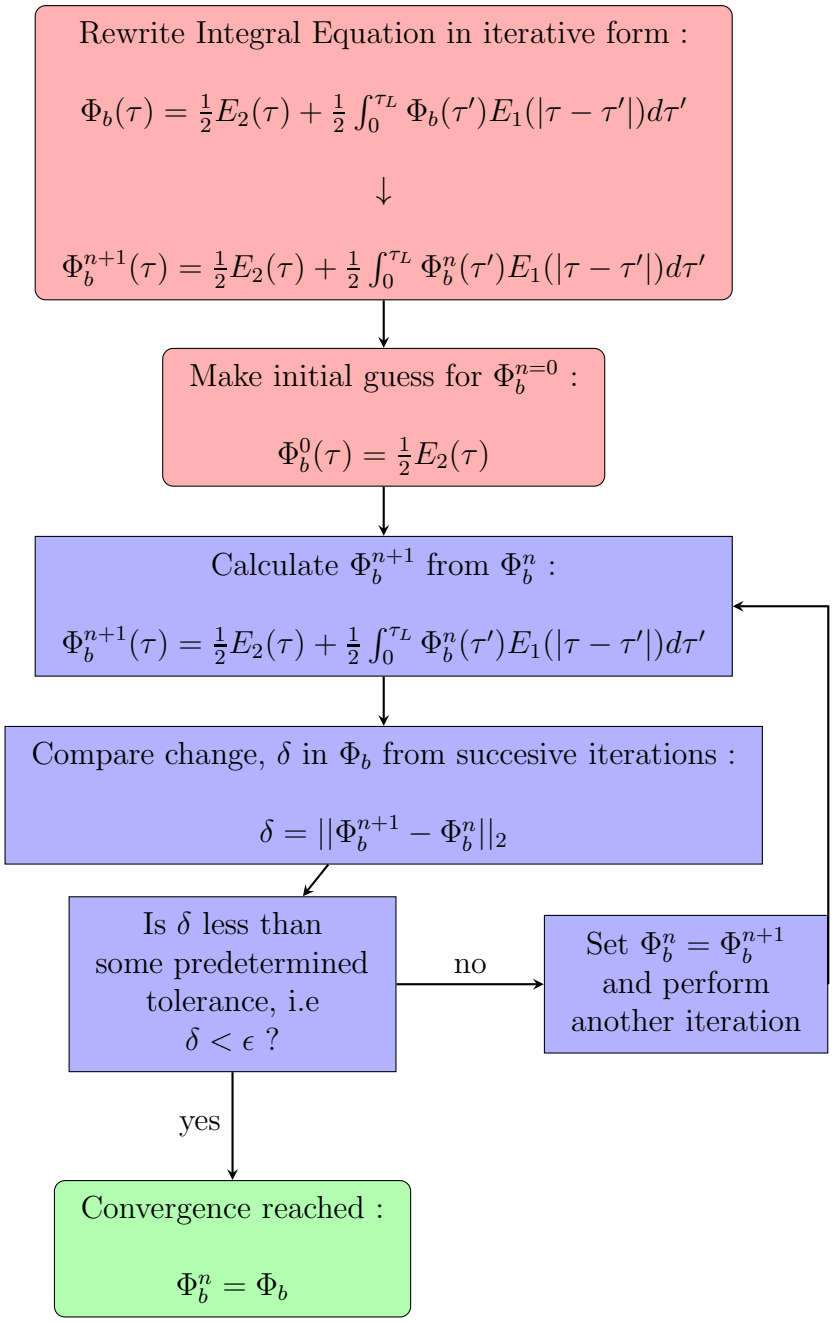

Figure 5.2: Method of successive approximations approach to solving the integral equation for the exact solution to the plane parallel problem

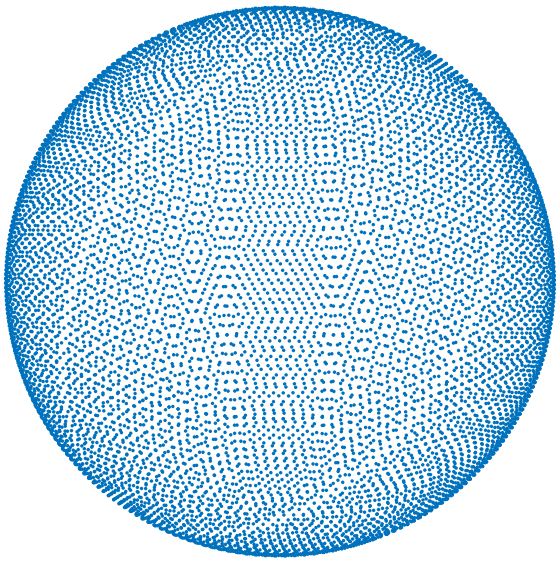

Figure 5.3: Schematic of a spherical Brillouin Zone.

except for the group velocity which was assumed to be constant in magnitude, and collinear with the wavevector. The gray phonon properties are given in Table 5.1. The simulation domain geometry replicates infinite parallel plates by specifying the y and z dimensions to be many orders of magnitude larger than the x dimensions. The plate at the $x = 0$ boundary was specified to be a Fourier interface condition with $T_1 = 301$ K and the high x boundary was specified to be a Fourier interface condition $T_2 = 300$ K. These conditions are analogous to the blackbody emitter-absorbers from the plane parallel problem. The distance between the plates was varied to investigate several Knudsen numbers (i.e. transport regimes). The transport regime is quantified by the Knudsen number where as the separation goes to zero (Kn $\gg 1$)

Specific Heat	$1.631 \times 10^6 \ \frac{\mathrm{J}}{\mathrm{m}^3 \cdot \mathrm{sec}}$
Group Velocity Magnitude	$6400 \ \frac{\mathrm{m}}{\mathrm{sec}}$
Relaxation Time	7.2×10^{-12} sec
Frequency	16.0 THz
Mean Free Path	4.608×10^{-8} m

Table 5.1: Gray phonon properties

transport becomes ballistic, and as the separation reaches several mean free paths (Kn < 1) the transport becomes more diffusive.

5.1.2 Verification Results

The results of the simulations for a range of Knudsen numbers are plotted in Figs. 5.4, 5.5, 5.6, and 5.7.

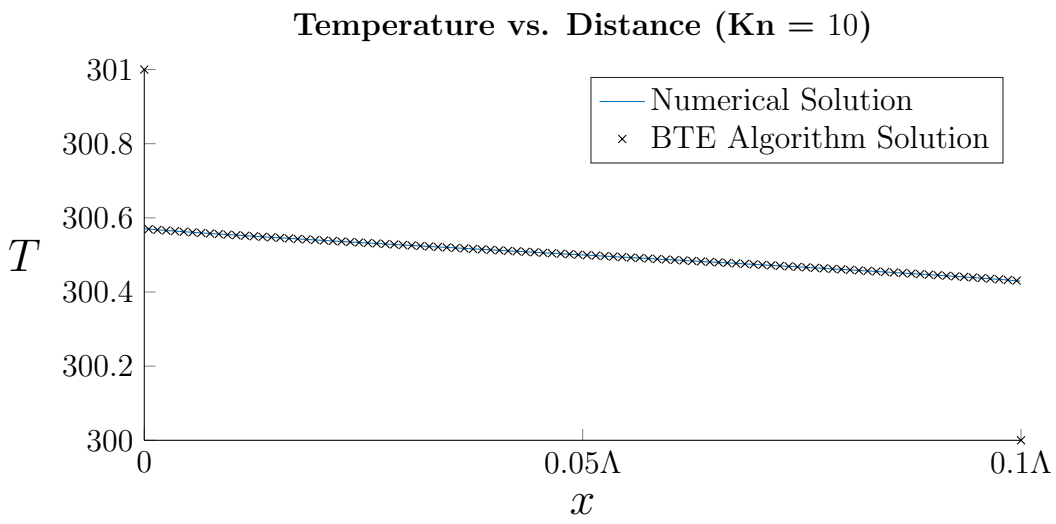

Figure 5.4: Temperature profile for domain length of $\frac{1}{10}$ Λ

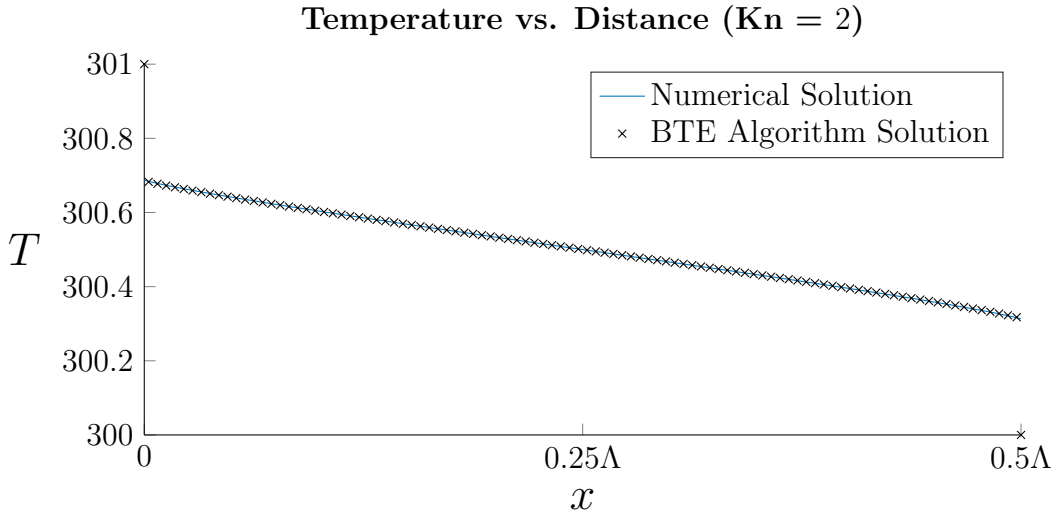

Figure 5.5: Temperature profile for domain length of $\frac{1}{2}$ Λ

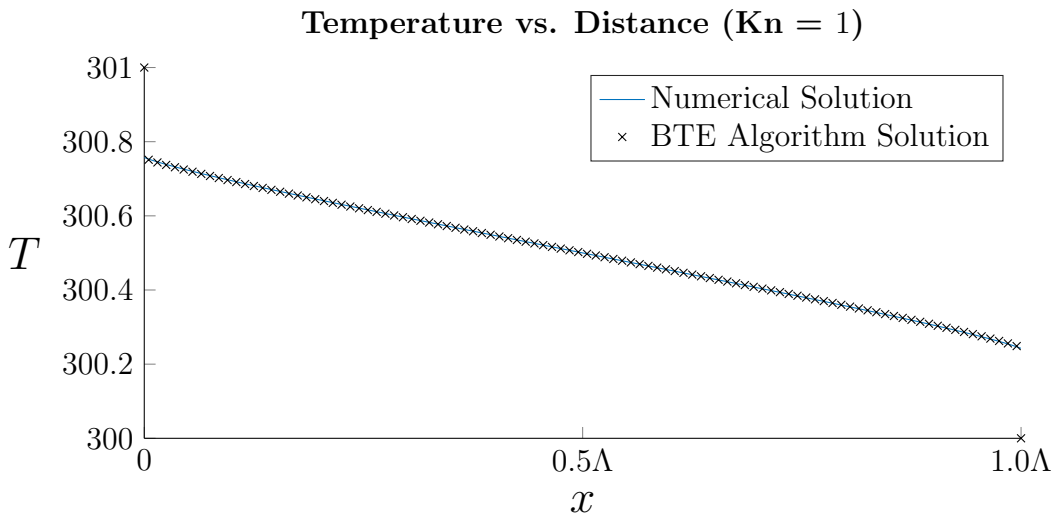

Figure 5.6: Temperature profile for domain length of 1 Λ

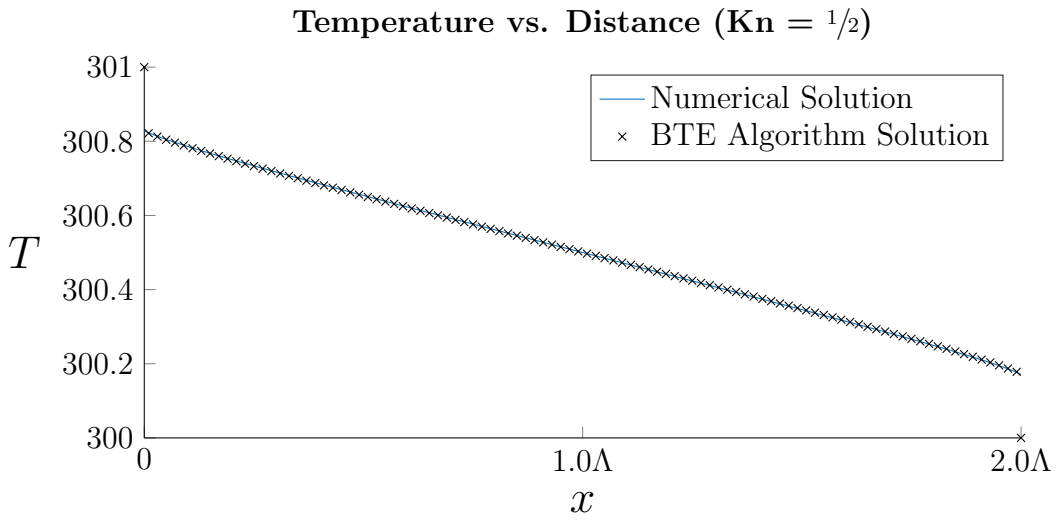

Figure 5.7: Temperature profile for domain length of 2 Λ

For all transport regimes the agreement is excellent between the numerical algorithm and the exact solution.

In addition to verifying the Boltzmann algorithm over a range of transport regimes, a mesh convergence study was performed to ensure that the algorithm converges to the exact solution as the mesh is refined. The results of the mesh convergence study, Fig. 5.8, give confidence that the algorithm has been implemented into the BTE code in a manner which reproduces exact numerical solutions.

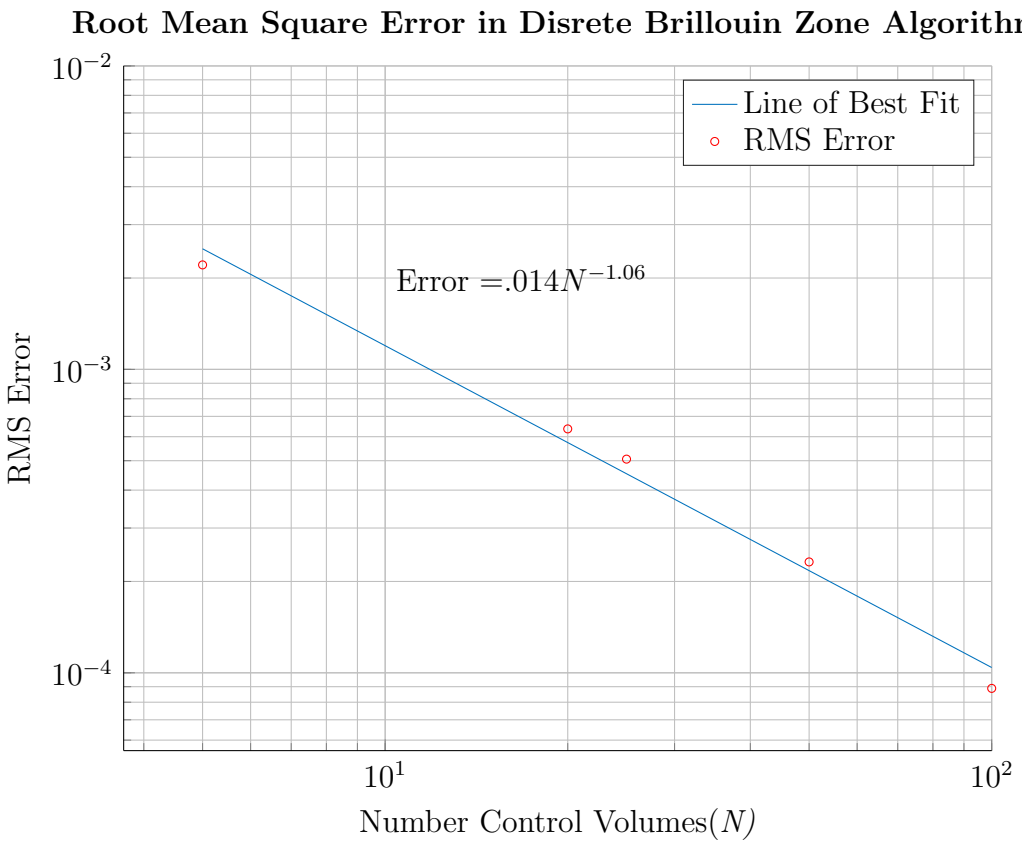

Figure 5.8: Logarithmic plot of root mean square (RMS) error between the Boltzmann algorithm and the exact numerical solution from [90]. Kn = 10
.

The BTE code results for the semi-ballistic transport simulations have been compared to semi-analytical solutions from radiation transport. The excellent agreement verifies that the BTE algorithm has been correctly implemented into a BTE code. In the following section the code is used to investigate the effect of Brillouin zone anisotropy. Finally the code is used to perform a parameter study of a nanoscale device.

5.2 Effect of Anisotropy

The vast majority of studies which use the Boltzmann transport equation to model nanoscale heat transport assume that high symmetry phonon properties prevail in all directions within the Brillouin zone. This assumption is equivalent to obtaining the dispersion curves of some material along a single high symmetry line, most often along the $\Gamma - X$ high symmetry line for the case of silicon(see Fig. 5.9), and assuming those frequency values are isotropic throughout a spherical Brillouin zone. Therefore, at any point in the Brillouin zone the frequency at that location is a function of $|\boldsymbol{k}|$ only, as the frequency is assumed spherically symmetric.

The consequence of these assumptions is twofold. First, the assumption effectively reduces the Brillouin zone shape to that of a sphere, as opposed to its true shape of a truncated octahedron for an FCC crystal (inset of Fig. 5.9). Within this sphere the frequencies, and all frequency dependent properties such as specific heat, are assumed to be distributed isotropically. Secondly, the group velocities become collinear with the wavevector and are therefore always directed radially outward.

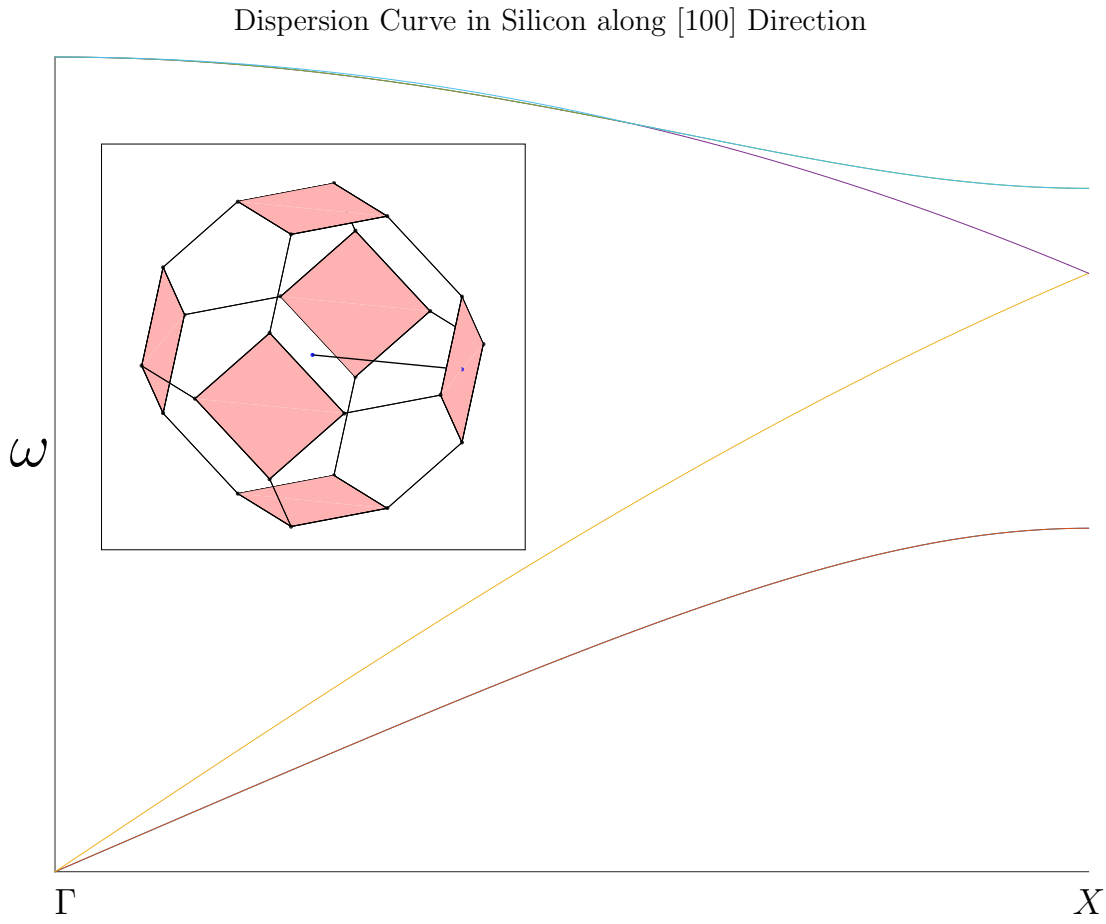

Figure 5.9: Vibrational frequencies in silicon along the high symmetry line $\Gamma - X$ corresponding to the [100] direction. The inset depicts the $\Gamma - X$ line (thick black line connecting the blue dots) within the first Brillouin zone of silicon

The true behavior of phonons within the anisotropic Brillouin zone is in fact-more complex. Consider the constant frequency contours of various branches within the $k_z = 0$ plane of the true anisotropic Brillouin zone given in Fig. 5.10. If the the Brillouin zone plane were isotropic these contours should be circular. However, only in certain regions can the contours be approximated as circles. The top row of Fig. 5.10 corresponds to the acoustic modes which are believed to dominate heat transport. The longitudinal acoustic mode (top right) is roughly circular near the Brillouin zone plane center, however the contours deviate strongly away from

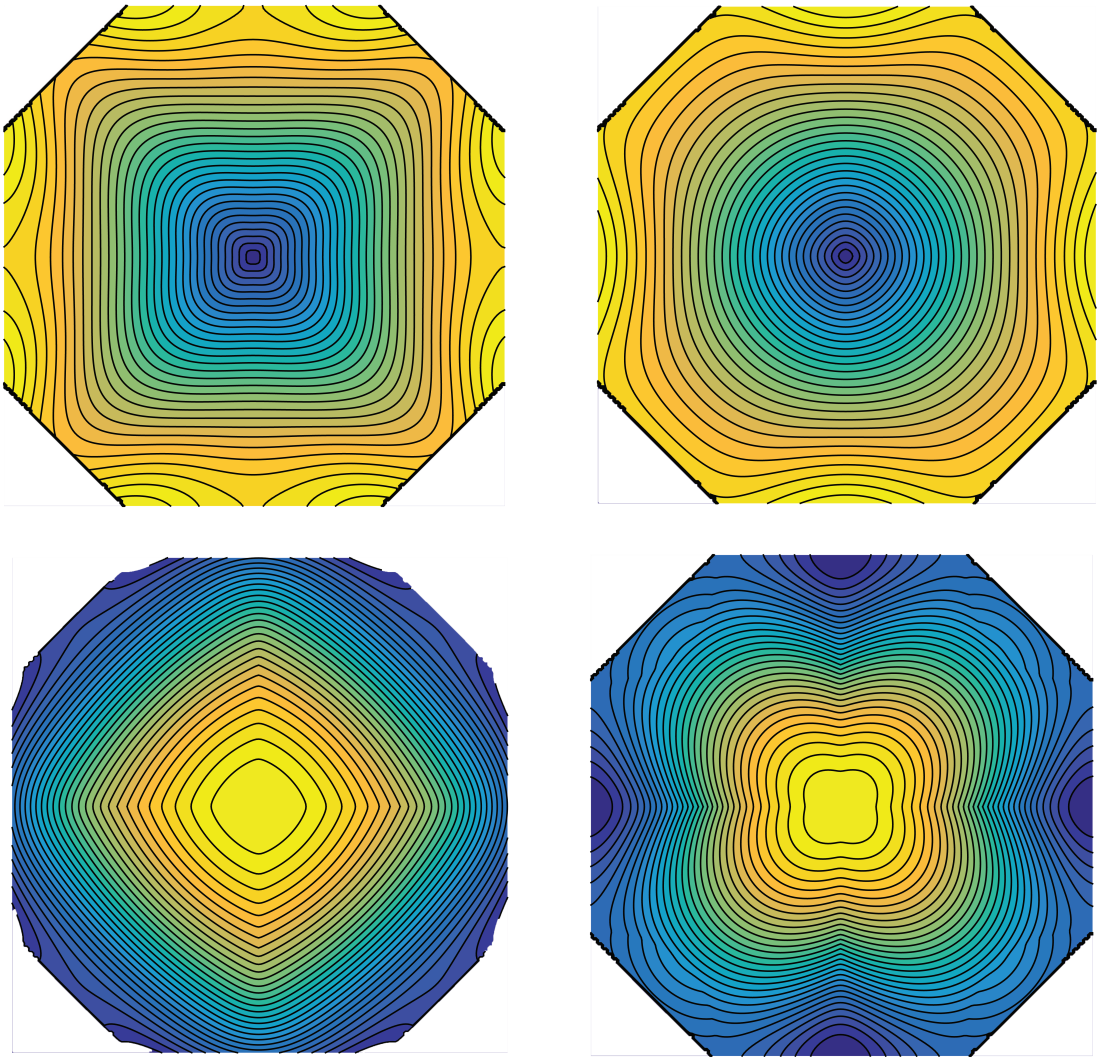

Figure 5.10: Frequency contours within the $k_z = 0$ first Brillouin zone for the first transverse acoustic branch (top left), the longitudinal acoustic branch (top right), the first transverse optical branch (bottom left), and the longitudinal optical branch (bottom right).

circular near the Brillouin zone edge, becoming more square-like. The transverse acoustic mode (top left) remains roughly square throughout the Brillouin zone plane suggesting that the assumption of an isotropic Brillouin zone could lead to errors in the phonon properties supplied to the Boltzmann transport equation. To verify whether frequency values are truly anisotropic in three dimensions a fine grid of wavevectors was created and the frequency values were determined via molecular

dynamics. The resulting frequency space was then discretized and all wavevectors corresponding to a frequency falling within a certain interval of frequency space were plotted. It was found that the constant frequency surface of the transverse acoustic mode is in fact a cube in three dimensions, see Fig. 5.11, further disproving the isotropic assumption.

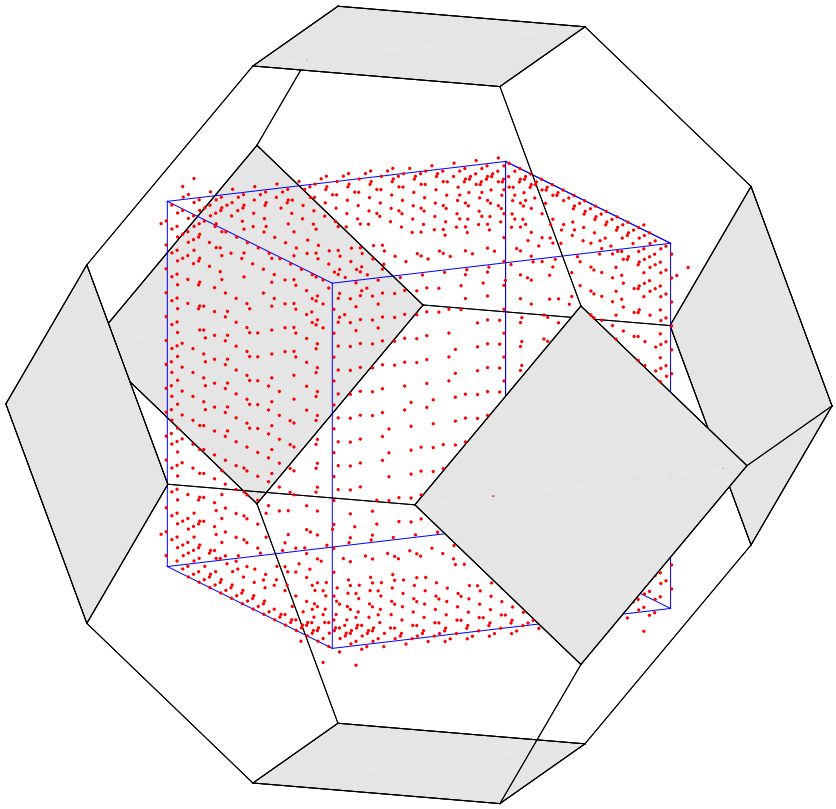

Figure 5.11: Constant frequency wavevectors of the transverse acoustic branch. The blue edges of the constant frequency square are visual guides

.

The anisotropy of frequencies within the Brillouin zone affects the phonon group velocities. In the isotropic assumption the group velocities, defined as $\boldsymbol{v}_g = \nabla_{\boldsymbol{k}}\,\omega$, are directed radially away from the Brillouin zone origin. However, it is shown in Fig. 5.12 that this simplification is not realistic. Figure 5.12 shows that away from the Brillouin zone center, frequencies become more anisotropic and the direction of phonon propagation deviates strongly from the radial direction. Additionally, for the transverse acoustic mode the majority of phonon propagation directions align along the x, y, z Cartesian directions, while a smaller percentage lie along the diagonal directions. Since the phonon group velocity is the speed and direction in which energy of a given mode is carried, therefore advection of a phonon mode will strongly depend on group velocity. Therefore, Fig. 5.12 would suggest that advection will be largest along the x and y directions and reach a minimal value along the diagonal directions.

The anisotropic distribution of frequency in the Brillouin zone, along with phonon mode group velocities which deviate from the radially outward direction, indicate that temperature profiles obtained using the isotropic assumption may incur some error. A two dimensional simulation of a thin silicon film with a heat source was performed to study what effect, if any, anisotropy has on phonon transport and the resulting temperature profile. The dimensions of the heat transport problem are given in Fig. 5.13, in addition the thickness of the film was set to 17.4 nanometers with diffusely reflecting boundary conditions.

Note that in general, different forms of the Boltzmann transport equation (i.e. gray, frequency dependent with isotropic assumption, or fully anisotropic)

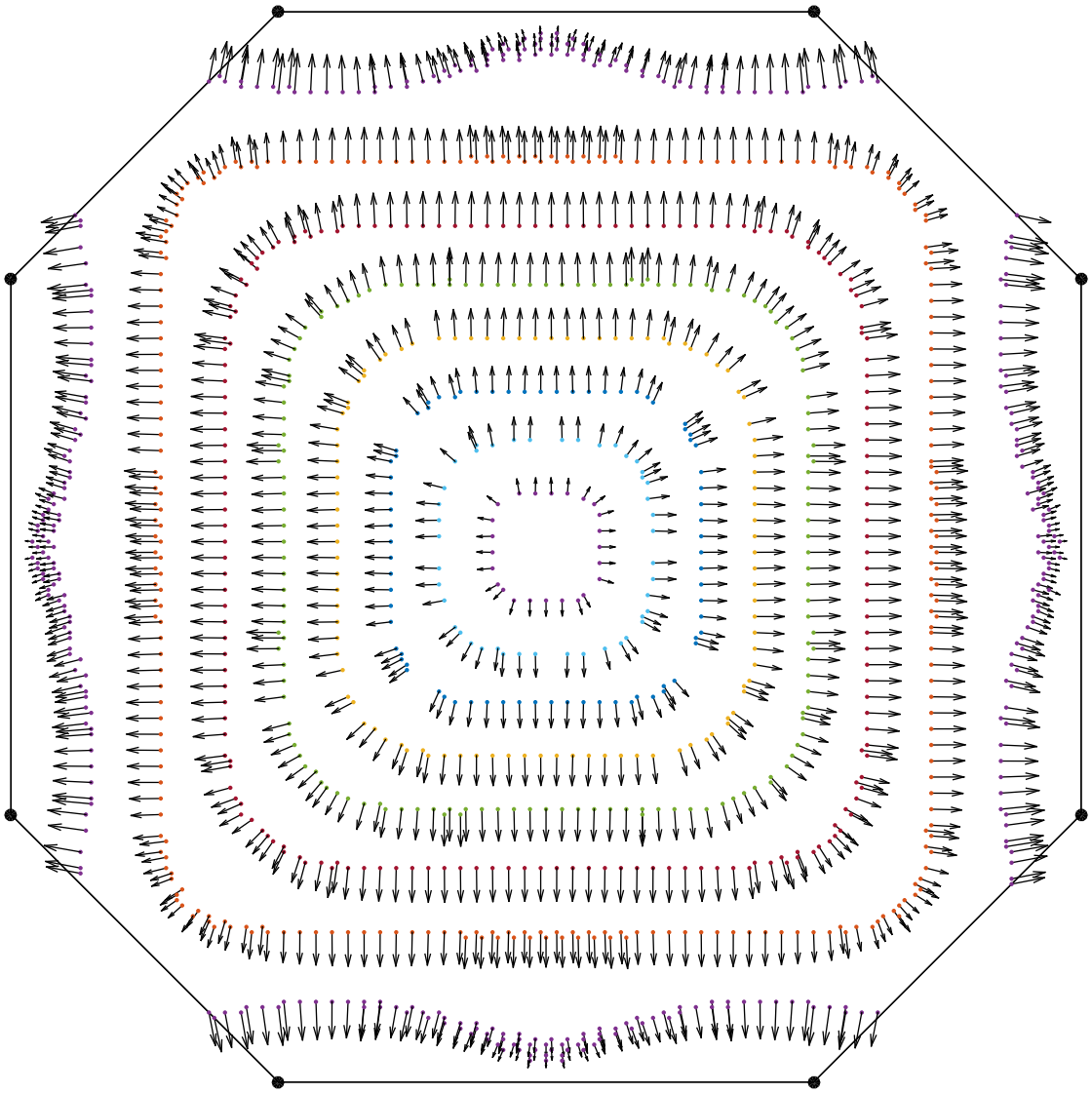

Figure 5.12: Constant frequency wavevectors of the transverse acoustic branch. The arrows protruding from each wavevector indicate the direction of phonon propagation in the $k_z = 0$ plane

.

will predict different peak temperatures in the simulation of a heated domain [19]. Therefore comparison of the absolute temperature profiles of two different models may not reveal the variation in heat conduction along different directions in the plane. However, this study focuses on whether or not phonon properties, and group velocities, obtained along a single high-symmetry line, are a valid description of heat

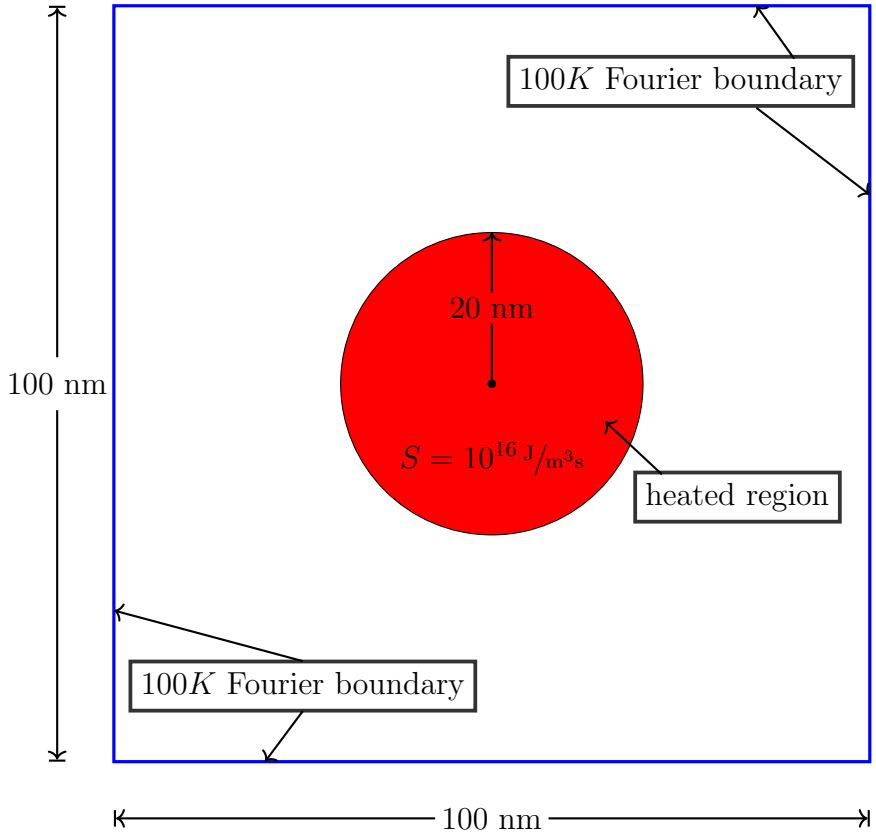

Figure 5.13: Simulation domain for the study of anisotropic effects in a thin silicon film.

transport along *all* directions. In order to study this assumption, the temperature profiles of two different Boltzmann transport models should be normalized so that the maximum temperature for each model is equal. For simplicity the following normalization is used,

$$T_{normalized} = \frac{T - T_{min}}{T_{max} - T_{min}} \qquad T_{min} = 100K \qquad . \tag{5.4}$$

The effect of this normalization is to restrict the temperatures within the domain to be between 0 and 1. Throughout the rest of this section any reference to temperature will implicitly be referring to the normalized temperature.

A reference isotropic solution was required for comparison to the anisotropic result. Therefore, a gray isotropic phonon simulation was performed to discretize and solve the Boltzmann transport equation. The spatial domain was discretized into a 71 $\times$ 71 grid of control volumes. The source term in the heated region is distributed equally into all phonon modes. The phonon properties for this simulation are identical to those used in the verification problem, which were given in Table 5.1. Due to the symmetry of the problem only a quarter of the plate was actually simulated, the constant temperature contours of the isotropic simulation are given in Fig. 5.14.

An anisotropic simulation was subsequently performed. All material and phonon properties of silicon were obtained from the molecular dynamics approach detailed in Sec. 4.1. The relaxation time model used was detailed in Sec. 4.1.2. Since the purpose of this study is to investigate the directional dependence of heat transport, only acoustic phonon modes were included in the simulation. The same spatial mesh that was used in the isotropic simulation is used in the anisotropic case. The source term was again equally distributed amongst all phonon modes. The constant temperature contours for the anisotropic simulation are given in Fig. 5.15. Note the flattening of the temperature contours along the diagonal direction, this flattening is most evident for the .3 temperature contours.

In order to directly compare the isotropic simulation to the anisotropic simulation, the difference between the two temperature profiles was taken. To obtain the difference in the temperature profiles, the cell centered temperature values of the anisotropic simulation were subtracted from the cell centered temperatures of

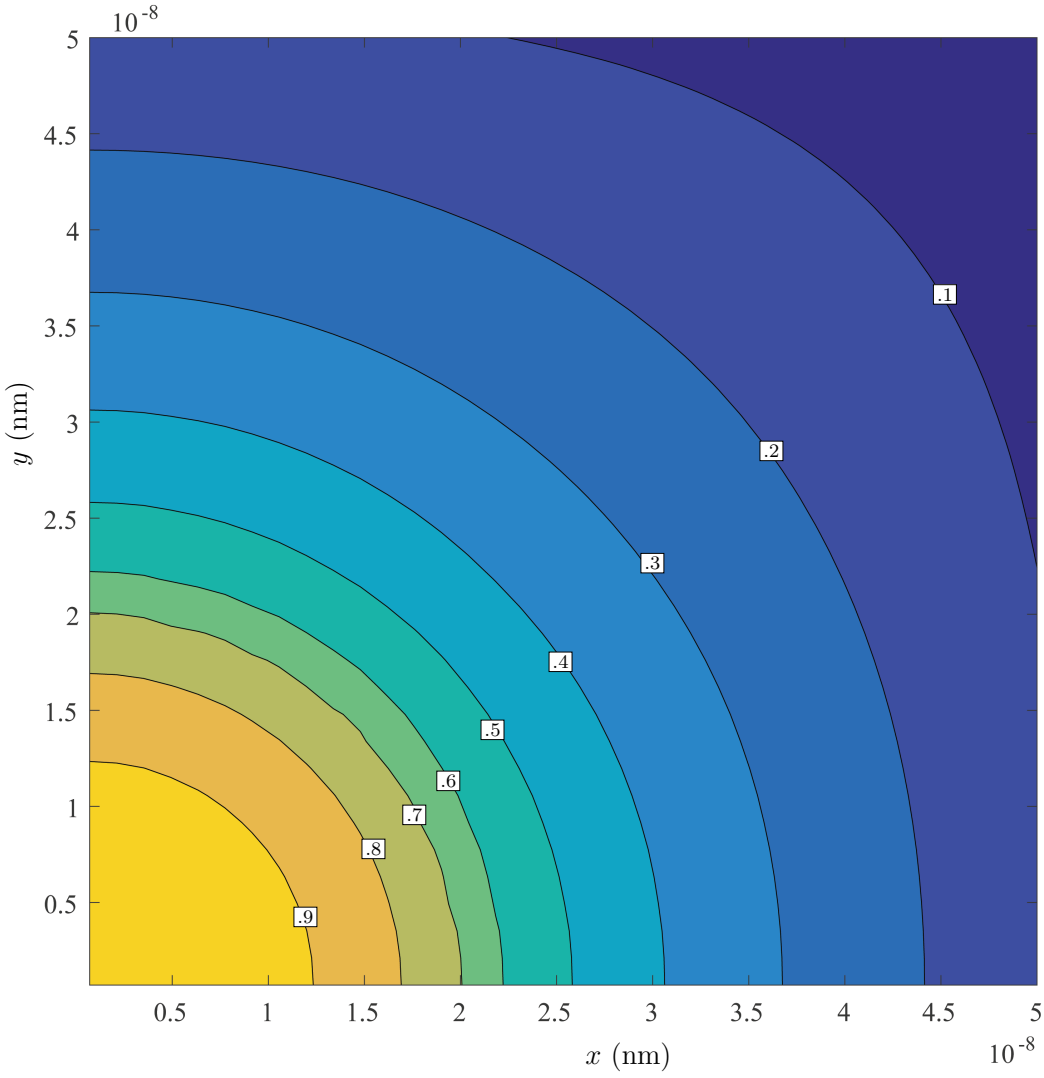

Figure 5.14: Constant temperature contours obtained through solving the gray isotropic Boltzmann transport equation

the isotropic simulation,

$$T_{diff} = T_{isotropic} - T_{anisotropic} \quad . \tag{5.5}$$

The contours of the temperature difference of the two simulations are given in Fig. 5.16, in addition the percent differences between the two simulations are given in 5.17.

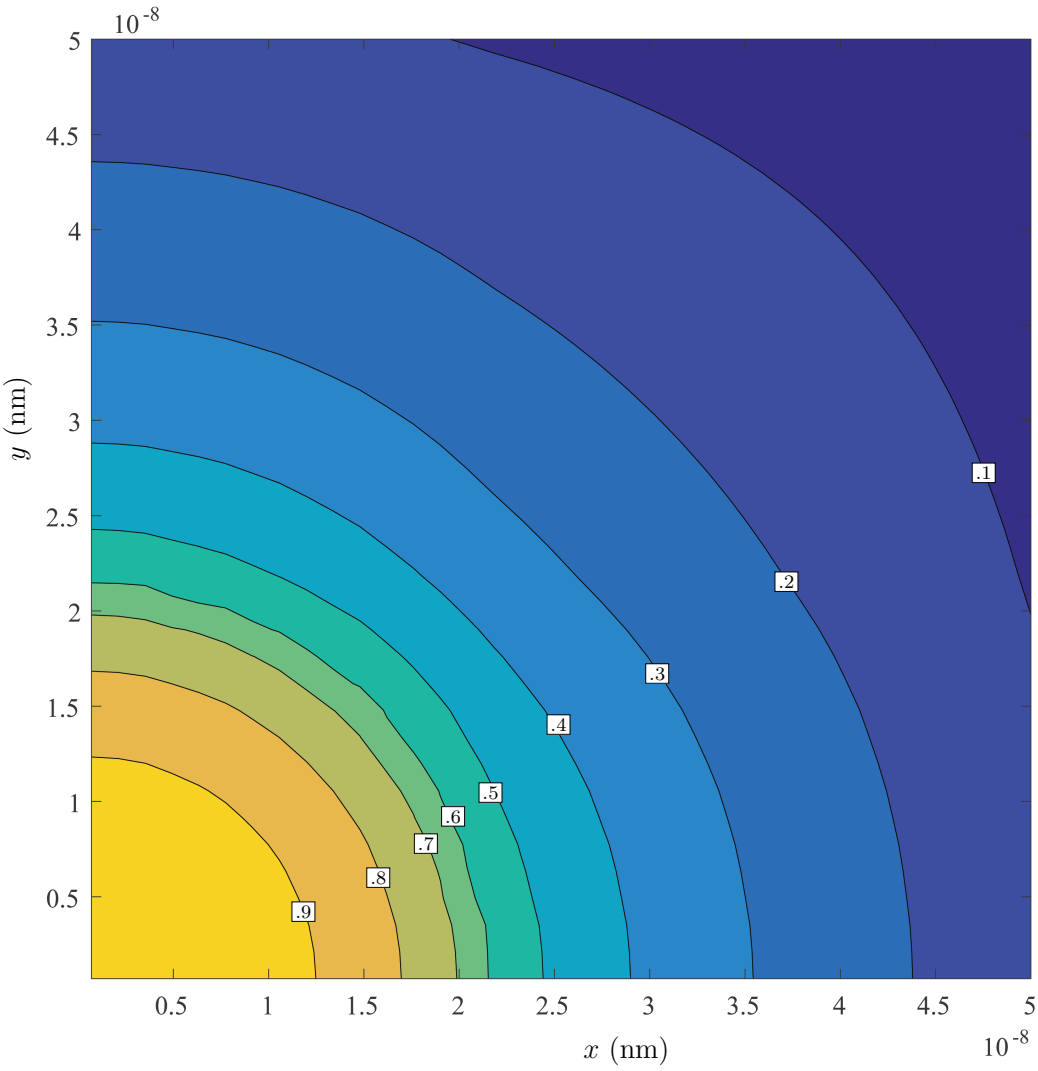

Figure 5.15: Constant temperature contours obtained through solving the fully anisotropic Boltzmann transport equation

The difference in the two solutions reveals that the isotropic assumption does lead to error in determining the temperature profiles. Furthermore this error is largest along the diagonal direction. This can be explained by considering the frequency and group velocity behavior within the Brillouin zone (Figures 5.10, 5.11, and 5.12). These figures demonstrate that the transverse acoustic modes preferably transport energy along the $\pm x$ or $\pm y$ directions as opposed to along any direction.

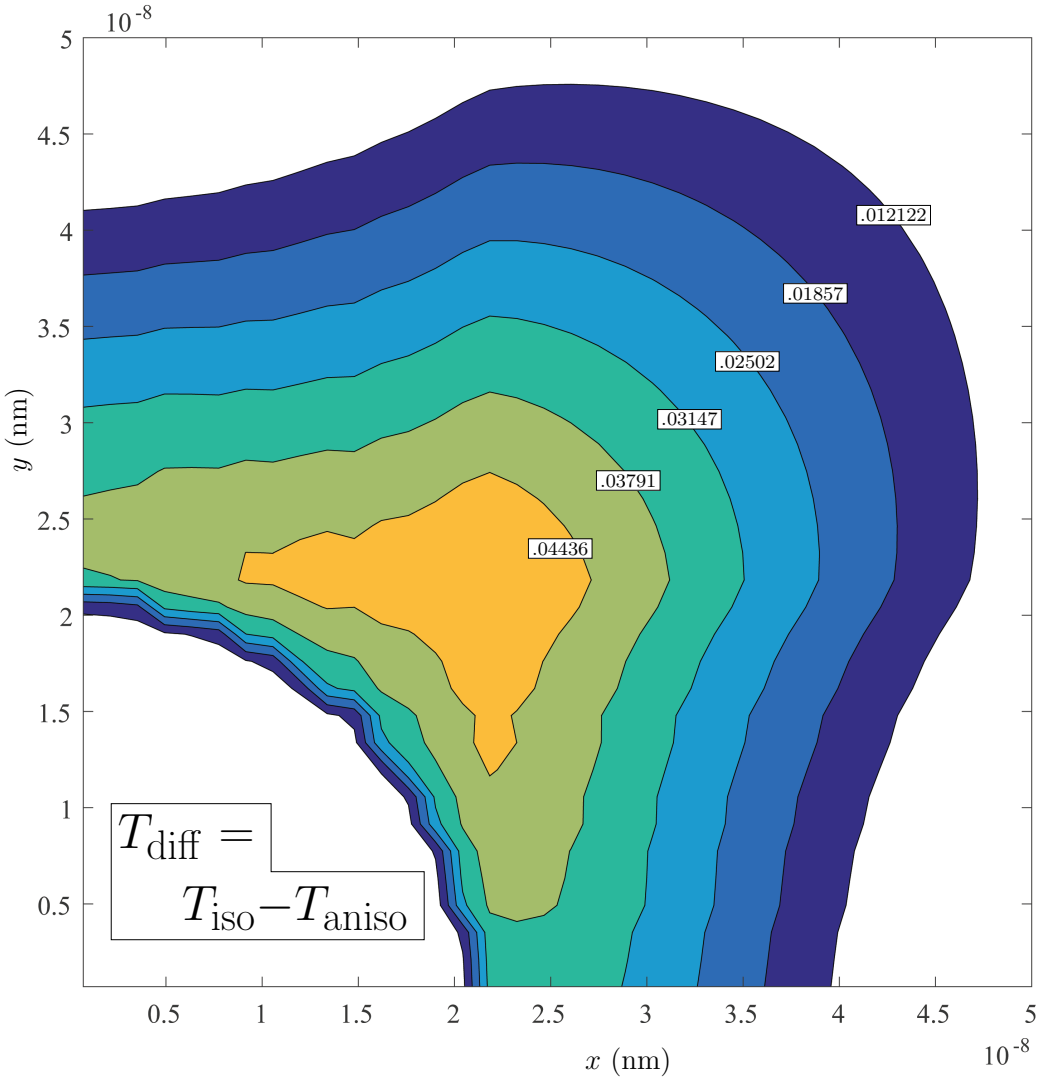

Figure 5.16: Constant temperature difference contours obtained by subtracting the anisotropic cell centered temperatures from the isotropic cell centered temperatures.

Therefore, by assuming that transport along the $\pm x$ or $\pm y$ direction is the same as along the plate diagonal, as is done within the isotropic assumption, the advection along the diagonal is exaggerated. This leads to an over prediction of temperatures along this diagonal line as seen in the temperature difference contours.

Note that the largest temperature difference occurs at 40.833 nanometers from the origin and 20.833 nanometers from the source term boundary. The majority of

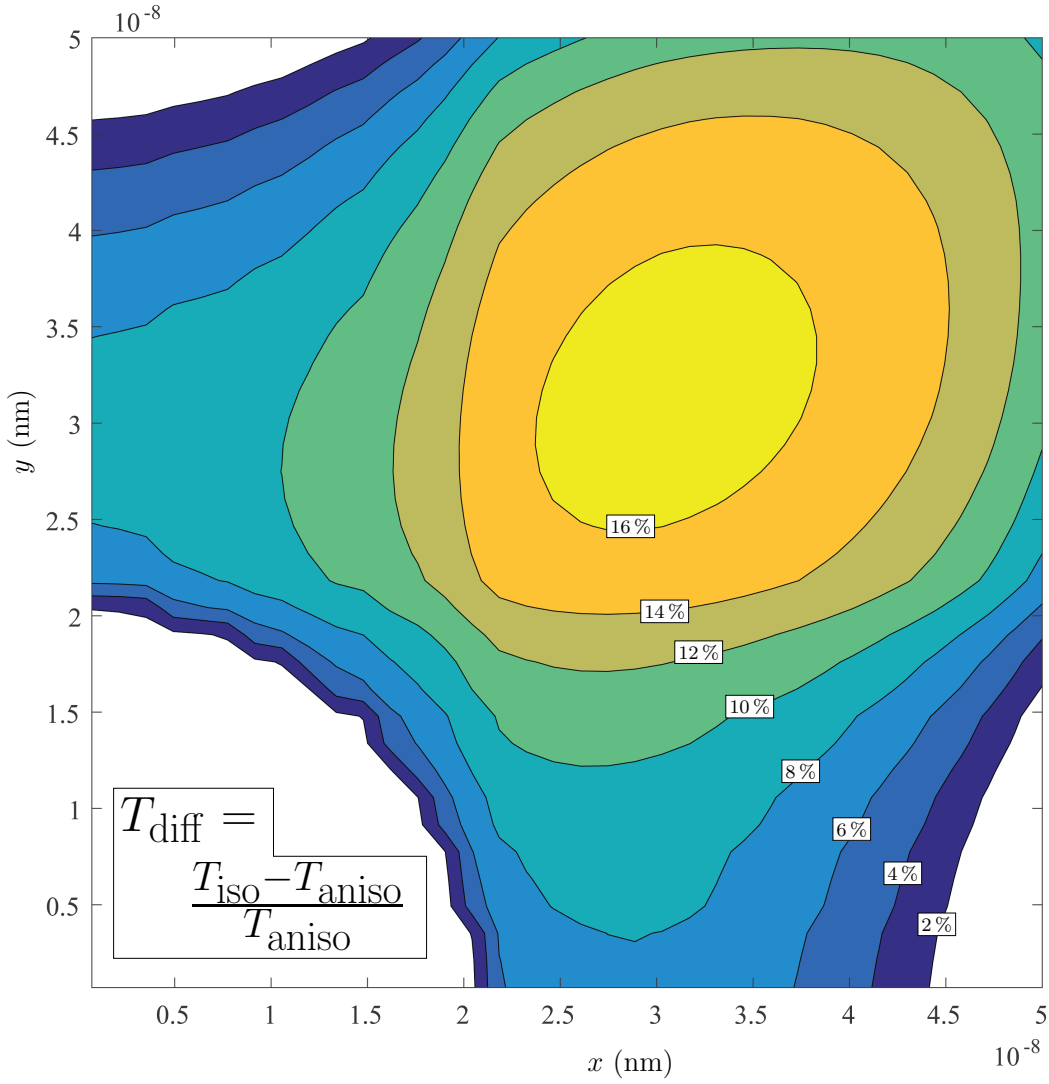

Figure 5.17: Percent difference contours between the isotropic and anisotropic simulations.

longitudinal and transverse acoustic phonons will traverse this distance ballistically without experiencing phonon-phonon scattering. Therefore the isotropic assumption introduces artificial advection in certain directions. The difference between the two models is least along the $\pm x$ or $\pm y$ direction as these directions correspond to the direction in which the majority of transverse acoustic phonon modes propagate, see Fig. 5.12. Finally note that at distances far from the source the two models agree

closely. This is a result of transport transitioning from ballistic to more diffusive at these distances. At large distance, transport is dominated by diffusion, resulting from the relaxation time term, as opposed to advection which is not accurately modeled through the isotropic model. Therefore the isotropic assumption differs the most from a fully anisotropic solution in regions where transport is dominated by advection.

From the results presented in this section it appears that use of the isotropic assumption may not be valid for two dimensional phonon transport simulations. The cause for the inaccuracy, which arises from the isotropic assumption, stems from the anisotropy of frequencies within the Brillouin zone. As a result of this anisotropy, the group velocities, determined by the frequency values, advect phonons preferentially along certain directions, leading to an anisotropy in phonon transport.

5.3 FinFET Design and Self-Heating

The Boltzmann transport equation algorithm presented in this work, is capable of modeling nanoscale heat flow in three dimensions. This capability has application in the simulation of field effect transistors with a three dimensional fin geometry (FinFET). The benefit of modeling the temperature profile in a transistor is two fold. First it is important to determine the maximum temperature within a transistor as critical electronic properties of the transistor are negatively affected by temperature. These electronic properties include the drain saturation current and the threshold voltage [11]. Sufficiently large temperatures reduce saturation current

and threshold voltage, effectively reducing the transistor lifetime [11]. Therefore thermal profile information is critical in determining possible failure in such devices as well as predicting the long term reliability of the transistor device. The usefulness of the simulation is enhanced by the fact that experimental measurements of transistors are difficult to perform due to the nanometer length scales of current transistor designs. The second benefit of nanoscale modeling lies in the profiling of new transistor designs. A wide array of device geometry parameters may be varied and the temperature profile within the device may be modeled using the presented algorithm to determine the design which most efficiently dissipates heat. The set of geometric parameters which yield the lowest peak hotspot temperature should maximize device performance and lifetime.

5.3.1 Problem Set-Up

A parameter study of a silicon on insulator (SOI) fin field effect transistor (FinFET) was performed with the goal of analyzing the effect of fin width, and source region geometry, on the peak temperature obtained within the fin. Three fin widths were chosen as well as three source region geometries. In order to allow for comparison between the various parameter combinations the overall energy sourced into each FinFET is maintained at a constant value. The parameter values for the FinFET and source region were drawn from the literature to ensure that the simulations reflect realistic physical conditions of FinFET transistor devices. The FinFET device has a characteristic length scale of ten nanometers, reducing the

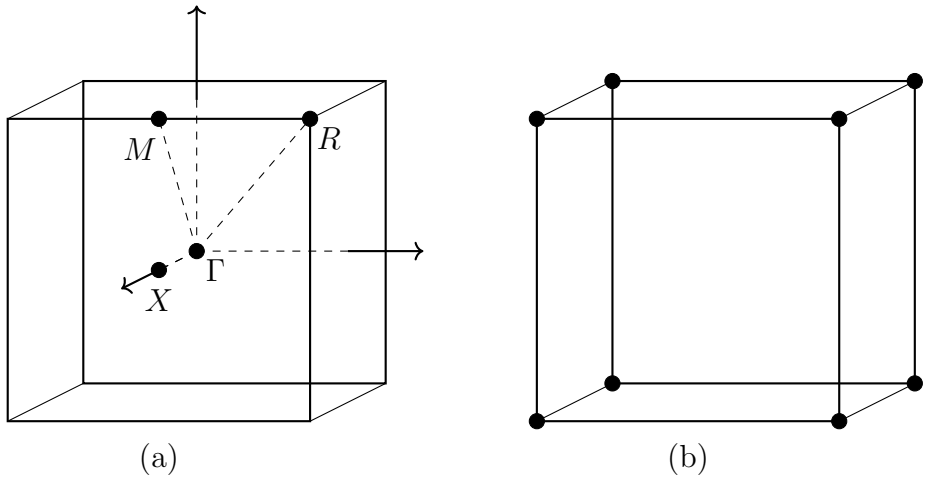

Figure 5.18: Idealized Simple Cubic Lattice: (a) Brillouin Zone including high symmetry points (Γ, X, M, and R) and lines (dotted), (b) real space lattice primitive unit cell with atoms at vertices.

number of allowed vibrational modes as compared to a bulk device. In addition the FinFET length scales are on the same order of magnitude as the phonon MFP's placing transport within the fin in the semi-ballistic regime. The device geometry, source terms, and boundary conditions all vary in three dimensions, resulting in three dimensional temperature profiles. Therefore, the wide array of features within the presented Boltzmann algorithm are required for accurate modeling of the SOI FinFET device.

For simplicity, it was assumed that the FinFET is composed of an idealized Lennard-Jones solid with a simple cubic crystal lattice, the real space unit cell as well as the associated Brillouin zone of the material are depicted in Fig. 5.18. The chosen interatomic potential is the Lennard-Jones potential which has the form:

$$V_{LJ,n}(r_{ij}) = 4B_n \left(\frac{A_n^{12}}{r_{ij}^{12}} - \frac{A_n^{6}}{r_{ij}^{6}} \right) \qquad ; \qquad n = NN \text{ or } NNN \ ,$$

here r_{ij} is the distance between atom i and atoms j, A_n and B_n are constants chosen to reproduce the lattice constant and frequency spectrum displayed by common semiconductor materials, and NN and NNN represent the interactions between nearest neighbor and next-nearest neighbor respectively. The constants appearing in the interatomic potential are given in Table 5.2.

Empirical Potential Constants	
A_{nn}	4.4545×10^{-10} meters
B_{nn}	2.7×10^{-20} Joules
A_{nnn}	6.2996×10^{-10} meters
B_{nnn}	1.9×10^{-20} Joules

Table 5.2: Lennard Jones parameters

The phonon properties are determined from the analytical form of the interatomic potential, using the methods detailed in Sec. 3.3 and 4.1. The resulting dispersion along the high symmetry lines of the cubic Brillouin zone are given in Fig. 5.19. From the dispersion relations, the phonon group velocities are obtained through the central differencing procedure outlined in Sec. 4.1.

The phonon relaxation times are obtained from literature values given in ref. [1]. This relaxation time model was chosen as it accounts for the temperature and frequency dependence of relaxation times. In addition the model differentiates between both longitudinal and transverse modes as well as between normal and

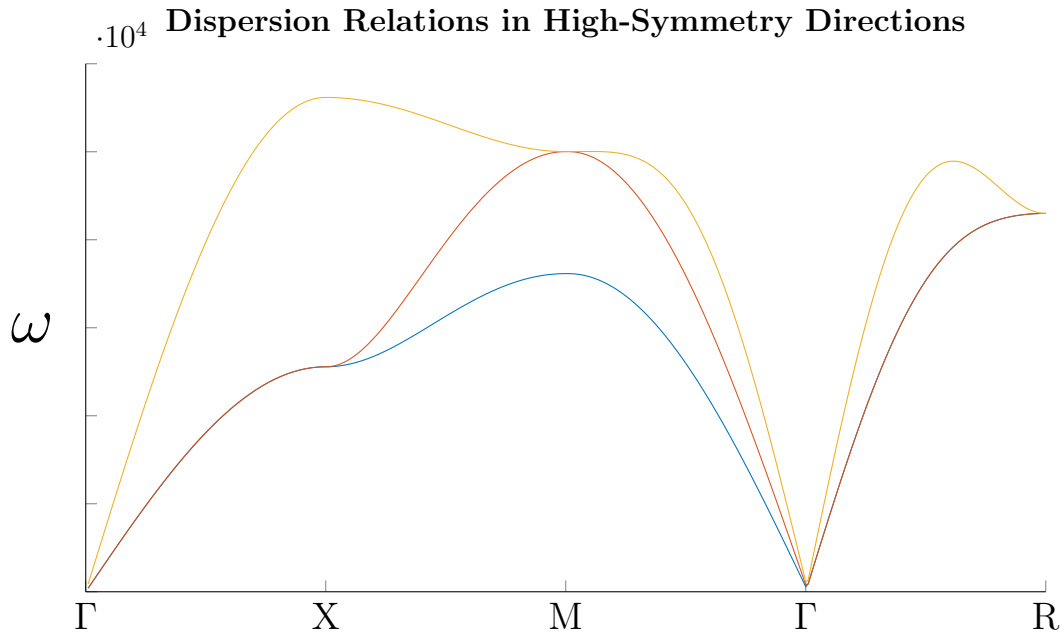

Figure 5.19: Frequency - wavevector relations for a series of high-symmetry lines within the first Brillouin zone

Umklapp scattering processes. Finally, the functional forms have been fit to experimental data and accurately reproduce the thermal conductivity values in semiconducting materials [1]. The functional forms of the various phonon scattering rates, along with the parameter values, are reproduced from [1] in Tables 5.3 and 5.4.

A source term is incorporated into the appropriate BTE's in order to model electron - phonon interactions or Joule heating. Joule heating occurs when high energy electrons interact with the lattice, transferring their energy to the lattice and creating phonons. The vast majority of electron-phonon interaction occurs within a region of the transistor known as the *channel* [9]. The location of this channel region is assumed to coincide with the fin region of highest electron density. Due to the high energy of electrons within the channel, the majority of energy is known to be transferred to high frequency phonons [9]. In order to capture this effect, a

Phonon Branch	Umklapp Scattering Rate (τ_U^{-1})	Normal Scattering Rate (τ_L^{-1})
Transverse	$B_{TU}\omega^2 T e^{-C_T/T}$	$B_T \omega T^4$
Longitudinal	$B_{LU}\omega^2 T e^{-C_L/T}$	$B_L \omega^2 T^3$

Table 5.3: Functional form of the phonon scattering rates from [1]

Scattering Rate Parameters	
B_T (K^{-4})	2×10^{-13}
B_{TL} (s/K^{-3})	2×10^{-21}
B_{TU} (s)	1×10^{-19}
B_{LU} (s)	5×10^{-19}
C_T (K)	55
C_L (K)	180

Table 5.4: Parameter values for phonon scattering rates in Table 5.3 given by [1]

source term is included in the BTE's (i.e. $S_{\boldsymbol{k}} \neq 0$ in Eq. 4.31) corresponding to phonon states which have a frequency $\omega(\boldsymbol{k}) \geq \omega_{max}/2$ where ω_{max} is the maximum vibrational frequency of the material. As a result of this assumption, energy is injected into high frequency modes which tend to have lower group velocity and are thus inefficient at transporting thermal energy. Therefore the removal of heat will require energy to decay from high frequency modes to lower frequency modes which then carry the heat away from the heated region.

Joule heating occurs in the regions of the transistor with high electron density, i.e. the channel. Electron density may be determined through solving the problem of electron transport, this is typically done using the Monte Carlo method to solve the

Boltzmann transport equation for electrons [56]. The electron density for the device considered in this study is found to vary with the applied gate voltage [3], where as the gate voltage is increased, electrons are pulled toward the gate interface at the corners of the device, see Fig. 5.20. To capture this variation, the parameter study

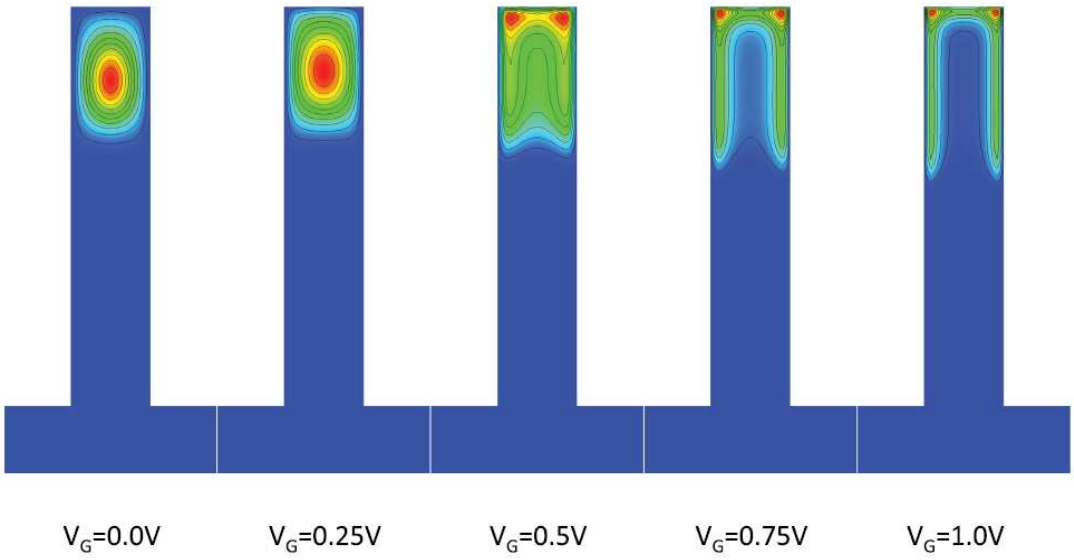

Figure 5.20: Evolution of carrier concentration with applied gate voltage, figure obtained from [3]

considers three different configurations of the source region. These configurations are meant to reflect the location and size of the channel for a range of applied voltages, these regions are depicted in Fig. 5.21. The source is applied in such a manner that the energy injected into the channel is constant for all fin widths and for all channel geometries (the three regions are henceforth referred to as channel

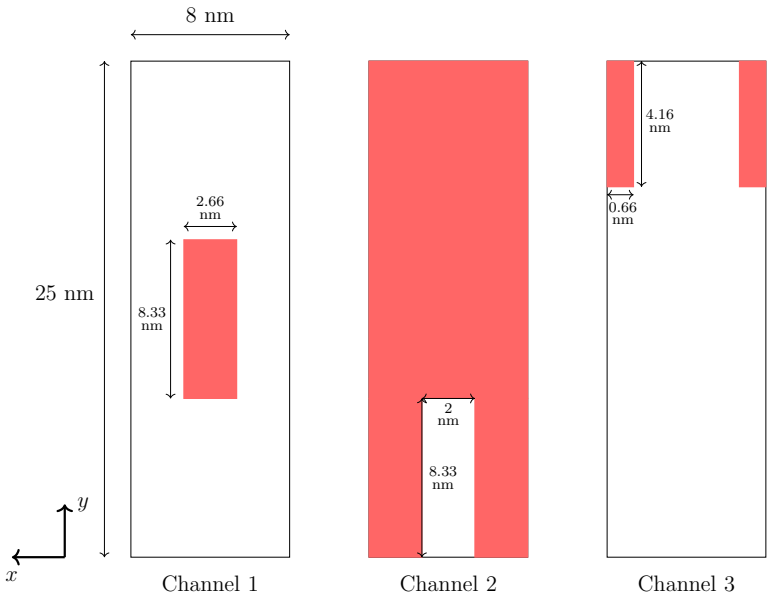

Figure 5.21: Three channel geometries simulated in FinFET device. Channel I corresponds to low applied gate voltage, channel II corresponds to medium applied gate voltage, and channel III corresponds to high applied gate voltage.

I, channel II, and channel III). The depth (in the x-direction, i.e. into the page) of all channels is set to 10 nanometers, this value was found to be the length of the channel from Monte Carlo simulations of electron-phonon coupling [8]. The simulation domain dimensions are varied to investigate the effect of fin width on the temperature profile within a FinFET. Three simulation domains were considered, depicted in Fig. 5.3.1. The geometries of the devices being simulated are drawn from [3] and reflect current FinFET transistor device design.

Due to symmetry in the x and y directions only a quarter of the FinFET need be simulated, however the allowed wavevectors must reflect the dimensions of the full crystal. The quarter domain to be simulated is depicted in Fig. 5.25 along with the associated boundary conditions. Specular boundary conditions are applied

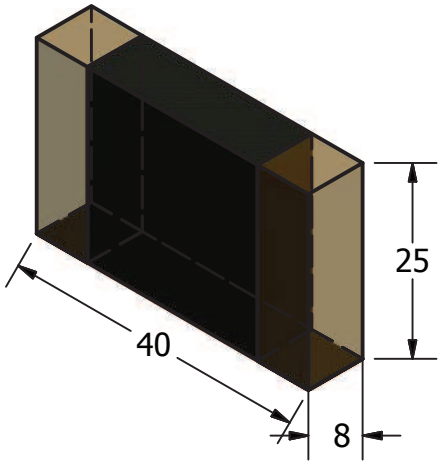

Figure 5.22: Thin Fin

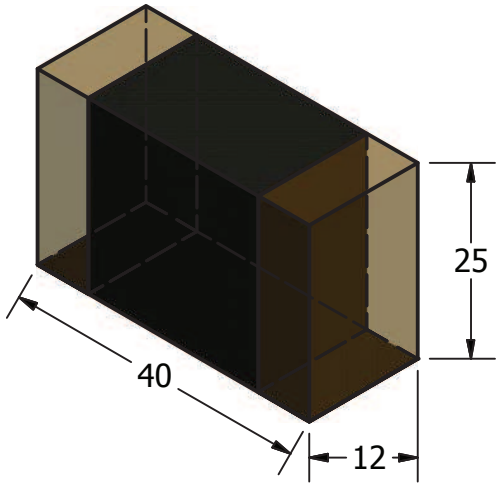

Figure 5.23: Medium Fin

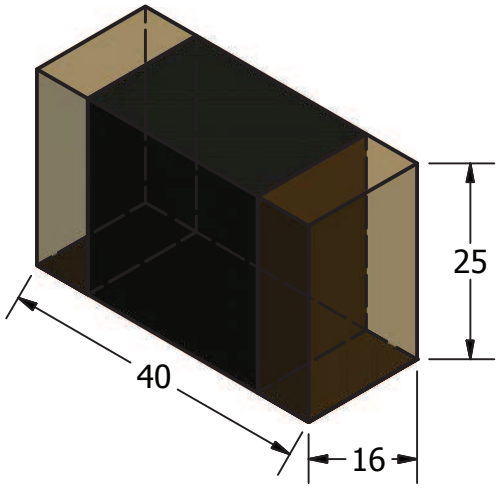

Figure 5.24: Thick Fin

to the symmetry surfaces. Diffuse boundary conditions are applied to the exposed surfaces of the FinFET as fabrication techniques for these devices cause disorder in atoms near the surface [92], this disorder results in diffuse phonon scattering at these boundaries. Finally, Fourier boundary conditions are applied to the silicon/silicon dioxide interfaces. It is assumed that the majority of heat generated within the FinFET is removed through these surfaces. All Fourier boundary conditions are set

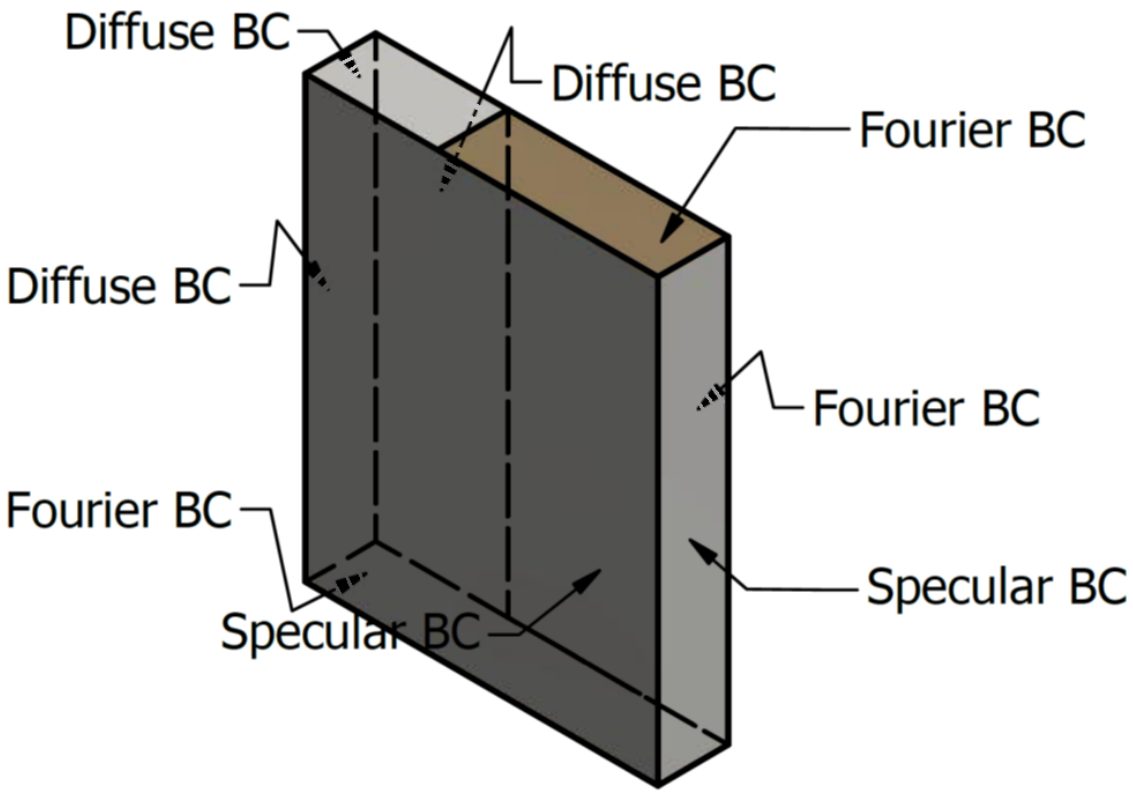

Figure 5.25: Boundary conditions applied to the simulation domain.

to 300 K, where it is the maximum rise in temperature over 300 K that is of the most importance to the performance of the FinFET.

5.3.2 Device Simulation Results

With the phonon inputs, and physical properties defined, device simulations were performed for all three channels and all three fin widths, resulting in a total of nine simulations. The temperature contours of each simulation are grouped based on the channel region in order to illuminate the effect of fin width (Figs 5.26, 5.27, and 5.28).

Consider channel I whose temperature contours are given in Fig. 5.26. Begin by noting that the region of maximum temperature occurs in the center of the

channel region. Furthermore, the temperatures are highest within the channel and decrease sharply outside the channel. Both of these effects are a result of energy being distributed to high frequency modes with low group velocity due to electron-phonon interactions within the channel. As a result energy is confined to the channel region before decaying into lower frequency modes with higher group velocity which are capable of transporting energy out of the domain. Note also the slight temperature rise which occurs in the $(+x, +y, +z)$ region. This is a result of the adiabatic boundary conditions trapping phonons in the domain, all energy must leave via the $(-y)$ plane or through the $(-z)$ plane. Finally, it is important to consider the trend in maximum channel temperature as this will have the largest effect on the electrical performance of the FinFET. The trend observed here is that as the fin width decreases, the peak temperature increases.

Consider now channel II temperature contours, which are given in Fig. 5.27. The temperature profile for this channel region is spread over a larger portion of the domain as a result of spreading of the source term. Recall that this spreading effect comes from an increase in the applied gate voltage which reduces the spatial electron density. The temperature profile inside the domain is observed to be less than for channel I. This reduction is a result of shifting the channel region closer to the Fourier interface boundary. By moving the channel closer to the Fourier boundary which allows phonons to flow out of the domain, heat generated in the high frequency modes with low group velocity can be transported out of the domain directly. Therefore, the process in which energy must be transferred to lower group velocity modes (a process which is limited by the mode relaxation times), before

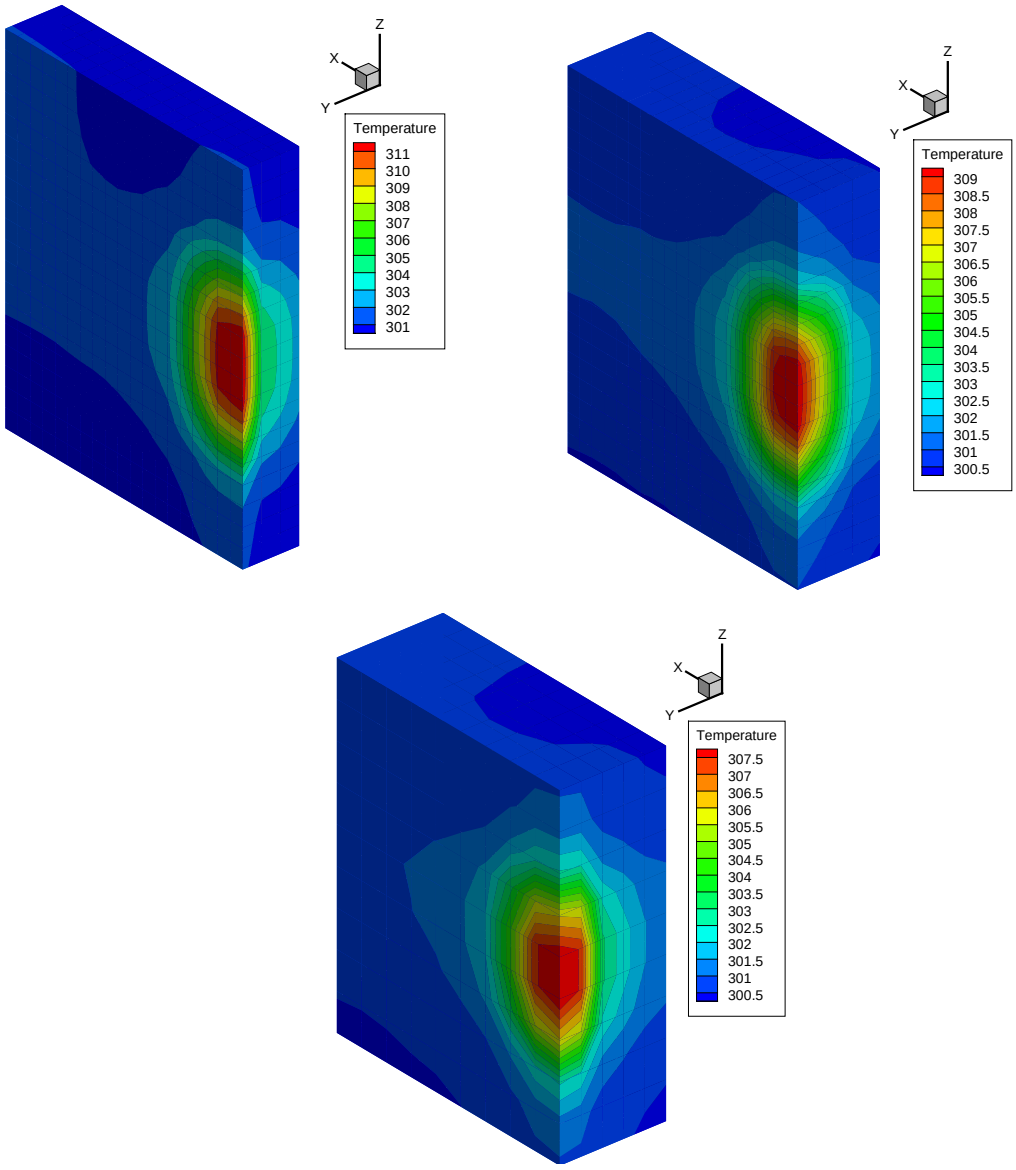

Figure 5.26: Temperature profiles for channel 1. All temperatures are reported in units of Kelvin.

being transported out of the system, is partially circumvented. This more efficient process of heat removal results in the lower overall temperatures observed in channel II. Again, note the trapping of energy along the $(+x, +z)$ boundary edge, resulting from adiabatic boundary conditions. As with channel I, an decrease in fin width corresponds to an increase in maximum temperature for channel II.

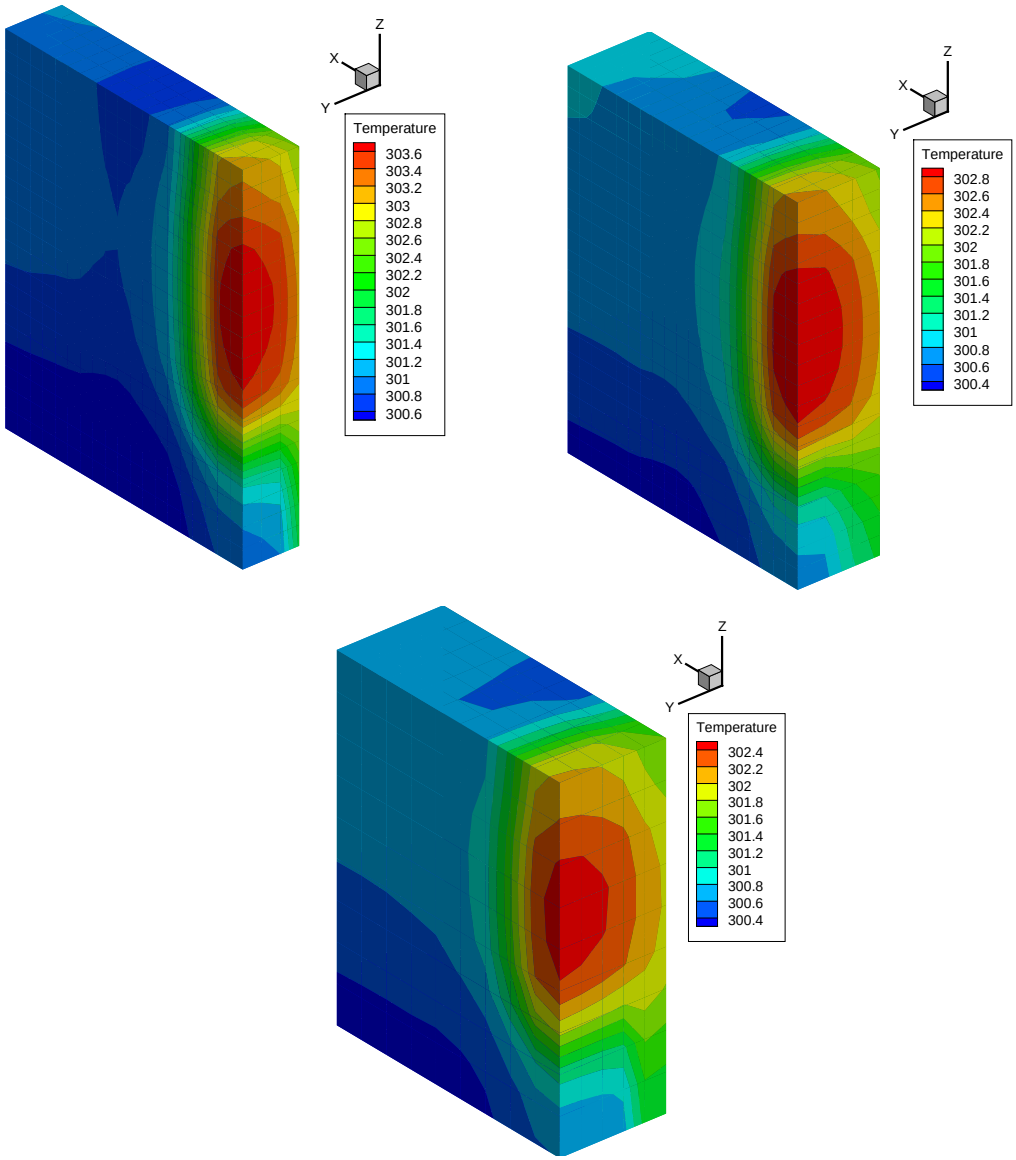

Figure 5.27: Temperature profiles for channel 2. All temperatures are reported in units of Kelvin.

Finally, consider the channel III temperature contours given in Fig. 5.28. This channel configuration produces the highest temperatures. These temperature contours strongly mirror the channel region itself. Channel III lies along a Fourier interface boundary as does channel II. However, as opposed to channel II, the large energy generation which exists in channel III cannot be efficiently dissipated by high frequency phonon modes. This results in channel III displaying the largest overall

temperature profiles with respect to the 300 K. Also note the sharp temperature gradients in regions near the channel. This effect is characteristic of non-equilibrium ballistic transport at the nanoscale and has been observed in similar device simulations [64]. These sharp temperature gradients are qualitatively different than those that would be obtained through a classical simulation using Fourier's equation of heat transfer. Such a simulation assumes diffusive transport and would yield smoother temperature gradients. Finally the trend in maximum hotspot temperature is again that decreasing fin width increases the peak channel temperature.

The central quantity of interest is the maximum temperature rise within the domain with respect to 300 K. The maximum temperature for all fin widths and channels is given in Table 5.5. Several conclusions may be drawn from these results.

	Thin Fin	Medium Fin	Thick Fin
Channel 1	312.245 K	309.735 K	308.276 K
Channel 2	303.823 K	303.024 K	302.535 K
Channel 3	324.966 K	319.044 K	316.048 K

Table 5.5: Maximum temperature rise in each simulation.

First, as the channel becomes smaller, corresponding to larger applied gate voltages, the maximum temperature rise increases. This is to be expected as channel III corresponds the to the highest electron densities within any channel and therefore the largest source term. The high source term, in addition to the low group velocity

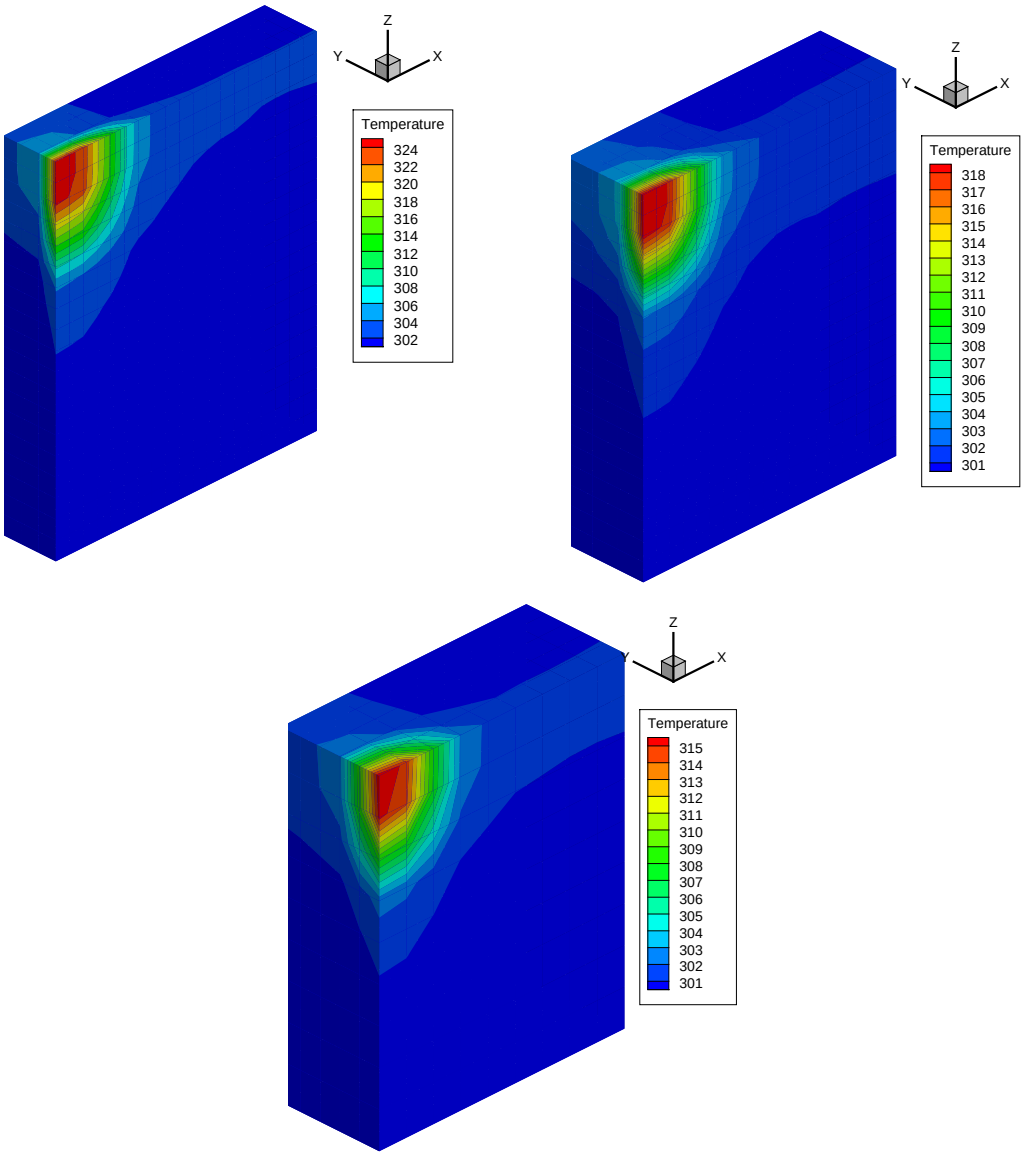

Figure 5.28: Temperature profiles for channel 3. All temperatures are reported in units of Kelvin.

of phonon modes receiving the energy, lead to large temperature rise of the channel. Furthermore, a clear trend emerges, for all channels, when considering the variation of fin width. Namely as the fin width decreases, so does the maximum temperature achieved in the channel. This effect results from introducing the same amount of energy into a smaller volume leading to an overall temperature rise.

In the final portion of this section the energy density of two particular phonon modes are visualized, henceforth referred to as mode 1 and mode 2. Tracking the energy flow within an individual phonon mode represents a capability unique to the Boltzmann transport equation algorithm presented in this work, whereby individual mode occupancies may be be examined since the BTE is solved for all allowed wavevectors and branches within the Brillouin zone. Consider the phonon properties of mode 1 and mode 2 which are detailed in Table 5.6. The energy density profiles

	Mode 1	Mode 2
Frequency (THz)	117.20	7.89
Group Velocity ($^{\text{meters}}/_{\text{sec}}$)	$0\hat{\boldsymbol{x}} + 0\hat{\boldsymbol{y}} + 0\hat{\boldsymbol{x}}\hat{\boldsymbol{z}}$	$-4882.8\hat{\boldsymbol{x}} + 1656.37\hat{\boldsymbol{y}} + 973.58\hat{\boldsymbol{z}}$
Source Term ($\omega > {}^{\omega_{max}}/_{2}$)	Yes	No
Relaxation Time (picoseconds)	69.74	28.37

Table 5.6: Phonon properties of two vibrational modes.

of these two modes for channel II in the 8 nm wide fin are detailed in Fig. 5.29. These modes are chosen to highlight the wide array of phonon physics that manifest within nanoscale devices for two different modes within the first Brillouin zone.

Analyzing the energy profiles of the two modes, it is clear that the individual phonon modes may behave in a manner quite different from one another as well as from the total energy density profile, which is given in Fig. 5.27 (recall that energy and temperature are proportionally related through the specific heat, this relation

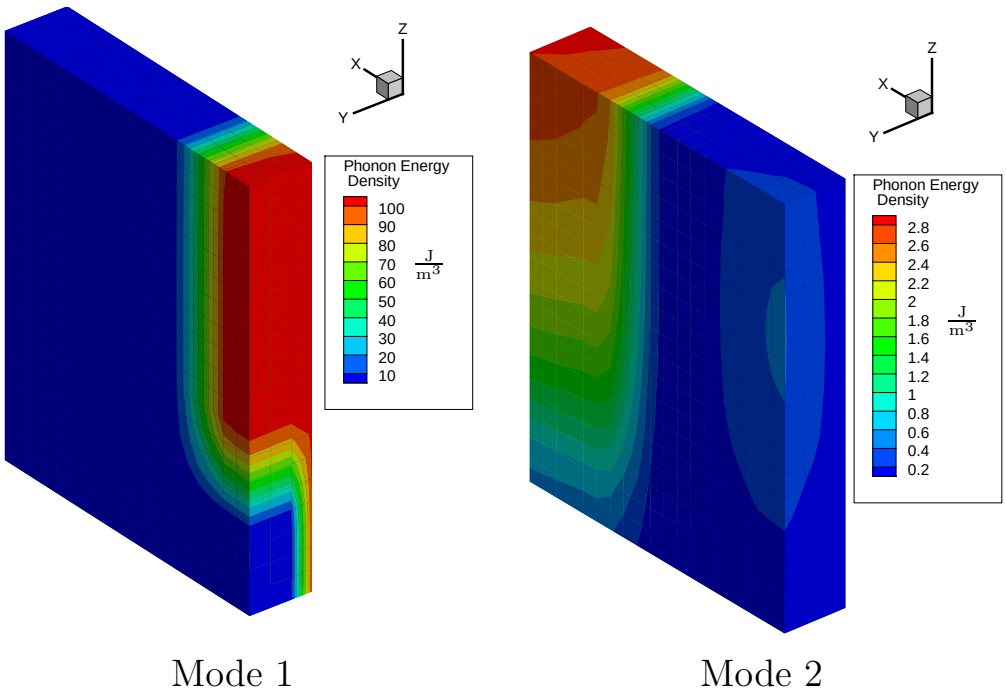

Figure 5.29: Energy profiles of mode 1 and mode 2. The parameters correspond to the 8 nm fin width and channel 1 geometry

is given in Eq. 4.30). Considering mode 1 first, note that the shape is identical to the channel geometry. This is a result of mode 1 having zero group velocity, therefore none of the energy deposited into this mode can be directly transported. Rather, energy must decay into other phonon modes through scattering processes, modeled through the relaxation time term, before being transported. Therefore it is capacitative modes such as mode 1 that are responsible for the self heating effects in nanoscale devices.

Mode 2 has an energy profile which is much different from that of the overall energy density profile, this departure arises from a multitude of factors. First, mode 2 is of low enough frequency that it does not directly receive energy from the source term, rather any energy injected into this mode is through phonon-

phonon scattering modeled by the relaxation time term or through in-scattering from boundaries. Furthermore, the region of the material in which the mode is excited is far removed from the hotspot region, see Fig. 5.27. This separation arises from energy decaying from capacitative modes, such as mode 1, into lower frequency (and higher group velocity) modes which then transport energy away from the domain. When these modes reach the far end of the domain, i.e. the surface normal to the $+\hat{\boldsymbol{x}}$ direction, they scatter and diffusely redistribute their energy into mode 2. Finally it is important to note that mode 2 has a much lower energy density than mode 1, indicating dominance of the source term over phonon-phonon scattering when increasing the occupancy of the mode. The dominance of phonon generation by the source term results in the overall energy density profile more closely mirroring mode 1, whose BTE contains a source term, over mode 2, whose BTE does not.

In this section a study of a FinFET device has been performed with the goal of characterizing the effect of fin geometry as well as source term geometry on the temperature profiles within the fin. Of specific interest is the peak temperature achieved, as this has the largest effect on the electronic performance of the FinFET. It is found that decreasing fin width corresponds to an increase in peak temperature of the hotspot. Furthermore, the capability of visualizing individual mode occupations was demonstrated by considering two phonon modes with different phonon properties. Capturing phonon physics of individual phonon modes is an inherent capability of the presented algorithm, a capability not available the majority of BTE solvers which appear in the literature.

Chapter 6: Conclusion

6.1 Closure

The main goal of this thesis was to solve the fully anisotropic Boltzmann transport equation for all allowed wavevectors and branches in the first Brillouin zone and apply this method to nanoscale device simulation. To this end the challenges inherent in nanoscale thermal modeling were introduced, and a literature review was presented of previous work that had been performed in the area of nanoscale thermal modeling. Work done on nanoscale thermal modeling within the framework of solving the Boltzmann transport equation was highlighted to demonstrate that the BTE provided accurate description of thermal transport in nanoscale devices. However, it was noted that many of these works employed simplifying assumptions which did not fully account for the variation of phonon properties throughout the anisotropic Brillouin zone.

Following the literature review, the theory behind the physics of phonons was reviewed. The lattice dynamical approach to obtaining phonon properties was covered, and the difficulties in accurately described phonon-phonon collisions was discussed. A relaxation time model was chosen which accurately captured scattering in thin films. Additionally, the quantum mechanical basis for the particle viewpoint of

phonons was introduced to motivate the use of the Boltzmann transport equation. Finally the notion of discrete allowed wavevectors within the Brillouin zone was presented. By solving the Boltzmann transport equation for each of these allowed wavevectors, the anisotropy of phonon properties within the Brillouin zone may be accounted for.

The algorithm for solving the BTE was given in Sec. 4. The algorithm employs a control volume discretization to solve the system of differential equations. Phonon boundary scattering is incorporated by applying specular, diffuse, or Fourier boundary conditions directly to the individual differential equations. Finally, specifics regarding the computational implementation were discussed, including parallelization of the algorithm.

In the results section, the code implementing the BTE algorithm was verified to ensure mathematical accuracy. The verification problem was borrowed from radiative transport and described transport in regimes ranging from fully ballistic to diffusive. Next the validity of the isotropic assumption, which is used in many BTE models, was tested. Comparison between the anisotropic model used in this work and the gray isotropic model revealed that the isotropic model may overestimate advection along certain direction. As a result the temperature profiles obtained from the two models differ by up to 16 %. Finally a device simulation was performed to investigate the effects of channel geometry and fin width on the peak temperatures inside a FinFET transistor. It was found that smaller channels and thicker fins tended to increase the maximum temperature, while spreading of the channel and narrowing the fin reduced peak temperatures.

6.2 Future Work

The work presented in this thesis represents the first steps towards modeling phonon transport in three dimensions for a wide variety of devices. Future work, as well as improvements to the BTE code, include:

(i) Further investigate and quantify the effect of anisotropy. This includes investigating the effects of anisotropy in all three dimensions as opposed to just two dimensions. In addition explore materials which display stronger anisotropy than silicon.

(ii) Implement the time dependent form of the Boltzmann transport equation. The unsteady form of the BTE will allow for the modeling of transient phenomena at the nanoscale which cannot be captured in the current BTE code.

(iii) Incorporate the effect of material interfaces into the framework of the BTE code. In its current state the BTE code is capable of handling only a single homogeneous material. However modern day nanoscale devices are often heterostructures with material interfaces. At such interfaces the effects of phonon scattering, absorption, and transmission need to be accounted for. Thus simulation of more complex structures will require incorporating material interfaces into the framework of the existing BTE code.

(iv) The current OpenMP implementation for parallelizing the code should be extended to MPI parallelization. While the OpenMP parallelization provides a large reduction in computing time, it is restricted to use on shared memory

platforms. Solving the Boltzmann transport equation for all allowed wavevectors, as done in this thesis, is very computationally expensive. Therefore parallelization through MPI will allow for further performance improvements that are needed for investigating larger problems.

Bibliography

[1] M Asen-Palmer, K Bartkowski, E Gmelin, M Cardona, AP Zhernov, AV Inyushkin, A Taldenkov, VI Ozhogin, Kohei M Itoh, and EE Haller. Thermal conductivity of germanium crystals with different isotopic compositions. *Physical review B*, 56(15):9431, 1997.

[2] MM Kuklja and AB Kunz. Ab initio simulation of defects in energetic materials. part i. molecular vacancy structure in rdx crystal. *Journal of Physics and Chemistry of Solids*, 61(1):35–44, 2000.

[3] Andrew R Brown, Nicolas Daval, Konstantin K Bourdelle, B-Y Nguyen, and Asen Asenov. Comparative simulation analysis of process-induced variability in nanoscale soi and bulk trigate finfets. *Electron Devices, IEEE Transactions on*, 60(11):3611–3617, 2013.

[4] More moore roadmap - itrs 2.0 white paper. Technical report, International Technology Roadmap for Semiconductors, 2014.

[5] Jeremy Rowlette, Eric Pop, Sanjiv Sinha, Mathew Panzer, and Kenneth Goodson. Thermal phenomena in deeply scaled mosfets. *IEDM Tech. Dig*, 2005:984–987, 2005.

[6] Eric Pop, Robert Dutton, and Kenneth Goodson. Detailed heat generation simulations via the monte carlo method. In *Simulation of Semiconductor Processes and Devices, 2003. SISPAD 2003. International Conference on*, pages 121–124. IEEE, 2003.

[7] Mohamed Mohamed, Zlatan Aksamija, Wolfgang Vitale, Foyzul Hassan, Kyeong-Hyun Park, and Umberto Ravaioli. A conjoined electron and thermal transport study of thermal degradation induced during normal operation of multigate transistors. *Electron Devices, IEEE Transactions on*, 61(4):976–983, 2014.

[8] Eric Pop, Sanjiv Sinha, and Kenneth E Goodson. Heat generation and transport in nanometer-scale transistors. *Proceedings of the IEEE*, 94(8):1587–1601, 2006.

[9] Eric Pop, Robert W Dutton, and Kenneth E Goodson. Monte carlo simulation of joule heating in bulk and strained silicon. *Applied Physics Letters*, 86(8):082101, 2005.

[10] Mayank Shrivastava, Manish Agrawal, Sunny Mahajan, Harald Gossner, Thomas Schulz, Dinesh Kumar Sharma, and V Ramgopal Rao. Physical insight toward heat transport and an improved electrothermal modeling framework for finfet architectures. *Electron Devices, IEEE Transactions on*, 59(5):1353–1363, 2012.

[11] Yang-Kyu Choi, Daewon Ha, Eric Snow, Jeffrey Bokor, and Tsu-Jae King. Reliability study of cmos finfets. In *Electron Devices Meeting, 2003. IEDM'03 Technical Digest. IEEE International*, pages 7–6. IEEE, 2003.

[12] Per G Sverdrup, Y Sungtaek Ju, and Kenneth E Goodson. Sub-continuum simulations of heat conduction in silicon-on-insulator transistors. *Journal of Heat Transfer*, 123(1):130–137, 2001.

[13] YS Ju and KE Goodson. Phonon scattering in silicon films with thickness of order 100 nm. *Applied Physics Letters*, 74(20):3005–3007, 1999.

[14] Baxter H Armstrong. Two-fluid theory of thermal conductivity of dielectric crystals. *Physical Review B*, 23(2):883, 1981.

[15] Adam Christensen and Samuel Graham. Multiscale lattice boltzmann modeling of phonon transport in crystalline semiconductor materials. *Numerical Heat Transfer, Part B: Fundamentals*, 57(2):89–109, 2010.

[16] PG Sverdrup, S Sinha, M Asheghi, S Uma, and KE Goodson. Measurement of ballistic phonon conduction near hotspots in silicon. *Applied Physics Letters*, 78(21):3331–3333, 2001.

[17] Rodrigo A Escobar, Sartaj S Ghai, Myung S Jhon, and Cristina H Amon. Multi-length and time scale thermal transport using the lattice boltzmann method with application to electronics cooling. *International Journal of Heat and Mass Transfer*, 49(1):97–107, 2006.

[18] JY Murthy and SR Mathur. An improved computational procedure for sub-micron heat conduction. In *ASME 2002 International Mechanical Engineering Congress and Exposition*, pages 75–84. American Society of Mechanical Engineers, 2002.

[19] Sreekant V Narumanchi, Jayathi Y Murthy, and Cristina H Amon. Comparison of different phonon transport models for predicting heat conduction in silicon-on-insulator transistors. *Journal of Heat Transfer*, 127(7):713–723, 2005.

[20] Sreekant VJ Narumanchi, Jayathi Y Murthy, and Cristina H Amon. Boltzmann transport equation-based thermal modeling approaches for hotspots in microelectronics. *Heat and mass transfer*, 42(6):478–491, 2006.

[21] Eric Pop, Robert W Dutton, and Kenneth E Goodson. Analytic band monte carlo model for electron transport in si including acoustic and optical phonon dispersion. *Journal of Applied Physics*, 96(9):4998–5005, 2004.

[22] David Lacroix, Karl Joulain, and Denis Lemonnier. Monte carlo transient phonon transport in silicon and germanium at nanoscales. *Physical Review B*, 72(6):064305, 2005.

[23] Jean-Philippe M Péraud, Colin D Landon, and Nicolas G Hadjiconstantinou. Monte carlo methods for solving the boltzmann transport equation. *Annual Review of Heat Transfer*, 17:205–265, 2014.

[24] Sandip Mazumder and Arunava Majumdar. Monte carlo study of phonon transport in solid thin films including dispersion and polarization. *Journal of Heat Transfer*, 123(4):749–759, 2001.

[25] Syed Ashraf Ali, Gautham Kollu, Sandip Mazumder, P Sadayappan, and Arpit Mittal. Large-scale parallel computation of the phonon boltzmann transport equation. *International Journal of Thermal Sciences*, 86:341–351, 2014.

[26] Daniel P Sellan, JE Turney, Alan JH McGaughey, and Cristina H Amon. Cross-plane phonon transport in thin films. *Journal of Applied Physics*, 108(11):113524, 2010.

[27] X. Huang et al. Sub 50-nm finfet: Pmos. pages 67–70, 445 Hoes Lane, Piscataway, NJ 08855, 12 1999. Institute of Electrical and Electronics Engineers, Institute of Electrical and Electronics Engineers.

[28] Joseph E Turney, Alan JH McGaughey, and Cristina H Amon. In-plane phonon transport in thin films. *Journal of Applied Physics*, 107(2):024317, 2010.

[29] A. R. Brown et al. Comparitive simulation analysis of process-induced variability in nanoscale soi and bulk trigate finfets. *IEEE Transactions on Electron Devices*, 60(11):3611–3617, 11 2013.

[30] G.P. Srivastava. *The Physics of Phonons*. Taylor and Francis Group, 270 Madison Avenue New York, NY 10016, 1990.

[31] P Pavone, K Karch, O Schütt, D Strauch, W Windl, P Giannozzi, and S Baroni. Ab initio lattice dynamics of diamond. *Physical Review B*, 48(5):3156, 1993.

[32] Alistair Ward, DA Broido, Derek A Stewart, and Gernot Deinzer. Ab initio theory of the lattice thermal conductivity in diamond. *Physical Review B*, 80(12):125203, 2009.

[33] Nicolas Mounet and Nicola Marzari. First-principles determination of the structural, vibrational and thermodynamic properties of diamond, graphite, and derivatives. *Physical Review B*, 71(20):205214, 2005.

[34] A Ward and DA Broido. Intrinsic phonon relaxation times from first-principles studies of the thermal conductivities of si and ge. *Physical Review B*, 81(8):085205, 2010.

[35] Stefano Baroni, Stefano De Gironcoli, Andrea Dal Corso, and Paolo Giannozzi. Phonons and related crystal properties from density-functional perturbation theory. *Reviews of Modern Physics*, 73(2):515, 2001.

[36] E. Molinari A. Debernardi, S. Baroni. Anharmonic phonon lifetimes in semiconductors from density-functional perturbation theory. *Physical Review Letters*, 75(9):1819–1822, 8 1995.

[37] A. Ward and D. A. Broido. Intrinsic phonon relaxation times from first-principles studies of the thermal conductivities of si and ge. *Physical Review B*, 81(8):1–5, 2 2010.

[38] Paolo Giannozzi, Stefano Baroni, Nicola Bonini, Matteo Calandra, Roberto Car, Carlo Cavazzoni, Davide Ceresoli, Guido L Chiarotti, Matteo Cococcioni, Ismaila Dabo, Andrea Dal Corso, Stefano de Gironcoli, Stefano Fabris, Guido Fratesi, Ralph Gebauer, Uwe Gerstmann, Christos Gougoussis, Anton Kokalj, Michele Lazzeri, Layla Martin-Samos, Nicola Marzari, Francesco Mauri, Riccardo Mazzarello, Stefano Paolini, Alfredo Pasquarello, Lorenzo Paulatto, Carlo Sbraccia, Sandro Scandolo, Gabriele Sclauzero, Ari P Seitsonen, Alexander Smogunov, Paolo Umari, and Renata M Wentzcovitch. Quantum espresso: a modular and open-source software project for quantum simulations of materials. *Journal of Physics: Condensed Matter*, 21(39):395502, 2009.

[39] J-S Wang, Jian Wang, and JT Lü. Quantum thermal transport in nanostructures. *The European Physical Journal B*, 62(4):381–404, 2008.

[40] Gang Chen. Nanoscale energy transport and conversion. 2005.

[41] JE Turney, ES Landry, AJH McGaughey, and CH Amon. Predicting phonon properties and thermal conductivity from anharmonic lattice dynamics calculations and molecular dynamics simulations. *Physical Review B*, 79(6):064301, 2009.

[42] AJH McGaughey and M Kaviany. Thermal conductivity decomposition and analysis using molecular dynamics simulations. part i. lennard-jones argon. *International Journal of Heat and Mass Transfer*, 47(8):1783–1798, 2004.

[43] Shuze Zhu and Teng Li. Hydrogenation-assisted graphene origami and its application in programmable molecular mass uptake, storage, and release. *ACS nano*, 8(3):2864–2872, 2014.

[44] Frank H Stillinger and Thomas A Weber. Computer simulation of local order in condensed phases of silicon. *Physical review B*, 31(8):5262, 1985.

[45] JG Swadener, MI Baskes, and M Nastasi. Molecular dynamics simulation of brittle fracture in silicon. *Physical review letters*, 89(8):085503, 2002.

[46] Jing Xu, Signe Kjelstrup, and Dick Bedeaux. Molecular dynamics simulations of a chemical reaction; conditions for local equilibrium in a temperature gradient. *Physical Chemistry Chemical Physics*, 8(17):2017–2027, 2006.

[47] Peter L Freddolino, Anton S Arkhipov, Steven B Larson, Alexander McPherson, and Klaus Schulten. Molecular dynamics simulations of the complete satellite tobacco mosaic virus. *Structure*, 14(3):437–449, 2006.

[48] Yongjin Lee and Gyeong S Hwang. Force-matching-based parameterization of the stillinger-weber potential for thermal conduction in silicon. *Physical Review B*, 85(12):125204, 2012.

[49] Alan JH McGaughey and Jason M Larkin. Predicting phonon properties from equilibrium molecular dynamics simulations. *Ann. Rev. Heat Transfer*, 17:49–87, 2014.

[50] A. J. H McGaughey and M. Kaviany. Phonon transport in molecular dynamics simulations: Formulation and thermal conductivity prediction.

[51] Alan JH McGaughey and M Kaviany. Quantitative validation of the boltzmann transport equation phonon thermal conductivity model under the single-mode relaxation time approximation. *Physical Review B*, 69(9):094303, 2004.

[52] PK Schelling, SR Phillpot, and P Keblinski. Phonon wave-packet dynamics at semiconductor interfaces by molecular-dynamics simulation. *Applied Physics Letters*, 80(14):2484–2486, 2002.

[53] JE Turney, AJH McGaughey, and CH Amon. Assessing the applicability of quantum corrections to classical thermal conductivity predictions. *Physical Review B*, 79(22):224305, 2009.

[54] Mehran Kardar. *Statistical Physics of Particles*, volume 1 of *1*, chapter 3, pages 57–84. Cambridge University Press, University Printing House, Cambridge CB2 8BS, United Kingdom, 6 edition, 2007. "".

[55] Robert E. Peierls. *Quantum Theory of Solids*. Oxford University Press, Amen House, London E.C.4, 1 edition, 1955.

[56] Carlo Jacoboni and Lino Reggiani. The monte carlo method for the solution of charge transport in semiconductors with applications to covalent materials. *Reviews of Modern Physics*, 55(3):645, 1983.

[57] JA Fleck and JD Cummings. An implicit monte carlo scheme for calculating time and frequency dependent nonlinear radiation transport. *Journal of Computational Physics*, 8(3):313–342, 1971.

[58] Ivan Lux and László Koblinger. *Monte Carlo particle transport methods: neutron and photon calculations*, volume 102. Citeseer, 1991.

[59] Jean-Philippe M Péraud and Nicolas G Hadjiconstantinou. Efficient simulation of multidimensional phonon transport using energy-based variance-reduced monte carlo formulations. *Physical Review B*, 84(20):205331, 2011.

[60] ASME Majumdar. Microscale heat conduction in dielectric thin films. *Journal of Heat Transfer*, 115(1):7–16, 1993.

[61] AA Joshi and A Majumdar. Transient ballistic and diffusive phonon heat transport in thin films. *Journal of Applied Physics*, 74(1):31–39, 1993.

[62] Rodrigo Escobar. *Lattice Boltzmann Modeling of Phonon Transport in Silicon Films*. PhD thesis, Carnegie Mellon University, Pittsburgh Pennsylvania, 7 2005. "".

[63] Aydin Nabovati, Daniel P Sellan, and Cristina H Amon. On the lattice boltzmann method for phonon transport. *Journal of Computational Physics*, 230(15):5864–5876, 2011.

[64] Syed Ashraf Ali and Sandip Mazumder. Phonon heat conduction in multidimensional heterostructures: predictions using the boltzmann transport equation. *Journal of Heat Transfer*, 137(10):102401, 2015.

[65] C. Kittle. *Introduction to Solid State Physics*. John Wiley & Sons, Inc., New York, 1996.

[66] David J. Griffiths. *Introduction to Quantum Mechanics*. Pearson Prentice Hall, Upper Saddle River, NJ 07458, 2005.

[67] V. L. Gurevich. *Transport in Phonon Systems*. North-Holland Physics Publishing, 1000 AC Amsterdam, Netherlands, 1986.

[68] N. W. Ashcroft and N. D Mermin. *Solid State Physics*. Saunders College Publishers, 1976.

[69] Xinjiang Wang and Baoling Huang. Computational study of in-plane phonon transport in si thin films. *Scientific reports*, 4, 2014.

[70] Max Born and Kun Huang. *Dynamical theory of crystal lattices*. Clarendon Press, 1954.

[71] Julian D Gale and Andrew L Rohl. The general utility lattice program (gulp). *Molecular Simulation*, 29(5):291–341, 2003.

[72] Louis P Bouckaert, Roman Smoluchowski, and Eo Wigner. Theory of brillouin zones and symmetry properties of wave functions in crystals. *Physical Review*, 50(1):58, 1936.

[73] DA Broido, A Ward, and N Mingo. Lattice thermal conductivity of silicon from empirical interatomic potentials. *Physical Review B*, 72(1):014308, 2005.

[74] M Omini and A Sparavigna. Beyond the isotropic-model approximation in the theory of thermal conductivity. *Physical Review B*, 53(14):9064, 1996.

[75] A Sparavigna. Role of nonpairwise interactions on phonon thermal transport. *Physical Review B*, 67(14):144305, 2003.

[76] L Lindsay, DA Broido, and Natalio Mingo. Lattice thermal conductivity of single-walled carbon nanotubes: Beyond the relaxation time approximation and phonon-phonon scattering selection rules. *Physical Review B*, 80(12):125407, 2009.

[77] Aleksandr Chernatynskiy and Simon R Phillpot. Evaluation of computational techniques for solving the boltzmann transport equation for lattice thermal conductivity calculations. *Physical Review B*, 82(13):134301, 2010.

[78] Joseph Callaway. Model for lattice thermal conductivity at low temperatures. *Physical Review*, 113(4):1046, 1959.

[79] PG Klemens. The thermal conductivity of dielectric solids at low temperatures (theoretical). In *Proceedings of the Royal Society of London A: Mathematical, Physical and Engineering Sciences*, volume 208, pages 108–133. The Royal Society, 1951.

[80] MG Holland. Analysis of lattice thermal conductivity. *Physical Review*, 132(6):2461, 1963.

[81] Suhas Patankar. *Numerical heat transfer and fluid flow*. CRC press, 1980.

[82] Lisa J Porter, Sidney Yip, Masatake Yamaguchi, Hideo Kaburaki, and Meijie Tang. Empirical bond-order potential description of thermodynamic properties of crystalline silicon. *Journal of applied physics*, 81(1):96–106, 1997.

[83] John M Ziman. *Electrons and phonons: the theory of transport phenomena in solids*. Oxford University Press, 1960.

[84] Austin J Minnich. Thermal phonon boundary scattering in anisotropic thin films. *Applied Physics Letters*, 107(18):183106, 2015.

[85] Jie Zou and Alexander Balandin. Phonon heat conduction in a semiconductor nanowire. *Journal of Applied Physics*, 89(5):2932–2938, 2001.

[86] Arpit Mittal and Sandip Mazumder. Hybrid discrete ordinatesspherical harmonics solution to the boltzmann transport equation for phonons for non-equilibrium heat conduction. *Journal of Computational Physics*, 230(18):6977–7001, 2011.

[87] Youcef Saad SPARSKIT. a basic tool kit for sparse matrix computations-version 2. Technical report, Tech. Rep. Computer Science Department, Univ. of Minnesota, Minneapolis, MN, 1994.

[88] Miguel Hermanns. Parallel programming in fortran 95 using openmp.

[89] Max A Heaslet and Robert F Warming. Radiative transport and wall temperature slip in an absorbing planar medium. *International Journal of Heat and Mass Transfer*, 8(7):979–994, 1965.

[90] Michael F Modest. *Radiative heat transfer*. Academic press, 2013.

[91] M Necati Özışık. *Radiative transfer and interactions with conduction and convection*. Werbel & Peck, 1973.

[92] Yang-Kyu Choi, Leland Chang, Pushkar Ranade, Jeong-Soo Lee, Daewon Ha, Sriram Balasubramanian, Aditya Agarwal, Mike Ameen, Tsu-Jae King, and Jeffrey Bokor. Finfet process refinements for improved mobility and gate work function engineering. In *Electron Devices Meeting, 2002. IEDM'02. International*, pages 259–262. IEEE, 2002.